Investigation of hydrogen diffusion and accumulation in X70 pipeline steel

A Thesis Submitted to the

College of Graduate and Postdoctoral Studies in Partial Fulfillment of the

Requirements for the Degree of Master of Science

In the Department of Mechanical Engineering

University of Saskatchewan

Saskatoon

By

Alen Thomas

PERMISSION TO USE

In presenting this thesis in partial fulfillment of the requirements for a postgraduate degree from the University of Saskatchewan, I agree that the Libraries of this University may make it freely available for inspection. I further agree that permission for copying of this thesis in any manner, in whole or in part, for scholarly purposes may be granted by the professor who supervised my thesis work or, in their absence, by the Head of the Department or the Dean of the College in which my thesis work was done. It is understood that any copying or publication or use of this thesis or parts thereof for financial gain shall not be allowed without my written permission. It is also understood that due recognition shall be given to me and to the University of Saskatchewan in any scholarly use, which may be made of any material in my thesis.

Requests for permission to copy or to make other use of the material in this thesis in whole or part should be addressed to:

Head of the Department of Mechanical Engineering
University of Saskatchewan
57 Campus Drive
Saskatoon, Saskatchewan, S7N 5A9
Canada

OR

Dean
College of Graduate and Postdoctoral Studies
University of Saskatchewan
116 Thorvaldson Building, 110 Science Place
Saskatoon, Saskatchewan S7N 5C9
Canada

ABSTRACT

Pipelines quickly, safely and economically transport large volumes of oil and gas compared to trains, trucks and ships. However, they occasionally fail leading to environmental pollution, fatalities and financial losses. Pipeline cracking by hydrogen embrittlement is the main cause of pipeline failure. The main focus of this research was on the effect of grain size and misorientation on hydrogen diffusion and accumulation in X70 pipeline steel.

In this investigation, the hydrogen permeation experiment was used to determine the parameters for hydrogen diffusion, and the hydrogen microprint technique was used to visualize the diffusion path in X70 steel. Hydrogen atoms were oxidized in the hydrogen permeation experiment, whereas they were reacted with an emulsion coating in the hydrogen microprint experiment. The samples for studying the effect of grain size on hydrogen diffusion and accumulation were taken from the mid-layer at the segregation zone and the top-layer of the first batch of X70-1 steel. The top-layer of another batch of steel, X70-2, was used to study the effect of misorientation on hydrogen diffusion and accumulation.

Hydrogen permeation experiment, in X70-1 steel, allowed in concluding that the permeability increased for larger grain sizes in both layers of steel. Also, the density of total, reversible, and irreversible hydrogen trapping sites of top-layer decreased for larger grains. However, the irreversible and total trapping sites of mid-layer showed an initial growth and subsequent decay with an increase in grain size. The hydrogen permeation experiment, in X70-2 steel, allowed in concluding that the permeability and effective diffusion coefficient decreased with an increase in grain misorientation. Also, the density of total and irreversible trapping sites increased with an increase in grain misorientation. The conclusions from hydrogen permeation experiments were validated with hydrogen microprint technique results. Grain boundaries, triple junctions and deformed grains in the steel microstructure are considered as reversible trapping sites due to their superior hydrogen diffusion in hydrogen microprint experiments. Also, preferential hydrogen diffusion through steel microstructure increased in the order of non-deformed grains, grain boundaries, inclusion interfaces, triple junctions, cementites and matrix-inclusion interfaces with matrix-inclusion interfaces being the easy path for diffusion. The analysis of hydrogen microprint technique results also allowed in concluding that the presence and absence of a circular pattern of superimposed white silver particles around inclusions and precipitates is a method to distinguish the type of hydrogen traps in materials.

ACKNOWLEDGMENT

I want to express my sincere gratitude to my supervisor, Prof. Jerzy A. Szpunar, for giving me the valuable opportunity of joining his research group as a thesis-based master student since fall, 2016 at the University of Saskatchewan. He was giving me enough motivation to prepare myself as a material science student. Also, he was guiding me with valuable inputs throughout my research. I am also thankful for his financial support in the form of a student stipend for almost three years. Also, he allowed my development outside the academics by granting the permission for working as a Student Innovation and Business Analyst (December 2016 – November 2019) and Summer Entrepreneur (May 2019 – August 2019) at Innovation Enterprise, University of Saskatchewan.

My appreciation also goes to my advisory committee members, Prof. Akindele G. Odeshi and Prof. Ikechukwuka N. Oguocha, for their valuable guidance. The email communications with the ex-students of our research group, Dr. Mohammad Ali Mohtadi Bonab and Dr. Salman Razavi found to be helpful. The reasonably big research group under Dr. Szpunar was always there to broaden my knowledge related to the topic, and I am grateful for their time. My gratitude also goes to the mechanical engineering departmental assistant, Nanfang Zhao, and the staff at Engineering Shops for their training and permission to use the resources for sample preparations.

Also, sincere thanks to my best friend, Easwaran Nampoothiri, an ongoing Ph.D. student, who always motivate me from the dullness of living in the freezing weather of Saskatchewan, Canada.

DEDICATION

Success needs to be shared with the people who stay with me in my failures. Hence, I dedicate this thesis to my beloved family and friends who stay with my bumpy journey in this effort. I am always lucky to have the blessings from my late grandparents and my dearest uncle, late Chacko Mathew. I intensely believe that those valuable blessings make me capable of doing this work, and I would like to dedicate this work to them as well.

TABLE OF CONTENTS

LIST OF TABLES

LIST OF FIGURES

LIST OF ABBREVIATIONS

API	American Petroleum Institute
AF	Acicular ferrite
B	Bainite
DP	Degenerate pearlite
EBSD	Electron backscatter diffraction
EDS	Energy-dispersive X-ray spectroscopy
HE	Hydrogen embrittlement
HIC	Hydrogen induced cracking
HMT	Hydrogen microprint technique
HP	Hydrogen permeation
IEA	International Energy Agency
ISO	International Organization for Standardization
KAM	Kernel average misorientation
OM	Optical microscopy
PF	Polygonal ferrite
SEM	Scanning electron microscope
SSC	Sulfide stress cracking
QF	Quasi polygonal ferrite
RD	Rolling direction
TD	Transverse direction
USD	United States dollar

LIST OF SYMBOLS

Capp	Apparent hydrogen solubility, mol. cm^{-3}
D_{eff}	Effective hydrogen diffusion coefficient, $cm^2.s^{-1}$
I_∞	Steady-state current, µA
$J_\infty L$	Hydrogen permeability, mol. $cm^{-1}.s^{-1}$
Nt	Total number of hydrogen trapping sites, cm^{-3}
Nr	Number of reversible hydrogen trapping sites, cm^{-3}
Nir	Number of irreversible hydrogen trapping sites, cm^{-3}
TL	Time lag, s
λ	Degree of freedom
σ	Standard deviation, mA
%	Percentage

CHAPTER 1

INTRODUCTION

1.1. Overview

This chapter contains an introduction, motivation, research objectives, research contributions, and thesis arrangement.

1.2. Introduction

Revenue from the export of oil and natural gas through pipelines contributes to the economic development of Canada [1]. Natural Resources Canada reported that Canada needs 15,000 truck trips per day to transport three million barrels of crude oil in the absence of pipelines. It will lead to high road traffic that can cause problems with public safety, road maintenance, and environmental pollutions [2]. The Global Fossil Infrastructure Tracker reveals that the number of oil and natural gas pipeline projects has tripled since 1996, with natural gas contributing to 80 percent of the pipeline development [3]. However, political policies and pipeline failures create uncertainty on pipeline development. In this section, the existing global pipeline network and the planned pipeline expansions are discussed. An analysis of pipeline failures in North America is also presented.

1.2.1. Growth of pipeline network

The preference of pipelines over trains, trucks, and ships is due to its quick, safe, and economical mode of transporting large volumes of oil and gas [2]. Figure 1.1 shows the growth of the pipeline network for the last 36 years [3]. Nace et al. reported that the global number of new pipelines per year increased in the past with slight ups and downs due to the political pressures of switching to renewable energies from carbon-intensive energy.

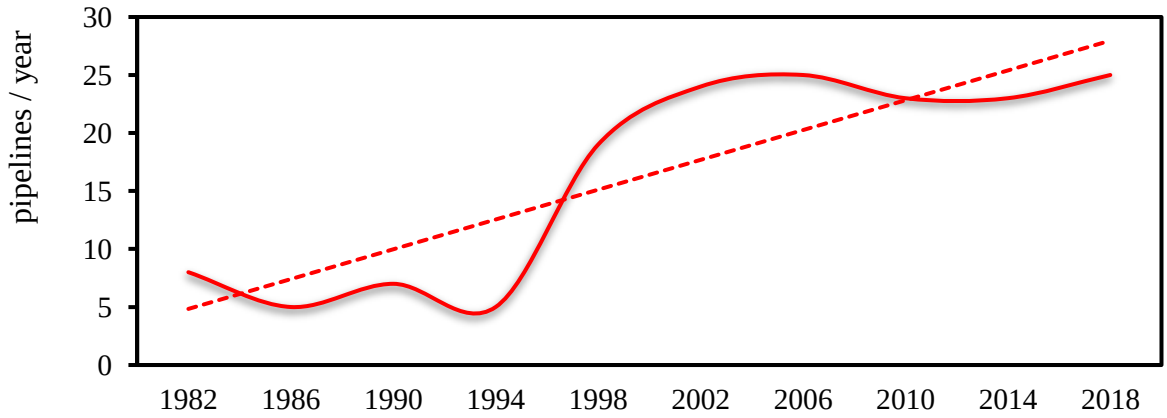

Figure 1.1. The global number of new pipelines per year for the last 36 years [3].

Global government policies were not favorable to the use of non-renewable energy. However, the growth of pipeline network is anticipated all over the world. The latest report from 2019 shows that global pipeline networks will increase by 29 percent with the completion of 302 new pipeline projects under construction [3]. Figure 1.2 shows the regional shares in the global pipeline development.

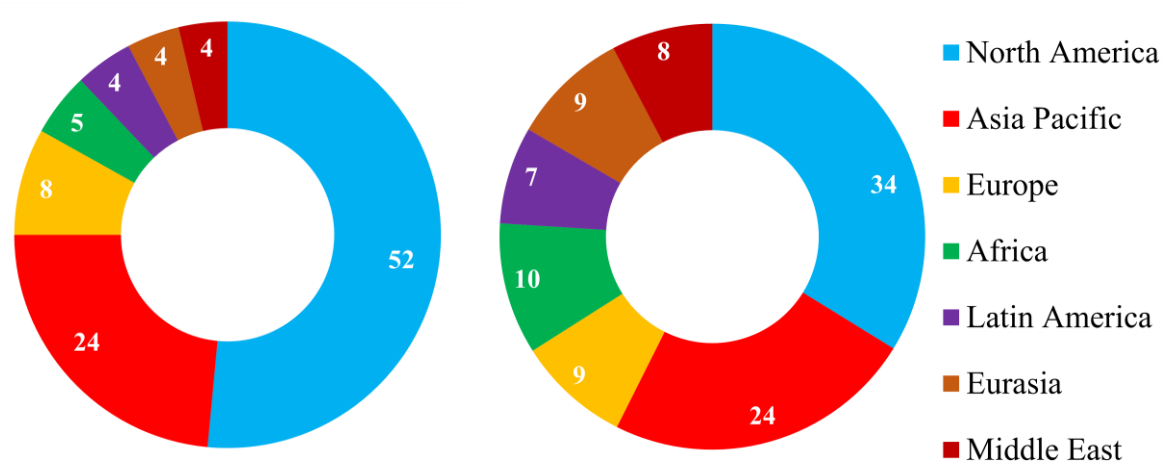

(a) (b)

Figure 1.2. Regional shares (in %) in global pipeline development (a) number of pipeline projects and (b) kilometers of pipeline projects [3].

Interestingly, the majority of pipeline development projects occur in North America and Asia Pacific regions [3]. North America, including the United States, Canada and Mexico, leads the contribution by numbers and kilometers of the pipeline projects. Recently, the advantages of pipelines allow the North American governments to proceed with the decade-old Trans Canada Energy's Keystone XL pipeline project [4]. Hence, the United States that imports 7 million barrels of oil each day from countries such as Iraq, Saudi Arabia, Mexico, and Venezuela becomes dependable to a stable source of crude oil from Canada [5]. The other recently approved projects like Enbridge's Line 3 Replacement and Trans Mountain's Expansion also show the continuing growth of pipeline networks in North America [4]. In general, literature reported that pipeline network will continue to grow like the past, and North America is the biggest market.

1.2.2. Challenges associated with pipeline transport of oil and gas

Even though the global pipeline network increases, there exists corrosion, cracking, excavation damages, natural force damages, operation failures, and manufacturing failures associated with

them [6]. The pipeline failures lead to economic loss and a risk to human and animal life [7, 8]. Figure 1.3 shows the classification of failure for the North American pipelines for the period between 1985 and 2018 [6, 7, 8, 9, 10, 11]. The internal corrosion that mostly occurs by cracking also contributes to the total corrosion failures. The failures from corrosion and cracking vary from 25 to 67 percent of the reported crashes.

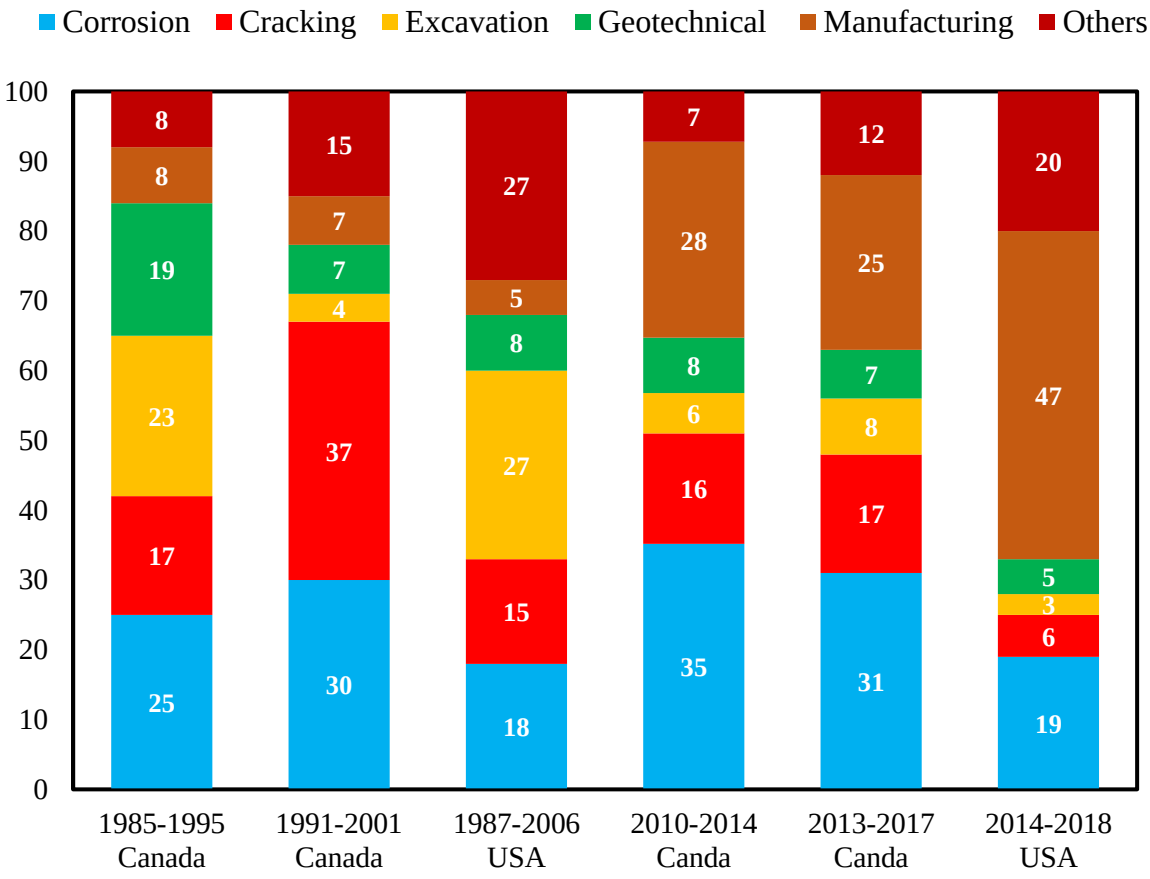

Figure 1.3. Classification of failure for North American pipeline (in %) [6, 7, 8, 9, 10, 11].

The cracking in pipelines occurs by hydrogen embrittlement (HE). Sulfide stress cracking (SSC) and hydrogen-induced cracking (HIC) were the two forms of HE [12]. The former occurs by the presence of residual stress and fatigue loads, whereas the latter occurs even without any external or internal stresses. However, the two forms of HE occurs in the presence of hydrogen. The hydrogen is produced by surface corrosion at pipeline steel in the presence of hydrogen sulfide from the transport of oil and gas. The fabrication and processing methods of the pipeline steel were other sources of hydrogen that can lead to the HE. The generated hydrogen atom diffuses into pipeline steel, and its rate increases with the presence of sulfide ions from oil and gas. However, some amount of the absorbed hydrogen atoms were accumulated at traps like voids, vacancies, dislocations, inclusions, precipitates, triple junctions, grain boundaries, microstructural phases, and segregation zones to initiate HE in pipeline steels [13, 14, 15].

1.2.3. Need for research

The use of hydrogen as the energy source and its transport through the pipeline network already started in North America. The United States owns 1600 miles of hydrogen pipelines, and the majority of them were at the Gulf Coast region [16]. However, the harmful effect of hydrogen on the pipeline network needs investigations before hydrogen transportation through pipelines is established. The diffusion parameters such as permeability, effective diffusion coefficient, and apparent solubility of hydrogen in the material were affected by the different hydrogen traps in pipeline steel. However, the hydrogen traps like grain boundaries, triple junctions, and dislocations significantly impact those diffusion parameters. Also, the accumulated hydrogen that leads to the HE in the pipeline steel varies with the changes in the trapping sites. Hence, this research work is needed to study the effect of grain size and structure misorientation on hydrogen diffusion and accumulation in pipeline steels. The amount of grain boundaries and triple junctions depends on the changes in grain size, whereas the misorientations can represent the induced dislocations in steels.

1.3. The motivations for present investigations

The increasing population, rising gross domestic product, and the improved standard of living need more energy from all sources, including oil and gas [17]. Hence, the pipelines that mainly transport oil and natural gas plays a significant role in the world's energy supply. Also, the new developments in the pipeline network create job opportunities. Hence, the expanding pipeline networks provide income from employment and energy for daily life at the same time. Remarkably, 30 percent of the global pipeline development [3] and 20 percent of the worldwide oil and natural gas demand [18] occurs in North America. Therefore, contributions of the pipeline network to global development, especially to North America, motivates to work for the improvement of the pipeline steels. The high demand for oil and gas and the massive employment opportunities were detailed in this section.

1.3.1. The high demand for oil and gas

The world population and the total energy demand are expected to exceed nine billion and increase by 27 % in 2040 [4, 19, 17]. The total energy consists of different forms of energy like oil, natural gas, coal, bioenergy, nuclear, hydroelectricity and other renewable energies [20]. The world energy model designed by the International Energy Agency (IEA) consists of two main scenarios as new policies and sustainable development scenarios. The former provides a projection of the energy sector by considering launched and announced policies of

various governments, whereas the latter considers the internationally agreed objectives on climate, air quality, and universal access to modern energy [21]. According to IEA, oil and natural gas contribute to 48 percent shares of the global energy demand by 2040 with the very likely sustainable development scenario [20, 22]. However, Figure 1.4 shows that oil and natural gas contribute to 53 percent of the global energy demand by 2040 with the new policies scenario. The same figure also shows that oil and natural gas contribute to 54 percent of the energy consumption in 2017. Hence, the significantly high contribution of oil and natural gas for energy consumption and energy demand also shows that pipeline networks that mainly transport those energies continue to grow all over the world [20].

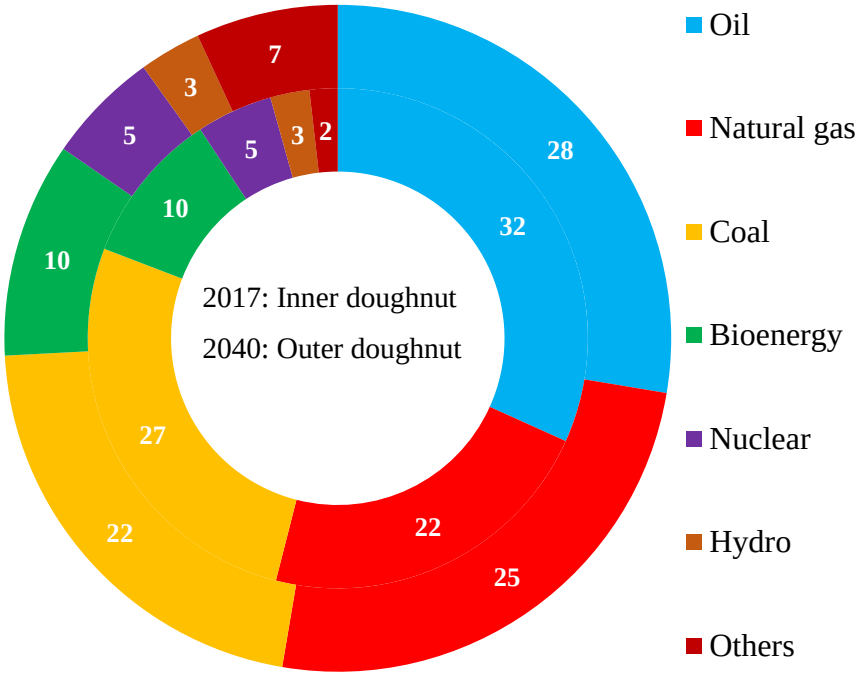

Figure 1.4. Types of energy (in %) in global energy consumption and demand [20].

Figure 1.5 shows the regional shares of global oil and natural gas consumption and demand [18, 23]. The governmental policies favoring increased use of renewable energies will reduce the demand for oil and gas in North America and Europe. However, North America still holds a second-largest regional share of more than 20 % for the global oil and natural gas consumption and demand. The different studies indicate that the pipeline network, which mainly transfers oil and natural gas, plays a significant role in serving the whole world with the required energy demand. The highest number of pipeline development projects in North America [3] occurs from their significant need for oil and gas [18].

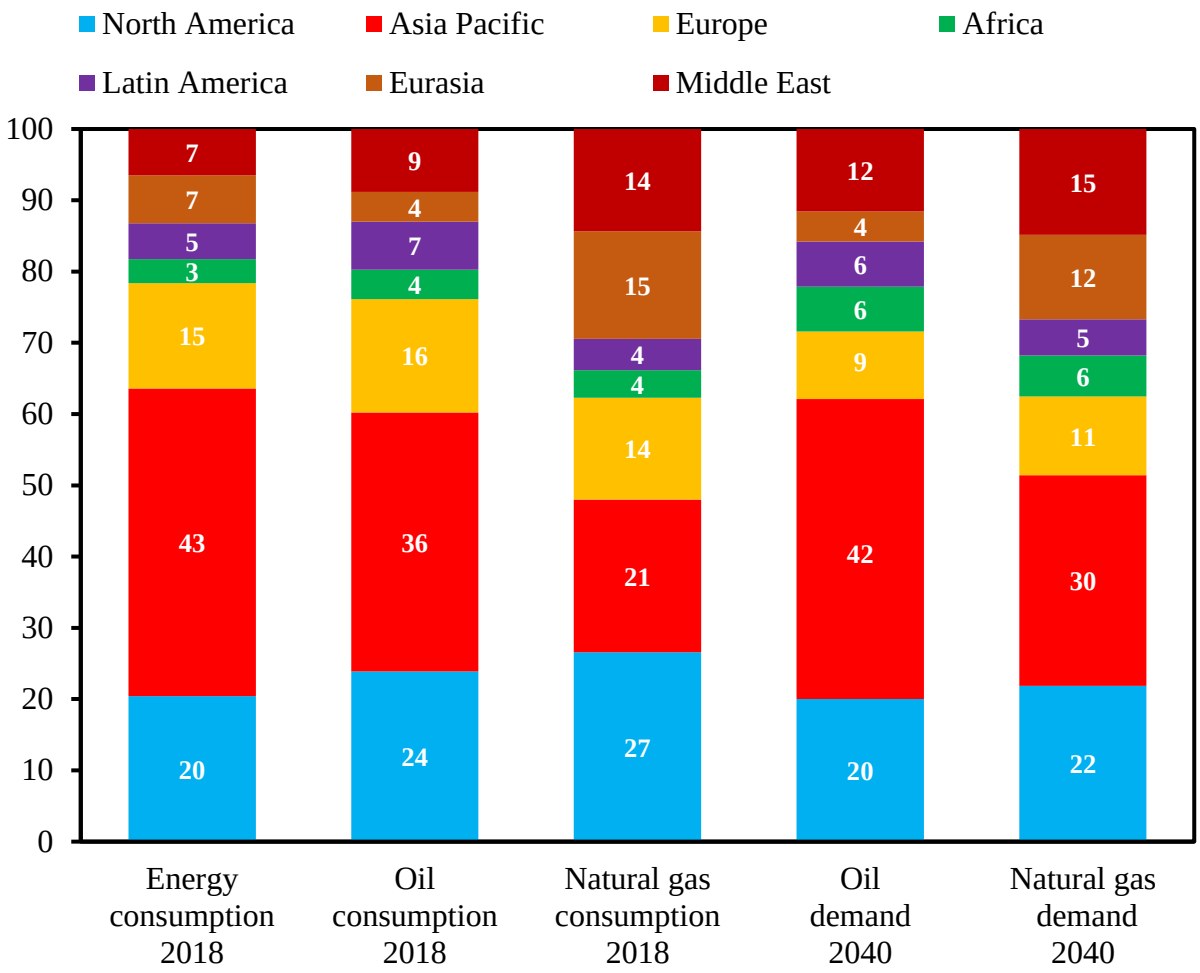

Figure 1.5. Regional shares (in %) of energy consumption and demand [18, 23].

1.3.2. Billion-dollar investments turn into million jobs

The pipelines with an expected lifespan of 40 years or more attract the banks and equity investors for a massive investment considering the immense contribution of oil and natural gas for the projected energy demand by 2040 [20]. Figure 1.6 shows the regional shares of estimated investments in the pipeline industry for the pipeline projects in the pre-construction and construction stage [3]. Remarkably, 37 % of the global investment of over 600 billion USD occurs in North America as it holds the second-largest share in the worldwide demand for oil and natural gas. Also, 18 % of global oil and natural gas exports happen from North America [23]. The massive investment leads to economic activity, which eventually leads to job opportunities and economic growth across the nation [4]. The global pipeline industry will support 2 million jobs per year based on the projected job opportunities and estimated investment in North America. However, the pipeline industry of North America will support 725,000 direct and indirect jobs per year without considering the other segments of the industry, whereas Canada will support 10 % of those jobs [24].

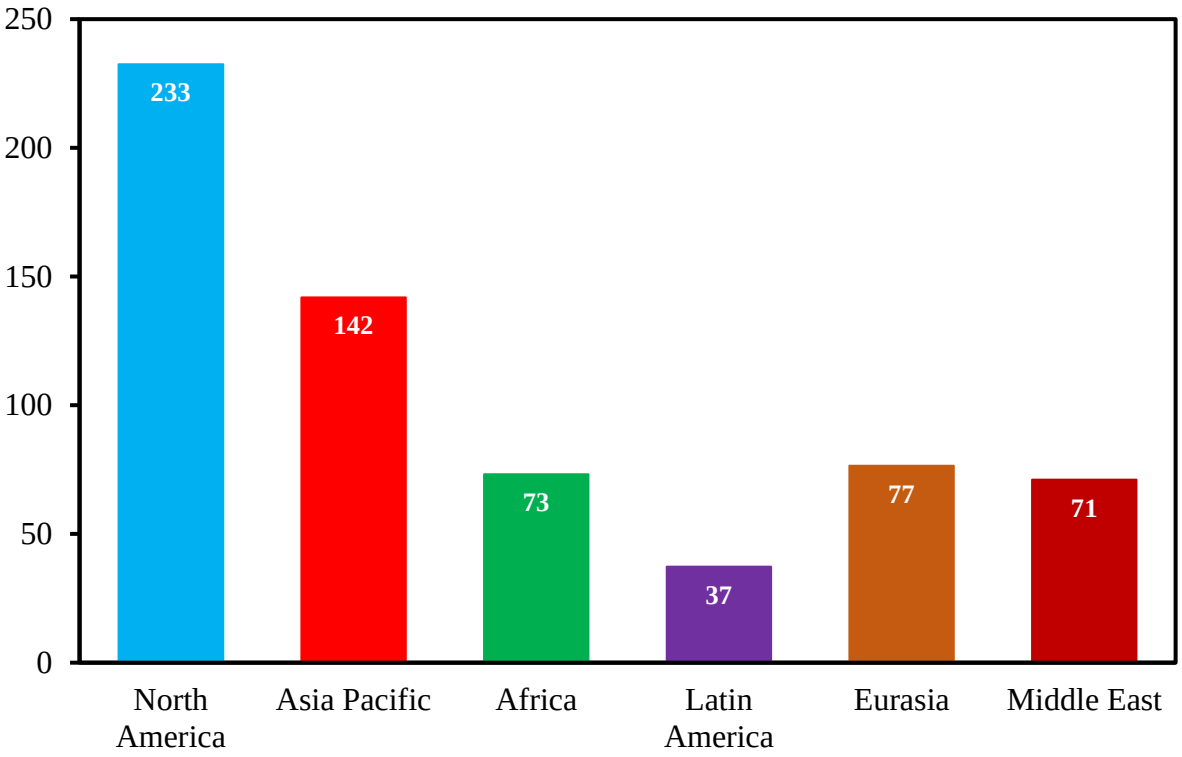

Figure 1.6. Estimated global investments in pipelines under development (Billion USD) [3].

1.4. Research objectives

The overall goal of this research was to understand the effect of grain size and grain misorientation on hydrogen diffusion and accumulation in X70 pipeline steels. The calculated diffusion parameters using the hydrogen permeation (HP) experiment enable determination of the hydrogen trapping sites in pipeline steel. Also, the hydrogen microprint technique (HMT) experiment was used to visualize hydrogen diffusion path through grains, grain boundaries, triple junctions, microstructural phases and around inclusions. The specific objectives of this research were:

1. To perform thermomechanical treatments in X70 pipeline steels to obtain samples with different grain size and misorientation.
2. To quantify hydrogen trapping sites using hydrogen permeation experiment to investigate the role of grain size and misorientation on hydrogen diffusion.
3. To visualize hydrogen diffusion path using hydrogen microprint technique experiment to investigate the role of grain size and misorientation on hydrogen diffusion.

1.5. Research contributions

In this research, the hydrogen permeation experiment and the hydrogen microprint technique experiment was used to study the effect of grain size and misorientation on hydrogen diffusion

and accumulation in X70 steel. The contributions from the research were prepared as four manuscripts, as listed below, and are currently under review in peer-reviewed journals.

1. Hydrogen diffusion and trapping in X70 pipeline steel.
   In this manuscript, the effect of a wide range of grain sizes on diffusion parameters and trapping sites in different layers of the pipeline steel was studied. Also, the diffusion through reversible trapping sites such as grain boundaries and triple junctions were visualized.
2. Hydrogen diffusion and trapping in X70 steel before and after cold rolling operation.
   In this manuscript, the effect of grain misorientations on diffusion parameters and trapping sites in pipeline steel was studied. Also, the preferential diffusion through the deformed grains, grain boundaries, and matrix-inclusion interfaces was visualized.
3. Effect of inclusions on hydrogen diffusion and trapping in X70 pipeline steel.
   In this manuscript, the effect of inclusions on diffusion parameters and trapping sites in pipeline steel was studied by taking steel samples from mid-layer at the segregation zone and top-layer. Also, preferential hydrogen diffusion around the inclusions was visualized to validate the estimated diffusion parameters.
4. Visualizing the effect of inclusions and precipitates for hydrogen diffusion in X70 steel by hydrogen microprint technique.
   In this manuscript, a modified hydrogen microprint technique procedure was used for visualizing the hydrogen diffusion path. The unique observations from the modified method allow in proposing a new method for classifying the inclusions and precipitates as reversible or irreversible traps.

1.6. Thesis arrangement

The thesis report contains five chapters, and each of them begins with an overview of that chapter. The current chapter, chapter one, includes an introduction, motivation, research objectives, research contributions, and thesis arrangement. The second chapter contains a summarized literature review of the topic. The third and fourth chapter is broad and significant as it explains the materials and methodologies in the former, and results and discussions in the latter. The thesis report finishes with chapter five, and it contains the conclusions from this study and the recommended future works.

CHAPTER 2

LITERATURE REVIEW

2.1. Overview

Chapter two begins with the description of hydrogen embrittlement and its different forms in pipeline steels. Further, the embrittlement susceptibility in different grades of pipeline steels and different types of hydrogen traps are reviewed. The chapter also contains the research gaps on the effect of grain size and grain misorientation on hydrogen diffusion and accumulation. Finally, the experimental factors affecting the hydrogen permeation experiment are also summarized in this chapter.

2.2. Hydrogen embrittlement in pipeline steels

The decline in material ductility that leads to a crack propagation without considerable plastic deformation is known as embrittlement [25]. However, the embrittlement that occurs in the presence of atomic hydrogen is known as hydrogen embrittlement (HE). All forms of HE falls into two types depending on the source of the hydrogen [26]. The embrittlement that occurs by the preexisting hydrogen inside the material is internal hydrogen embrittlement, whereas the hydrogen from the environment causes the second type of embrittlement known as hydrogen environmental embrittlement. The two types of HE can occur in two primary forms [12]. The embrittlement that occurs by the presence of residual stress and fatigue loads in the presence of hydrogen is known as sulfide stress cracking (SSC) and often known as hydrogen-assisted cracking (HAC), whereas the embrittlement that occurs even without any external or internal stresses in the presence of hydrogen is known as hydrogen-induced cracking (HIC) [27]. The other forms of HE include step wise cracking (SWC) and stress oriented hydrogen induced cracking (SOHIC). In SWC, the hydrogen cracks that lie parallel to each other causes shear stresses between the main cracks, and it leads to interconnected cracks between them. The hydrogen-induced cracking that is propagated by internal hoop stresses is known as SOHIC. SWC and SOHIC were often considered as HIC to limit the HE failures to SSC and HIC.

2.2.1. Sulfide stress cracking in pipeline steels

SSC was reported since the 1940s, and it initially occurs in North America with the failure of several oil and gas systems [28]. The SSC failures occur without any plastic deformation, and it results in extensive damages, injuries, and fatalities [28]. SSC occurs by cathodic embrittlement mechanism, and it usually happens in pipeline steels in the presence of wet

hydrogen sulfide or sulfide atmospheres from the transport of oil and natural gas. The steel reacts with the hydrogen sulfide to form metal sulfides and atomic hydrogen as corrosion products [29]. The sulfide ions act as a hydrogen recombination poison and prevent the formation of hydrogen molecules [30]. Therefore, the rate of hydrogen diffusion through the steel increases in the presence of sulfide ions. The favorable conditions of high strength material and high concentration of hydrogen sulfide from the environment accelerates the SSC in pipeline steels. Sun et al. explained that SSC occurs as a three-stage process [31]. In the first stage, the hydrogen atoms were absorbed and accumulated in the crystalline interstices and voids. SSC grows in the second stage with simultaneous assistance of highly concentrated stress and accumulated hydrogen atoms. The final stage involves the unnoticeable propagation of the cracks. During this type of embrittlement, the cracks initiate and propagate in a perpendicular direction to the applied stress and can result in a catastrophic failure of the pressurized systems [32].

2.2.2. Hydrogen-induced cracking in pipeline steels

HIC in pipelines was reported since 1976, and cracking occurs by a mechanism involving the formation, growth, and linkage of cracks [33]. The surface corrosion at pipeline steel in the presence of hydrogen sulfide from the transport of oil and gas generates free hydrogen. The hydrogen embrittling effect weakens the cohesive forces within the pipeline steel. Hence, HIC in pipelines can occur without any applied stresses. HIC begins with the accumulation of atomic hydrogen in the trapping sites of the steel. The trapped atomic hydrogen combines to form the hydrogen molecules, and it increases the internal pressures in trapping sites [34]. When the pressure of hydrogen gas becomes high, voids or cracks develop around the trapping sites. Generally, the mechanism of HIC in pipeline steel is explained as a two-stage process [35]. The first stage involves the diffusion of hydrogen and the formation of cracks. The second stage involves the propagation of cracks by the internal hydrogen pressure within the cracks. The linking of neighboring cracks enhances the crack propagation in pipelines.

2.3. Susceptibility of different pipeline steels for hydrogen embrittlement

The HE studies in the past uses different grades of pipeline steels, including X42 [36], X46 [37], X52 [38], X56 [39], X60 [40], X65 [41], X70 [42], X80 [43], X90 [44], X100 [45] and X120 [46]. The initial studies were focused on the lower grade of pipeline steel, and all the recent studies use the higher grade of pipeline steel. The American Petroleum Institute (API) recommends a minimum ultimate tensile strength of 415 MPa and 915 MPa for the X42 and

X120 grades of pipeline steels. The other grades of pipeline steel had an ultimate strength between 415 Mpa and 915 Mpa [47]. Bonab et al. reported that the X70 steel was more susceptible to HIC than X60 steel [48]. Also, they show that the HIC susceptibility increases with the hardness and strength of the steel. Shi et al. also reported that the HIC resistance decreases with an increase in the tensile strength of the pipeline steel [30]. As the HE susceptibility increases with the strength of steel, the stronger X120 easily cracks than the comparatively weaker X40. Hence, the available pipeline steel with high tensile strength is the best material for studying hydrogen diffusion and accumulation in pipeline steel. The steel microstructure changes from polygonal ferrite to acicular ferrite and bainite when the pipelines change from traditional X60 to the high strength grades of X80 and above [49]. Also, HE susceptibility increases in the order of polygonal ferrite, acicular ferrite, and bainite [50]. Hence, the microstructural changes with the pipeline steel grades were in agreement with the HE susceptibility of the different microstructures.

2.4. Susceptibility of different traps for hydrogen embrittlement

The HE begins with the hydrogen accumulation at various traps like inclusions, precipitates, voids, grain boundary, triple junctions, dislocations, microstructural phases, and segregation zones during the hydrogen diffusion through steels. Hydrogen accumulates in the steel as immobile and mobile hydrogen [51]. The traps which allow the accumulation of hydrogen were classified into two types [35]. The first kind of traps were reversible traps, and it does not trap the hydrogen permanently. The traps that more permanently stores the hydrogen were known as irreversible traps. Findley et al. reported that the binding energies of each trap with the hydrogen are the basis of trap classification [35]. The traps with binding energy lesser than 60 kilojoules per mole act as reversible traps, and all other traps belong to irreversible traps. The two types of traps possess differences in susceptibility to the HE. The previous studies reported that the finely distributed irreversible traps show less susceptibility to HE [52, 53, 54]. The reduction in HE susceptibility occurs by the reduced hydrogen accumulation at the potential crack initiation sites due to higher irreversible traps. The literature also reported an increase in HIC susceptibility with the increase in reversible trapping sites [55, 56, 57].

2.5. Hydrogen trapping by grain boundaries, dislocations, inclusions and precipitates

Eeckhout et al. reported the hydrogen diffusivity decreases due to the increased trapping by cold deformation in the steel. They also reported an increase in hydrogen diffusivity due to the thermal treatments on those cold-rolled samples [58]. Hence, the intensity of trapping changes

with differences in grain boundaries and dislocations by annealing and cold rolling. However, trapping increases solubility and decreases diffusivity [59, 58]. Findley et al. reported that grain boundaries and dislocations were reversible traps, whereas inclusions and precipitates belong to irreversible traps [35]. The thermal treatments on the material affect the coherency of the precipitates and inclusions with the matrix. The literature states that coherent and semi-coherent precipitates act as reversible trapping sites due to their low binding energy with hydrogen, whereas incoherent precipitates belong to irreversible trapping sites due to their high binding energy with hydrogen [35, 60, 14]. Therefore, inclusions and precipitates can act as reversible and irreversible traps based on their binding energy with hydrogen.

2.6 Effect of grain sizes on hydrogen diffusion, accumulation, and embrittlement

Ichimura et al. show that the highest diffusion rate occurs for intermediate grain size in X70 pipeline steel due to the grain boundary cross effect [61]. It states that hydrogen mobility increases for small grain size due to the increased grain boundary surface area per unit volume, and hydrogen mobility also decreases for small grain size due to increased trapping by more triple junctions. Recently, Yazdipour et al. reported that the higher diffusion occurs in an intermediate grain size of 46 μm, and the lower diffusion occurs in smaller grain size [62]. Bonab et al. reported that preferential hydrogen diffusion occurs through the grain boundaries of pipeline steels [48]. Also, Luu et al. reported preferential hydrogen diffusion through the matrix-inclusion interfaces of pipeline steels [63]. However, the preferential diffusion through the different microstructural features was never compared. Also, the types of hydrogen traps in the steels were never classified based on the visualized hydrogen diffusion path.

The grain refinement reduces the HE susceptibility as the mass of hydrogen per unit grain boundary area is decreased [64, 65]. Recently, Masoumi et al. opposed the previous studies and observed that small grains are more susceptible to HE [66]. Bonab et al. reported that grain boundaries act as reversible traps and provides an easy path for hydrogen mobility. They also reported that grain boundaries increase the HIC susceptibility in X70 pipeline steel [67]. Generally, the contradictory findings on the effect of grain sizes on HE susceptibility also allow the study on the effect of grain sizes on hydrogen diffusion and accumulation in pipelines. The grain refinement by the reduction in grain size occurs as a strengthening mechanism as it increases fracture toughness and strength of the material [68]. As the market requirement for high strength pipeline steel increases, the grain size is expected to be small than the presently used grain size. Hence, the effect of small grains was studied in this research.

2.7 Factors affecting grain growth

The study on the effect of grain size on hydrogen diffusion and accumulation requires a wide range of grain sizes. The different grain sizes for this study were obtained by annealing as-received steel. The reheating temperature and soaking time were the main parameters that influence grain growth during annealing. Seikh et al. reported that the grain size increases with the rise in reheating temperature and soaking time during the annealing of X70 pipeline steels [69]. The authors use three reheating temperatures between 115 ℃ and 1250 ℃ in that study. Also, they use five different soaking times between 10 and 60 minutes. However, the effect of pre-cold rolling before annealing on grain growth was not available during the literature review. Hence, the effect of pre-cold rolling needs to be explored before proceeding with sample preparation.

2.8. Effect of misorientations on hydrogen diffusion, accumulation, and embrittlement

Louthan et al. show the absence of hydrogen trapping by the dislocation densities induced by cold working [70]. Recently, Perng et al. reported that the increased density of dislocations increases effective hydrogen concentration and reduces hydrogen mobility [71]. Hung et al. also reported that cold working increases trapping in X70 pipeline steel, and it is evident from slower permeation and reduced diffusivity [55]. The recent studies reported that dislocation is a trapping site, whereas the ancient study reported its null effect for hydrogen trapping. Also, the previous studies reported that dislocation acts as a reversible trap and can increase the HE susceptibility [55, 56, 57]. Remarkably, the effect of misorientations, which indicates the amount of induced deformation, were never considered in the previous studies of hydrogen diffusion and accumulation.

The previous studies reported a preferential diffusion of hydrogen through the deformed regions of the microstructure [72, 73]. Also, there was a preferential diffusion of hydrogen through the slip lines and slip bands of the deformed materials [74, 75]. However, the preferential diffusion through the different deformed microstructural features was never compared. Also, the types of hydrogen traps in the deformed steels were never classified based on the visualized hydrogen diffusion path. The small change in the hydrogen microprint technique procedure can cause a difference in the image quality of the visualized hydrogen diffusion path. Also, the interpretations from the observations become different with modified procedures. Hence, the routine procedures for the hydrogen microprint technique by Perez et al. were modified by Luu et al. to get new findings of the hydrogen diffusion path. [63, 76].

2.9. Experimental factors affecting hydrogen permeation experiment

The electrochemical hydrogen permeation (HP) experiment was used to quantify the hydrogen diffusion parameters that can predict and help to understand the HE [77]. The control of different experimental variables in the HP experiment allows in generating reliable measurements. The variables include test setup, charging current density, oxidation potential, palladium coating on the sample, recombination poison, pH of the electrolytes, temperature, and pressure gradients across the sample. The quantity of the recombination poison, pH of the electrolytes were easily maintained in all experiments as the source of chemicals, and the measuring instruments were not changed during the research. Also, the applied oxidation potential had minimum variations due to the feedback system of the potentiostat. The test setup was open to atmospheric pressure during the experiments, and it avoids any pressure gradient across the sample.

2.9.1. Investigations of the role of hydrogen charging current density

Li et al. observed that the steady-state permeation current increases with the charging current density as more hydrogen atoms were injected into the charging cell. Hence, the permeation rate was accelerated, and the breakthrough time for the hydrogen atoms from the entry to exit was shortened for the higher charging current density [78]. Breakthrough time is utilized for the removal of the oxide film from the cathode surface of the sample. There were a couple of other studies that show an increased hydrogen diffusivity through the sample when the applied cathodic charging current was increased [79, 80]. Hence, the increased hydrogen charging current density in HP experiments increases the steady-state current, hydrogen permeability, effective hydrogen diffusivity and decreases the breakthrough time in materials.

2.9.2. Effect of palladium coating on the testing surface

The high permeability of the palladium membranes makes them ideal for hydrogen diffusion applications like membrane reactors and fuel cells. International Organization for standardization had mentioned the need for palladium coating on either side of the polished samples to get repeatable results and to avoid the oxide formation in the HP tests [81]. Also, Manolatos et al. reported the need for palladium coating on the oxidation side to ensure the reliability of the hydrogen flux measurement [82]. The absence of a palladium coating avoids the instantaneous oxidation and allows the formation of molecular hydrogen at the detection side. Hence, the actual permeation current is reduced in the absence of palladium coating. Zhang et al. reported that the application of a palladium coating of 30 nm on the surface of a

composite membrane enhances the hydrogen permeation rate of that membrane [83]. However, Wojciech et al. reported that the increase in coating thickness decreases the quantity of diffused hydrogen [84]. Hence, a thin palladium coating should be used in the HP experiments.

2.9.3. Effect of temperature on permeation characteristics

Wang et al. reported that the steady-state permeation current density, steady-state flux, and permeation rate increases with increasing temperature [85]. Another study by Jeon et al. also reported that hydrogen flux was directly proportional to the temperature at constant pressure [86]. Si et al. provided a similar observation on the permeation current in their study on different types of steels for four different temperatures between 15 º C and 45 º C [87]. Therefore, the permeability of the materials increases with an increase in temperature during the HP experiment.

CHAPTER 3

MATERIALS AND METHODOLOGY

3.1. Overview

This chapter contains details of the supplied materials and discussion of the experimental methodology used in this research. The details of the prepared samples were also presented in this chapter.

3.2. Materials

The materials used in this research were supplied by Evraz North America, Regina, Canada. The different experiments for fulfilling the objective of this thesis used two batches of API 5L X70 pipeline steel. The first batch of pipeline steel was supplied to the research group in 2012 and will be hereafter known by X70-1. The second batch of pipeline steel, X70 WH, was provided to the research group in April 2017 and will be known by X70-2. Table 3.1 shows the chemical composition of both steels.

Table 3.1. Chemical composition of the X70 pipeline steels (wt %).

Pipeline Steels	C	Mn	Si	Mo	Ti	Cr	Cu	Ni	V	S	P	N
X70-1	0.025	1.65	0.26	0.175	0.015	0.07	0.21	0.08	0.001	0.0025	0.010	0.008
X70-2	0.047	1.65	0.18	0.247	0.022	0.06	0.29	0.07	0.001	0.0018	0.009	0.009

3.3. Methods for sample preparation and validation

The two batches of supplied materials were in the form of big rectangular plates. The experiments were completed with the supplied material by preparing samples of required properties and dimensions. The change in material property is necessary to achieve the research objectives. Also, the experimental test setups require samples with standard dimensions. The change in properties and dimensions of the supplied material were achieved by methods like annealing, cold rolling and material cutting. Also, the prepared samples were characterized to validate the changes in material properties. The mounting of the sample facilitates the secure handling of the sample during polishing, etching and characterizations. Also, there is an intermediate coating on the sample before the hydrogen permeation experiment. This section

is used to familiarize the methods and associated machines used at different stages of the sample preparations.

3.3.1. Cutting

The bulk rectangular plate was cut into long strips along the width direction. Strips were made from the mid-thickness at the segregation zone and the top layer of steel. Then, the strips were cut into small samples before or after thermomechanical treatments. The individual strips from the bulk plate were chopped using a DoAll, 3612 – 3, Vertical Band saw with a sufficient cooling system. Similarly, small samples from the individual strips were obtained using a Buehler, Model 95-C1800, abrasive cutter with an adequate cooling system.

3.3.2. Annealing

The samples for studying the effect of grain size on hydrogen diffusion and accumulation in the X70-1 steel were prepared by annealing the as-received steel. The chopped samples from the steel strips were annealed in a Thermo Scientific, F48015 – 60 model, muffle furnace. The furnace was manually controlled, and there was oxidation at the sample surface as annealing occurs in regular atmosphere.

3.3.3. Cold rolling

Samples for studying the effect of grain misorientation on hydrogen diffusion and accumulation in the X70-2 steel were prepared by cold rolling the as-received steel. During plastic deformation by cold rolling, most of the mechanical energy is converted into heat energy. However, a fraction of the mechanical energy is stored as strain energy associated with the dislocations in materials. The strips from the rectangular bulk plate were cold-rolled at the room temperature. The cold-rolling used a Stanat, Model TA-31, Rolling mill to induce different levels of deformation in each sample.

3.3.4 Mounting

The small and sharp samples were mounted after annealing and cold rolling. The mounting of samples allows safe and secure handling during polishing and etching. Also, the mounted samples offer secure and fast fixing during characterizations. All the samples were hot mounted by Buehler, SimpliMet XPS1 automatic compression mounting system at a pressure of 4200 psi and temperature of 350 °F with five minutes of heating and cooling. Also, the mountings were broken after characterization, and the samples were repolished for other experiments.

3.3.5. Polishing

Polishing enriches the appearance of the samples before characterization. Hence, the annealed and cold rolled samples were polished to improve the surface evenness and to remove the oxidation layer. All the samples in this research were polished with the same sequence of silicon carbide emery paper using a Struers, Labopol-5, automatic polishing machine. The sample polishing was started with a 180 grit silicon carbide paper and followed by 360, 500, 800, 1200, and 2400 silicon carbide papers. Further, the samples were polished with 3, 1, and 0.04 μm diamond paste suspensions. Remarkably, the thin square sample used for the hydrogen permeation and hydrogen microprint technique experiments were polished on either side using the same polishing procedure.

3.3.6. Etching

The chemical process to reveal the microstructure of samples after metallographic grinding and polishing is known as etching. During etching, the contrast of etched surface is improved to see the details on it using microscopic inspection. All steel samples in this research were etched with a 4% nital solution for 10 seconds. The etched samples were rinsed with water and ethanol to clean from the residues of etchant. Finally, the cleaned samples were dried and proceeded for characterizations using a microscope.

3.3.7. Characterization

The annealed and cold rolled samples were characterized to quantify grain sizes and misorientations. All samples undertake some of the characterizations at different stages of the sample preparation and experimentation. The characterizations, as part of this research, include the microstructural, crystallographic, and chemical characterizations. The samples require either microstructural or crystallographic characterizations before the hydrogen permeation and hydrogen microprint technique experiments to measure the induced properties. However, there were additional microstructural and chemical characterizations after the hydrogen microprint technique experiments to visualize and validate the hydrogen diffusion path.

3.3.7.1. Microstructural characterization

Microstructural characterizations were done using an optical microscope (OM) from Nikon Eclipse, MA 100 and a scanning electron microscope (SEM), Hitachi SU6600, equipped with electron backscatter diffraction (EBSD) and energy-dispersive X-ray spectroscopy (EDS) detectors. The OM characterization uses a horizontally placed sample without any sample

holder. However, a flat sample holder places the sample in a horizontal plane during SEM characterization. Micrographs were taken using PAX-it software and SU6600 software in OM and SEM. The grain sizes, phases, and inclusions in the samples were characterized using OM and SEM. The average grain size was estimated using the lineal intercept technique or Heyn's technique [88]. This technique counts the number of grain boundaries intersecting a random line drawn through the micrograph, and the average grain size is founded by dividing the length of the line by the number of intersections.

3.3.7.2. Crystallographic characterization

The crystallographic characterizations were done using a Hitachi, SU 6600 field emission SEM with an Oxford Instruments, Nordlys nano EBSD detector, by the EBSD measurements. The pre-tilted sample holder places the sample at an inclination of 70° from a horizontal plane during the EBSD measurements. The Kikuchi diffraction pattern from a region in the sample is collected from the EBSD analysis and the corresponding crystal orientations were determined. The diffraction patterns were acquired using AZTEC 2.0 data acquisition software. The grain size and kernel average misorientation (KAM), an indication of the amount of induced deformation, were measured by the post-processing of the EBSD data. The post-processing of raw EBSD data uses tango and Mambo software.

3.3.7.3. Chemical characterization

Chemical characterizations were done using the EDS measurements, and it uses a Hitachi, SU 6600 field emission SEM with an Oxford Instrument, EDS detector. During the EDS characterizations, the samples were placed in the horizontal plane using a flat sample holder. EDS is used in identifying and quantifying elemental composition in which the detector analyses the wavelengths of the X –rays corresponding to each element when the atoms of the samples were excited by an electron beam. The EDS measurements were done using the AZTEC 2.0 data acquisition software. The elemental composition of the non-metallic inclusions in the steel microstructure and reduced silver particles in the hydrogen microprint technique experiments were identified and quantified using EDS measurements.

3.3.8. Coating

The high permeability of palladium makes it an excellent choice for coating the steel surface without affecting the hydrogen diffusion through it. The palladium coating on either side of polished samples suppresses oxide related problems and allows the complete oxidation of

diffused hydrogen in the hydrogen permeation experiment. Also, the palladium layer on the hydrogen charging side affects the subsurface hydrogen concertation and minimizes the variations in surface conditions of the sample and the permeation results. Similarly, the coating on the oxidation side of the sample increases the efficiency of hydrogen atom oxidation, and this oxidation is at a less potential than for the uncoated sample.

Electrochemical methods of coating the sample with a thin layer of palladium can introduce hydrogen into the sample and affect the experimental results. Hence, the samples were coated with palladium by sputtering in a vacuum. Sputtering uses a Quorum, Q150T model, turbomolecular-pumped coating system with a Ted Pella, 91119 palladium target of 57 mm diameter and 0.1 mm thickness. As an increased coating thickness should not affect the permeation results, the palladium layer was of 20 nm thickness. It is smaller than the 100 nm coating thickness obtained by the electrochemical method [89]. The coating system supplies a 20 mA sputter current to obtain a standard coating profile with a predetermined coating thickness of 20 nm. Hence, the coating system automatically terminates each profile after achieving the required coating thickness. The standard profile took 58 to 62 seconds to finish each coating. The 50 mm diameter stage of the coating system can carry three samples at the same time, and each side of the sample was separately coated. Hence, both sides of the three samples were covered with pallidum by executing two standard profiles.

3.4. Sample preparation for study on the effect of grain sizes

The as-received X70-1 steel was a rectangular plate with dimensions of 150 x 80 x13 mm. This batch of steel was used for investigating the effect of grain size on hydrogen diffusion and accumulation. Also, the mid-layer at the segregation zone and the top-layer from the steel were separately considered in this study. Hence, individual strips of 20 x 80 x 2 mm were cut for either layer, as shown in Figure 3.1. The steel strip of 2 mm in the mid-layer includes 1 mm thickness from either side of a centerline in the X70-1 plate thickness. These strips were cut into small samples of 20 x 20 x 2 mm and were annealed. Figure 3.2 shows the annealing program that enables to obtain different grain sizes in this study. The thermal treatment includes four different annealing cycles from A1 to A4. The samples were annealed at four different pre-defined temperatures in each annealing cycle. After 5 minutes of heating inside the furnace, the samples were cooled to the room temperature, RT, inside the oven. The annealed samples were polished and etched after mounting. Later, the samples were characterized using OM and SEM to measure the grain sizes and to understand the microstructure.

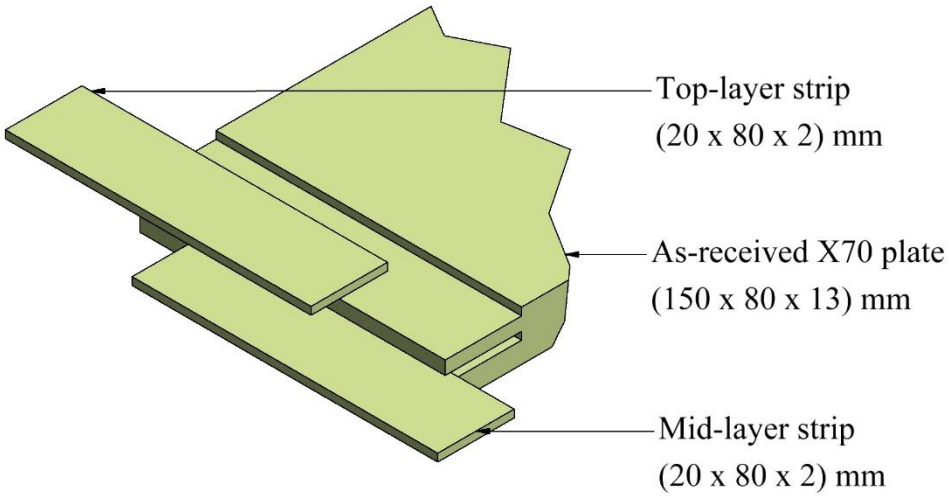

Figure 3.1. Top-layer and mid-layer from the X70-1 steel.

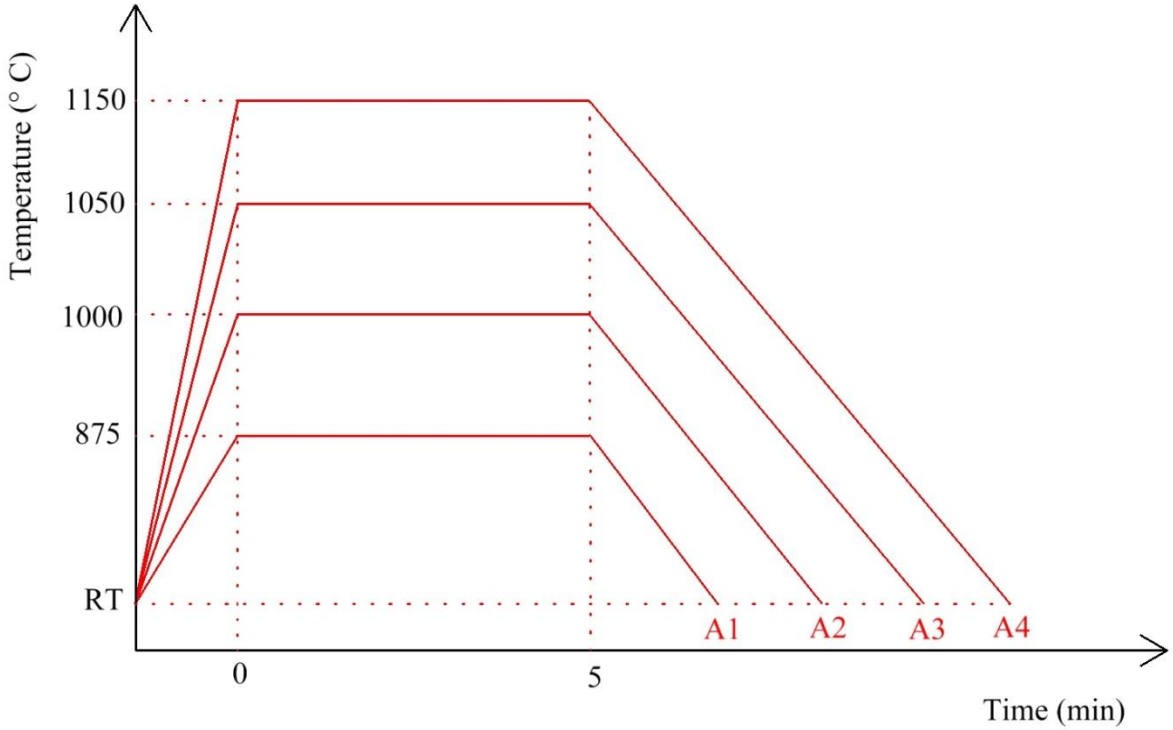

Figure 3.2. Annealing program to obtain different grain sizes in X70-1 steel.

The mountings of the samples were broken after characterizations and repolished on either side to make the final sample thickness to 1 mm for the hydrogen permeation and hydrogen microprint technique experiments. The repolished samples were coated with palladium before the hydrogen permeation experiments. The as-received sample and the four samples after annealing were the five samples prepared from each layer of the X70-1 steel in this study. Table 3.2 shows the details of the samples from each layer. Thirteen samples were prepared from X70-1 steel, and ten of them were used for the hydrogen permeation experiments.

Table 3.2. Details of the annealed X70-1 steel.

Sample name	Layer	Annealing cycle	Number of samples	Experiment name
T1	Top	As-received	1	HP
T2	Top	A1	1	HP
T3	Top	A2	1	HP
T4	Top	A3	1	HP
T5	Top	A4	2	HP and HMT
M1	Mid	As-received	2	HP and HMT
M2	Mid	A1	1	HP
M3	Mid	A2	1	HP
M4	Mid	A3	1	HP
M5	Mid	A4	2	HP and HMT

3.5. Sample preparation for study on the effect of misorientations

The as-received X70-2 rectangular steel plate had dimensions of 285 x 240 x 23 mm. This batch of steel was used for investigating the effect of misorientation on hydrogen diffusion and accumulation. The center segregation zone that occurs after solidification was unavoidable in hot-rolled pipeline steels. Hence, the top layer of the steel was cold-rolled to make samples without any segregation zone.

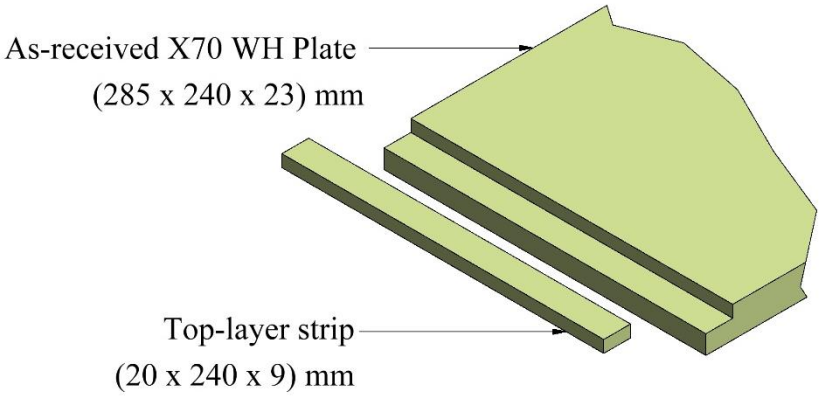

Figure 3.3. Top layer from the X70-2 steel.

Figure 3.3 shows a strip of 20 x 240 x 9 mm taken from the top layer of the as-received X70-2 plate. The strip was cold-rolled to obtain samples with different misorientations. The required thickness reductions in cold-rolling were obtained after multiple passes through the rollers. The

thickness reduction in each pass was less than 0.08 mm. The multiple pass reduction was used to reduce the inaccuracies by spring back and to avoid the cracking that occurs in a single pass reduction. Figure 3.4 shows the cracking of steel after a single pass reduction. An abrasive cutter was used to slice the cold-rolled strip into samples of 20 x 20 x 2 mm after each degree of cold rolling, whereas a vertical band saw was used to obtain a 2 mm thickness from the top-layer of the cold-rolled strip. The cold-rolled samples were initially mounted and later polished to a mirror finish. Finally, the samples undergo EBSD characterizations to quantify the KAM.

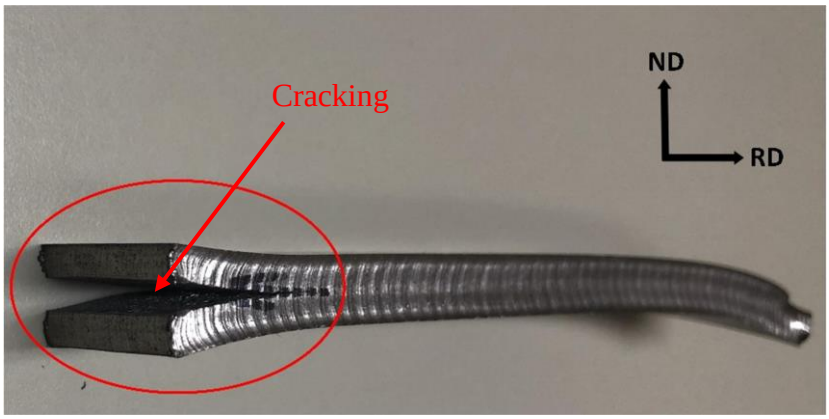

Figure 3.4. Cracking in X70-2 steel after single pass reduction by cold rolling.

The mountings of the samples were broken after characterization to polish either side of the samples to a final thickness of 1 mm required for the hydrogen permeation and hydrogen microprint technique experiments. The polished samples were immediately coated with a thin palladium layer before the hydrogen permeation experiment. Table 3.3 shows the details of the samples after the cold rolling experiments. Seven samples were prepared from X70-2 steel, and five of them were used for the hydrogen permeation experiments.

Table 3.3. Details of the cold-rolled X70-2 steel.

Sample name	Initial thickness	Final thickness	Degree of cold rolling	Number of samples	Experiment name
A	9	9	0	2	HP and HMT
B	9	7.2	20	1	HP
C	9	5.4	40	2	HP
D	9	3.6	60	1	HP
E	9	1.8	80	1	HP and HMT

3.6. Methods for hydrogen diffusion and accumulation studies

The hydrogen permeation and hydrogen microprint technique experiments were used in this research to understand the effect of grain size and misorientation on hydrogen diffusion and accumulation. The hydrogen permeation experiment is used to measure the diffusion parameters and hydrogen trapping sites, whereas the hydrogen microprint technique is used to visualize the hydrogen diffusion path. In the hydrogen permeation experiment, the diffused hydrogen is oxidized and simultaneously measured. In the hydrogen microprint technique experiment, diffused hydrogen is reacted with an emulsion coating, and it enables to visualize the hydrogen escaping sites. This section explains the theory, test setup, testing procedure, expected outcomes and uncertainties in measurements.

3.6.1. Hydrogen permeation

The electrochemical hydrogen permeation (HP) experiment was initially developed at the Electrochemistry Laboratory, the University of Pennsylvania, by Devanathan and Stachurski in 1962 for the instantaneous recording of hydrogen permeated through a palladium membrane [90]. Later, ISO had released a standard for the method of measurement of hydrogen permeation and determination of hydrogen uptake and transport in metals by an electrochemical technique [81]. There were plenty of works using hydrogen permeation experiments for the last 57 years. The research group under Dr. Szpuar used a test setup similar to the Devanathan and Stachurski test setup for the permeation study. In this research, the same test setup was used after additional modifications for obtaining more repeatable results. The below section explains the hydrogen permeation experiment.

3.6.1.1. Hydrogen permeation theory

The immersed steel specimen in dilute sulfuric acid generates hydrogen, and the steel absorbs the same hydrogen [91]. Also, the supply of cathodic current to the steel in an electrochemical cell can control the generated atomic hydrogen [92]. The hydrogen produced diffuses through the steel, and some amount of hydrogen is accumulated in the trapping sites of the material. The accumulation of hydrogen by the trapping sites eventually leads to hydrogen embrittlement. Even though there were many studies about hydrogen diffusion in steel, all of them used the Devanathan and Stachurski setup. This method creates a concentration gradient between two sides of the sample, and hydrogen was made to diffuse from one side of the sample to another side. The typical HP test setup, according to Devanathan and Stachurski setup, had two electrochemical cells running concurrently using the same sample as the working electrode

of both cells. The role of one electrochemical cell is to generate the hydrogen in one side of the sample, and another electrochemical cell is responsible for the simultaneous oxidation of the hydrogen that diffuses through the sample [93, 94]. The generation and oxidation of hydrogen in those two electrochemical cells are expressed [95, 96] using equations 3.1 and 3.2.

$$H^+ + e^- = H \qquad (3.1)$$

$$\mathrm{H} = \mathrm{H}^+ + \mathrm{e}^- \qquad (3.2)$$

From the literature, there were standard equations to calculate the diffusion parameters, and those equations were defined below. The effective diffusion coefficient is the quantity of hydrogen that will be diffusing through a unit cross-sectional area of the steel sample in unit time due to the difference in concentration between two surfaces. The steel sample act as a porous media, and hence, the effective diffusion coefficient is considered rather than the bulk diffusion coefficient. The thickness of the sample is 'L' in centimeters, and 'T_L' is the time lag in seconds, and they were calculated from the hydrogen permeation curve. If there is a simultaneous rate of permeation through a material, then the effective hydrogen diffusion coefficient measured in square centimeters per second is calculated by the time lag method [97, 81] using the equation 3.3, as given by,

$$D_{eff} = \frac{L^2}{6\,T_L} \qquad (3.3)$$

Permeability is the rate of hydrogen flux passing through the steel sample due to the difference in pressure between two surfaces. If Faraday's constant, 'F' is 96,500 Coulombs/mole [98, 99], 'A' is the exposed area of the sample to the electrolyte in the electrochemical cell measured in square centimeters, and 'I_∞' is the steady-state current measured in microamperes. Then, the hydrogen permeability, '$J_\infty L$' measured in moles per centimeter per second is calculated [67, 100] using equation 3.4, as given by,

$$J_\infty L = \frac{I_\infty\, L}{FA} \qquad (3.4)$$

Apparent solubility is the volume of hydrogen that will be dissolving in a unit volume of the steel sample to form a saturated sample in the provided experimental conditions of constant pressure and temperature. Also, the permeability is the product of the effective diffusion coefficient and apparent solubility. If surface hydrogen is in thermodynamic equilibrium with subsurface hydrogen, then the apparent hydrogen solubility, 'C_{app}'measured in moles per cubic centimeters is calculated [99, 100] using equation 3.5, as given by,

$$C_{app} = \frac{J_\infty L}{D_{eff}} \qquad (3.5)$$

Some amount of hydrogen remains in the trapping sites of the steel and is not diffusing. If the lattice diffusion coefficient, 'D_L' of the trap free bcc iron was taken as 1.28 x 10^{-4} square

centimeters per second. The number of electrons transferred in each mole is '*n*', and it is taken as 6.02 x 10^{23} electrons per mole. Then, the total number of hydrogen trapping sites, 'N_t' measured per cubic centimeter of the tested sample is calculated [67, 99] using equation 3.6, as given by,

$$N_t = \frac{n\,C_{app}}{3}\left\{\frac{D_L}{D_{eff}} - 1\right\} \qquad (3.6)$$

Every polarization of the hydrogen permeation experiment involves successive hydrogen charging and discharging. If the same sample is used for two simultaneous polarizations, all the irreversible traps are saturated after the first polarization for the supplied cathodic current in the charging cell. Therefore, the reversible traps are actively participating in the second polarization. Based on the previous research from Bonab et al. [67], if the density of the total and reversible trapping sites be N_t and N_r, and are measured per cubic centimeter of the tested sample in the first polarization and second polarization respectively. Then, the number of irreversible trapping sites, N_{ir}, measured per cubic centimeter of the tested sample is given by equation 3.7, as provided by,

$$N_{ir} = N_t - N_r \qquad (3.7)$$

3.6.1.2. Hydrogen permeation cell assembly

The ISO 17081 standard [81] is the basis for the HP cell assembly, and Figure 3.5 represents the schematic diagram of the same. It contains two identical glass beakers with a small flange at its bottom. The glass cup on the left side is the charging cell. The production of hydrogen for diffusion takes place at this charging cell. The glass cup on the right side is the oxidation cell, where the diffused hydrogen is oxidized. The charging cell electrolyte is 250 ml mixture of 0.1 M sulfuric acid (H_2SO_4). The electrolyte is also added with 3 grams per liter of ammonium thiocyanate, and it acts as a hydrogen recombination poison. Hence, it promotes the ability of atomic hydrogen to enter the material by retarding the hydrogen bubble formation. The oxidation cell electrolyte is 250 ml of 0.1 M sodium hydroxide (NaOH). There were separate lids for both charging and oxidation cell. Also, the lids have fixed electrode positions to maintain the uniformity of cell geometry in all experiments. The graphite rod of 5 mm diameter act as the counter electrode and saturated calomel electrode with 3 M potassium chloride act as the reference electrode in the test setup. During the entire testing, there is an inert argon gas supply to both cells for deaerating the system from oxygen. Both lids contain two plastic connectors for the argon gas in and out. The argon gas intake connector is placed away from the sample and extended into the electrolyte. The sample is placed at the gap between the flanges of each cell, and a nylon ring is used to assemble the sample firmly between

those flanges. Also, rubber O –Rings are kept between the sample and flanges to avoid any electrolyte leakage through flanges. The design of the flange and O –Ring is in such a way to provide a circular area exposing of 1 square centimeter between the sample and the electrolyte in glass beakers.

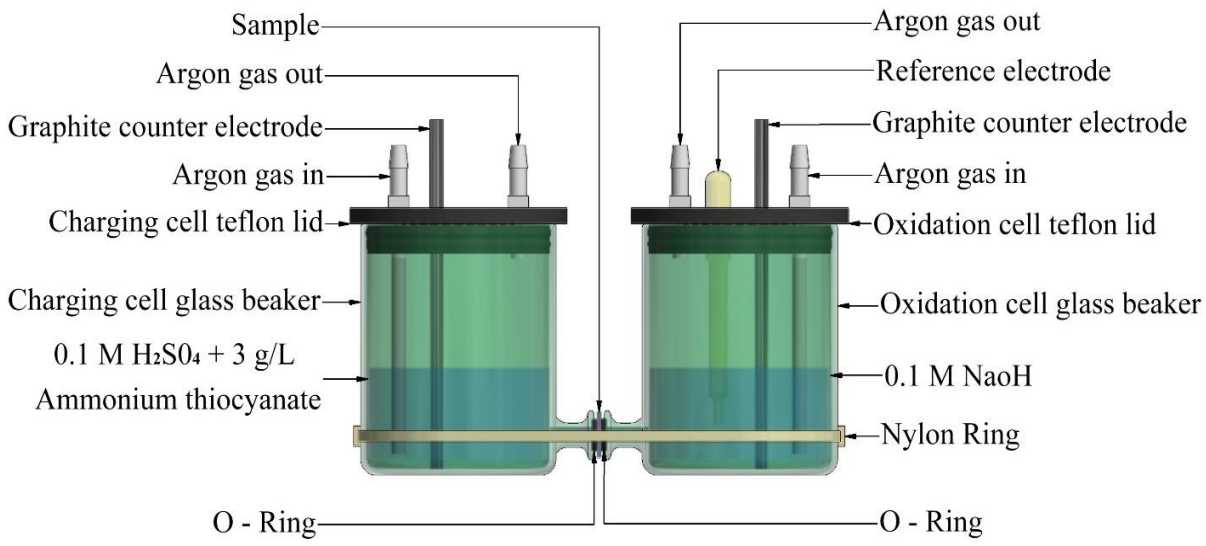

Figure 3.5. Schematic diagram of HP cell assembly.

Figure 3.6 shows the dimensions of the sample assembled with O – Rings. There are two O – Rings on either side for the HP test setup. The samples used for the permeation experiment is polished to the required surface finish and coated with a 20 nm thickness of palladium on either side of the sample. The graphite counter electrode in the charging cell, the electrolyte and the sample itself acts as the working electrode to form the first electrochemical cell where the production of hydrogen occurs. The oxidation cell lid has a counter electrode extending into the oxidation cell electrolyte, a reference electrode, and the sample itself acting as the working electrode again. This three-electrode system forms the second electrochemical cell where diffused hydrogen is oxidized. When the large current passes through an electrode, its potential changes, and it happens to the counter electrode of the oxidation cell when it forms out of a two-electrode system. The utilization of the three-electrode system provides careful control and measurement of both potential and current through the cell. Hence, the sample and the reference electrode maintains the required potential for the oxidation of hydrogen. A large amount of instantaneous oxidized current flows through the counter electrode during the oxidation of hydrogen. Hence, the potential of the reference electrode is constant during the entire HP experiment.

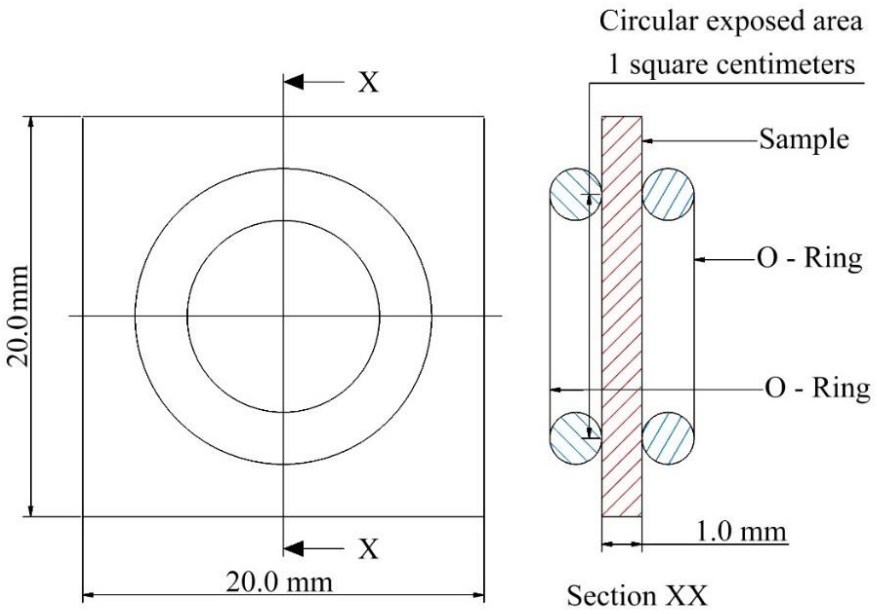

Figure 3.6. Dimensions of HP sample assembled with O – Rings.

3.6.1.3. Test procedure for the hydrogen permeation experiment

The hydrogen permeation cell assembly is connected to the required power sources to work as the actual permeation system, as shown in Figure 3.7. The charging cell is connected to the Instek direct current power supply to deliver 5 mA constant current in that system and to produce the hydrogen required for diffusion. The positive anode and negative cathode of the power supply are connected to the graphite counter electrode and the working sample in the charging cell. The second electrochemical cell forms in the oxidation cell and it is connected to a Gamry Potentiostat, G750 model, to supply a constant potential of 250 mV between the working electrode and the reference electrode to oxidize all the hydrogen diffused through the sample. The positive working electrode and the negative counter electrode of the Gamry potentiostat are connected to the working sample and graphite counter electrode. Also, the reference electrode in the Gamry is connected to the standard calomel electrode.

When both electrochemical cells work, the surface of the sample in the charging cell act as a cathode and the surface of the sample in the oxidation cell act as an anode at the same time for the respective cells. Also, the instantaneous current flowing through the counter electrode of the Gamry represents the amount of oxidized hydrogen, and the Gamry software is used to record the same. The data is recorded every two seconds as the behavior of each sample is significantly different. The permeation experiments use the potentiostatic experiment in version 6.33 of the Gamry software for providing the required voltage between the electrodes to measure the instantaneous current in all the experiments.

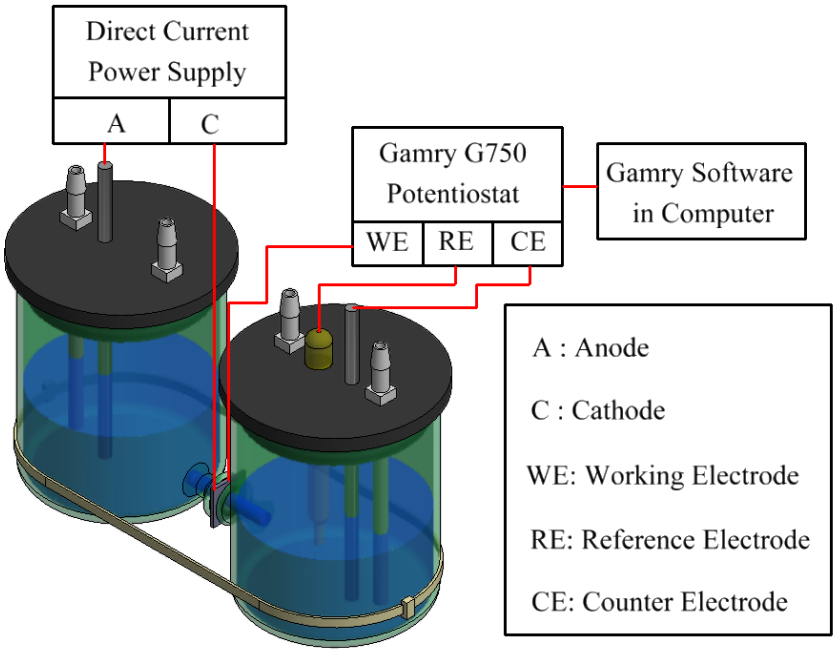

Figure 3.7. Schematic diagram of the HP test set up.

The electrochemical cells start working after the required connections between the electrodes and the corresponding power supplies. The experiment is started by pouring the electrolyte into the oxidation cell. The residual hydrogen in the system is oxidized with the supply of anodic potential to the sample. This residual oxidation of hydrogen is continued until the Gamry records a stabilized oxidation current close to 0 µA. The residual current usually takes 5 hours to reach a low oxidation current, and it varies between the samples. When the residual hydrogen is fully oxidized, the charging cell is poured with the electrolyte. Then, the second electrochemical cell is simultaneously started by providing the required cathodic current to the sample. When the charging cell produces hydrogen, it is immediately diffused into the oxidation cell and concurrently oxidized. Hence, the measured oxidized current is increased in the Gamry software. Once this measured current reaches a stable value in the Gamry, the cathodic flow is disconnected. Then, the measured oxidized current begins to reduce gradually. The hydrogen discharge from the material, indicated by the decline in oxidation current, takes 3 hours for annealed samples. However, the deformed samples take more time to bring down the oxidized current close to a stable 0 µA. At the same time, the charging solution is emptied to avoid corrosion in the working sample. The cathodic hydrogen charging and discharging allows the growth and decay of oxidized current. It is considered as a typical hydrogen permeation curve after first polarization. The experiment is further continued to get a second permeation curve by a second polarization after the first permeation curve. It enables the measurement of reversible and irreversible trapping sites.

3.6.1.4. Expected results from the hydrogen permeation experiment

All results from the hydrogen permeation experiment depend on the permeation curves obtained from the Gamry software. Figure 3.8 shows the typical hydrogen permeation curve after double polarization in the hydrogen permeation experiment [67, 100]. The permeation curve from the first polarization shows a gradual growth in the oxidizing current. Then, the permeation curve reaches a steady-state for the supplied cathodic current in the testing conditions. The oxidizing current is decayed by the removal of supplied cathodic current. Hence, a permeation curve for the first polarization is obtained. The parameters that can be obtained from the permeation curve were the steady-state current ($I\infty$), and time lag (T_L). The steady-state current is measured as the stable oxidation current from the permeation curve. The time lag is the time passed until the oxidized current becomes 0.63 times of the steady-state current. The other parameters, like permeability, effective diffusivity, apparent solubility, and density of total hydrogen trapping sites, are calculated using the values of steady-state current, time lag and dimensions of the sample. The density of irreversible trapping sites is obtained after the second polarization [67]. The second permeation curve from the second polarization is smaller than the first one as the irreversible trapping sites are not active in the second polarization. All the parameters that are deliverable from the first polarization are also deliverable in the second polarization. Also, the additional information on irreversible trapping sites is available after the second polarization.

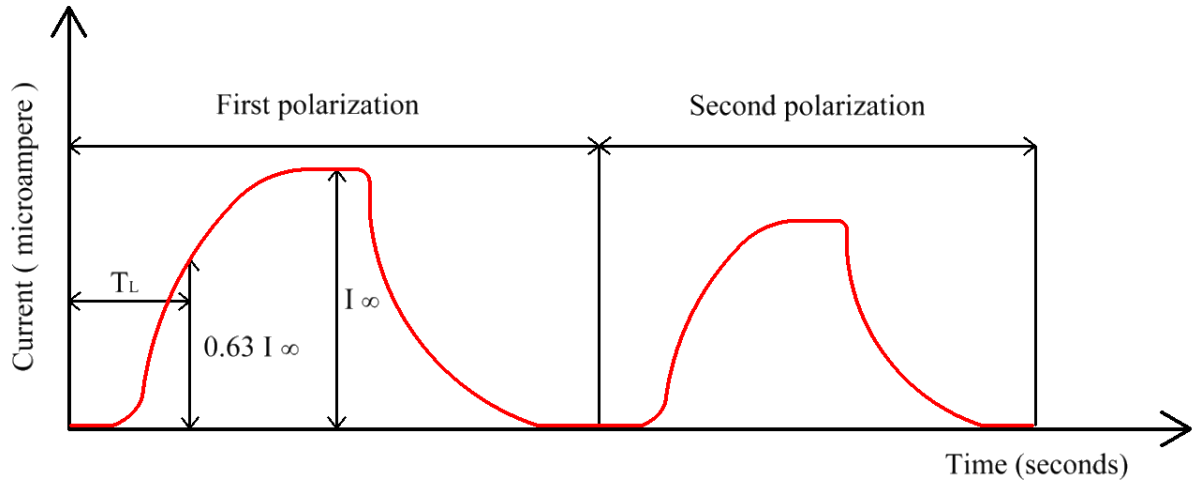

Figure 3.8. Typical hydrogen permeation curve after double polarization [67, 90].

3.6.1.5. Uncertainty in measurements

The difference between true and measured values is known as measurement error. The approximate value of the measurand is obtained from the measurement. Hence, the measurement is complete when it is supplemented by the uncertainty of measured value [101].

Yu et al. also reported that measurement error consists of imperfections in the method of measurement, observer, measured object and measuring instrument. Systematic error either overestimate or underestimate the results of measurements in a predictable way, and it occurs with a particular measuring instrument or experimental technique. The errors from data acquisition (A), calibration (C), and resolution (R) fall under systematic errors. Random errors occur from unpredicted events on the measurement, and it affects the precision (P) of the measured results. Uncertainty describes a range of values inside which the true value is expected to fit with some level of confidence. It should address the systematic and random errors, and therefore, it is the most appropriate way of expressing the accuracy of the results. According to Rabah et al. [102], If the law of propagation of error estimates the level of uncertainty of every measured parameter in the permeation experiment at a 95% confidence interval, then the combined uncertainty, *U*, in the measurement is given by equation 3.8.

$$U = \sqrt{A^2 + C^2 + R^2 + P^2} \qquad (3.8)$$

However, measurements often avoid systematic errors in uncertainty measurement due to its negligible contribution [103]. When random error alone contributes to uncertainty measurement, it is a reflection of the precision of the instrument. If *t* is the student test at a 95% confident interval, σ is the standard deviation, *N* is the number of data sets, λ is the degree of freedom given by $\lambda = N-1$, then the uncertainty of the measurement is calculated by the reduced equation 3.9, as provided by,

$$U = \sqrt{P^2} = P = \frac{t_{\lambda,95\%}\sigma}{\sqrt{N}} \qquad (3.9)$$

From equation 3.1, the supplied current is directly proportional to the produced hydrogen, the diffused hydrogen, and the oxidized hydrogen. However, some of the produced hydrogen atoms in the oxidation cell escape as a hydrogen bubble even in the presence of a recombination poison. Figure 3.9 shows the images of a typical bubble at various stages in the charging cell. This formation of the bubble and its free escape usually takes 3 to 5 minutes in different experiments. The supplied cathodic current is decreased by 0.5 to 0.75 milliamperes during the bubble formation. Equation 3.1 also shows that the supplied cathodic current is directly proportional to the steady-state current. Hence, the calculated uncertainty in the supplied cathodic current indicates the uncertainty in the steady-state current from the Gamry software that was calibrated with a universal dummy cell. The uncertainty for the measured time lag is taken as the maximum uncertainty from a data set of three measurements in the same sample. The method of propagation of uncertainty [103] is used for the uncertainty calculation of other diffusion parameters and different types of trapping sites.

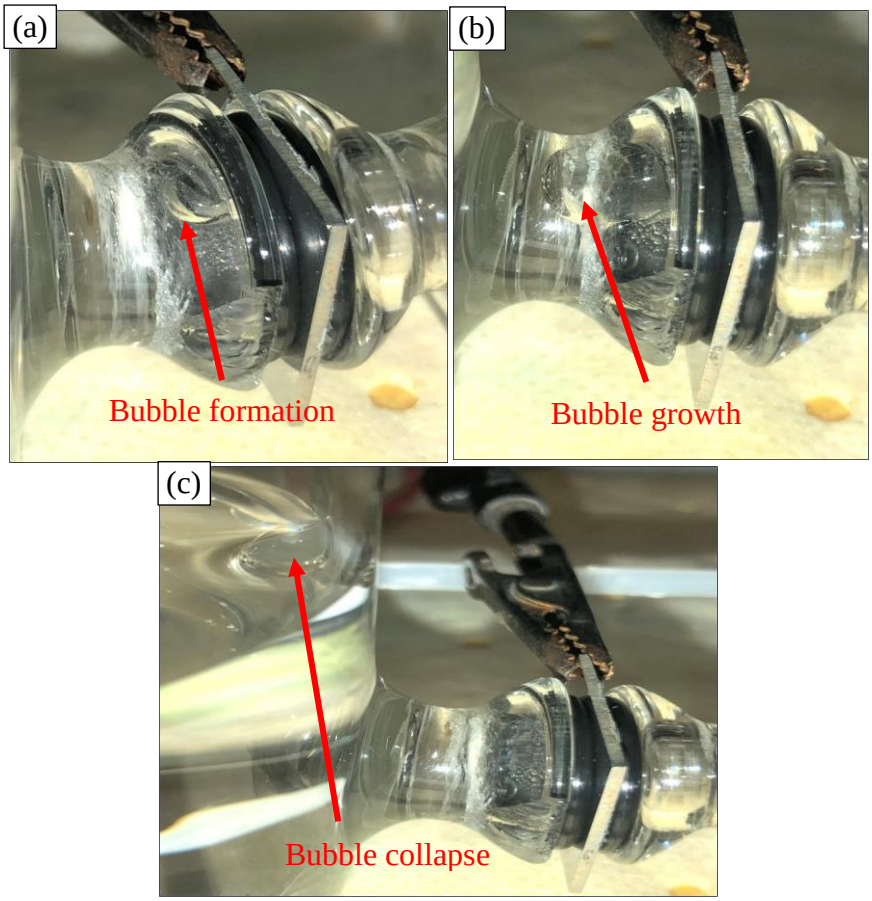

Figure 3.9. Hydrogen bubble in charging cell: (a) formation (b) growth and (c) collapse.

3.6.2. Hydrogen microprint technique

The hydrogen microprint technique (HMT) experiment was initially developed at the National Atomic Energy Commission Laboratory, Argentina, by Pérez and García in 1982. It is used for detecting hydrogen diffusion and understanding its relationship with microstructure [76]. There were several techniques like hydrogen bubble analysis, neodymium film technique, and autoradiography distribution for analyzing the hydrogen diffusion through materials. However, HMT is preferred above other methods due to its simplicity and precision [104, 63]. Also, it is recommended to conduct the HMT experiment after the hydrogen permeation experiment for the hydrogen embrittlement studies of metals and alloys [104]. There were many studies based on HMT experiments for the last 36 years. However, the HMT experiment lacks an international standard.

As validation of the permeation results often uses HMT, Luu and Wu, in 1995, introduced a test setup for the HMT experiments. They modified the hydrogen permeation test setup for simultaneous hydrogen charging and corresponding hydrogen diffusion through an emulsion

coated sample [63]. The previous HMT experiments conducted in Dr. Szpunar's research group used the method of noticing the hydrogen evolution using an emulsion coating on a previously hydrogen charged sample. It is the same method used by Pérez [76]. The demonstrations in this research work allow simultaneous hydrogen charging and corresponding hydrogen diffusion using a test setup. Additionally, the HMT experiment in this research work allows the immediate discharge of hydrogen through the emulsion coated sample for an extended time after the cathodic hydrogen charging. Hence, the reversible hydrogen completely diffuses from the sample during the HMT experiments. Even though there were many HMT research in the past, there were only a few instances where HMT experiments are used to investigate the hydrogen diffusion in pipeline steels [48, 63, 105]. The below section explains the hydrogen microprint technique experiment.

3.6.2.1. Hydrogen microprint theory

Hydrogen diffusion occurs in both hydrogen permeation and hydrogen microprint technique experiments. The HMT is used to visualize hydrogen diffusion path instead of measuring the diffused hydrogen as in the HP experiment. Hence, HMT experiments reveal the variations in the diffusion of hydrogen atoms with microstructural features in steels. HMT is performed on the theory that the diffused hydrogen atoms from the sample reduce the silver ions in an emulsion coating of silver bromide on the sample surface. The hydrogen diffusion path is indicated by the metallic silver, and it is observed under SEM after washing out the unreacted silver bromide using a fixing solution. The HMT experiment involves multiple stages, and Figure 3.10 explains the theory behind it. The thin square sample is polished on either side and is etched at one side to expose the microstructure. The details of the polishing and etching were explained earlier. Stage A of the figure represents the side view of the etched sample. The sample is further coated with a silver bromide emulsion on the etched side in stage B. The emulsion coated sample is electrochemically charged with hydrogen from the other side in step C [63]. The HMT experiment in this research uses a dedicated test setup for hydrogen charging. The generation of hydrogen from the electrochemical charging is expressed by equation 3.10 [96], as given by,

$$H^+ + e^- = H \qquad (3.10)$$

The hydrogen produced by the electrochemical reaction is allowed to diffuse through the sample. When the hydrogen finally reaches the emulsion coated side of the sample, it reduces the silver ions in the silver bromide emulsion to metallic silver at stage D, as expressed [76, 63, 95] in the equation 3.11 and 3.12, as given by,

$$Ag^+ + H = Ag + H^+ \quad (3.11)$$

$$2H^+ = H_2 \text{ and } \frac{1}{2}H_2 + Ag^+ = H^+ + Ag \quad (3.12)$$

After the predetermined time of charging and discharging of hydrogen through the sample, the remaining unreacted emulsion coating is washed away using a fixing solution. Stage E of the HMT shows the same. The metallic silver that remains on the surface after fixing shows the sites from which hydrogen diffuses. The metallic silver is visible as white spherical particles superimposed on the microstructure when examined under an SEM [76]. The number of silver particles found on the surface of the sample resembles the actual amount of hydrogen released from the specimen surface [95].

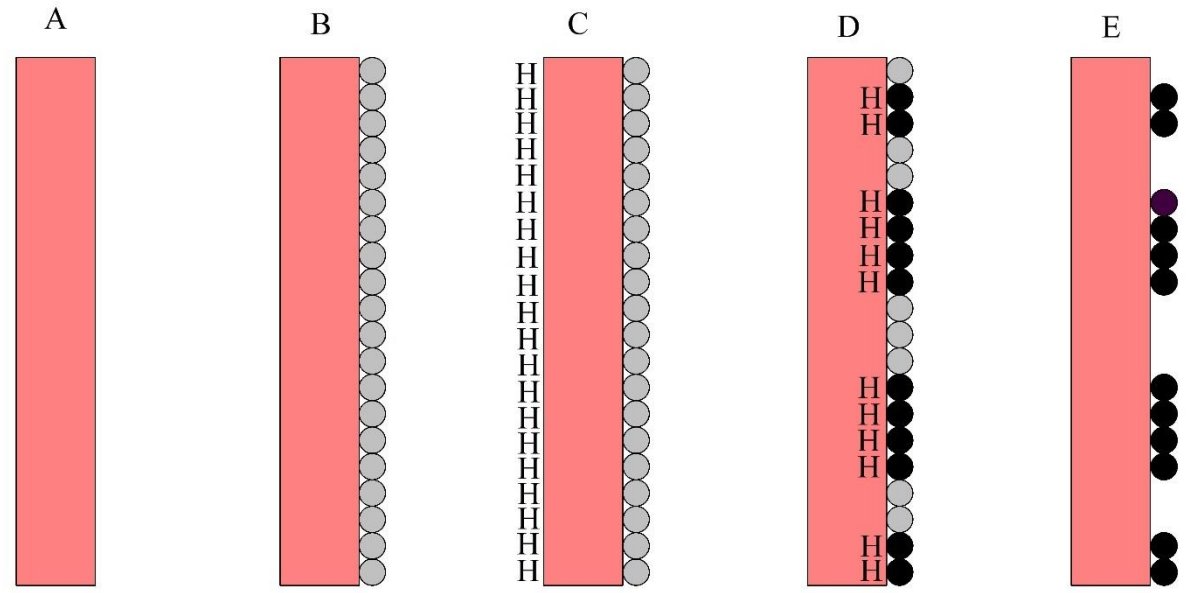

Figure 3.10. Stages of hydrogen microprint technique.

3.6.2.2. Hydrogen microprint cell assembly

As mentioned in theory, the HMT experiment involves multiple stages. The two stages of the HMT experiments use this cell assembly. The electrochemical hydrogen charging on an emulsion coated sample and the corresponding reaction between diffused hydrogen and emulsion occurs in the test setup. Figure 3.11 shows the schematic diagram of the HMT cell assembly for hydrogen charging, and it is the duplication of the test setup made by Luu et al.

[63]. The main part of the test setup is a specially designed glass beaker with a small flange at the bottom of the glass cup. The role of the glass cup is to become the container for carrying the charging cell electrolyte. The required hydrogen for diffusion is produced inside the charging cell beaker. The electrolyte for the charging cell is 250 ml mixture of 0.1 M sulfuric acid (H_2SO_4). The development of hydrogen molecule delays the ability of the atomic hydrogen to diffuse through the material. Hence, the formation of the hydrogen molecule is retarded by the addition of 3 grams per liter of ammonium thiocyanate that acts as a recombination poison for hydrogen molecule. The charging cell is covered with a teflon lid, and it has a fixed position for the counter electrode to maintain the uniformity of cell geometry in all experiments. The charging cell uses a graphite cylinder electrode of 5 mm diameter as the counter electrode, and it extends into the charging cell electrolyte. During the entire testing, there is an inert argon gas supply into the charging cell to deaerate the system from oxygen. The closing lid has two fixed plastic connectors for the argon gas in and out. The argon gas intake connector is placed away from the sample and extended into the electrolyte in the glass beaker.

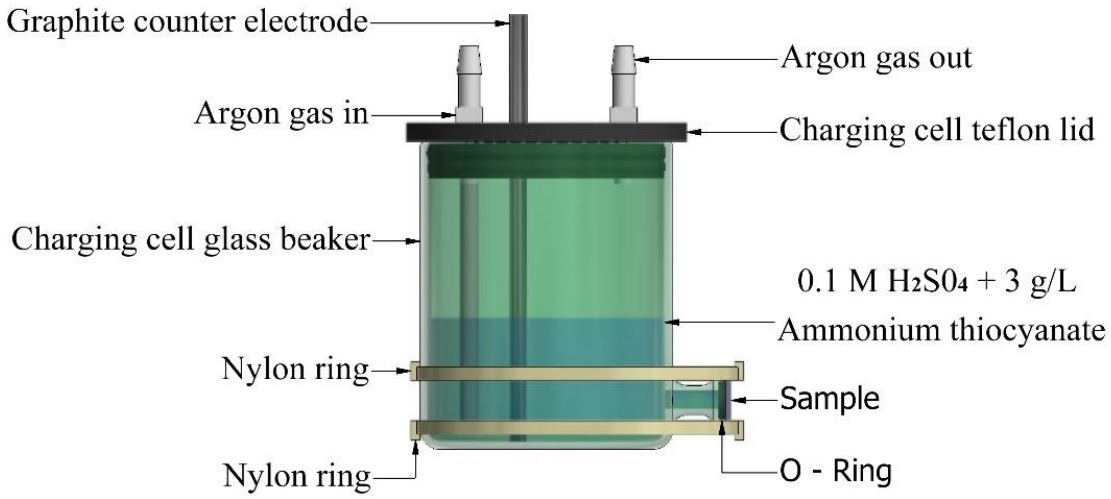

Figure 3.11. Schematic diagram of hydrogen microprint cell assembly.

The thin square sample is polished on either side, and there is a uniform emulsion coating on one side of the sample. The sample is placed at the end of the glass beaker flange with the emulsion coated side away from the flange. Two nylon rings keep the sample firmly, and a rubber O-Ring was held between the sample and flange to avoid any electrolyte leakage through the flange. The design of flange and O-Ring produces a circular area exposing of 1 square centimeter between sample and electrolyte. Figure 3.12 shows the dimensions of the HMT sample assembled with an O-Ring. The graphite counter electrode, electrolyte and emulsion coated sample that act as the working electrode forms the electrochemical cell.

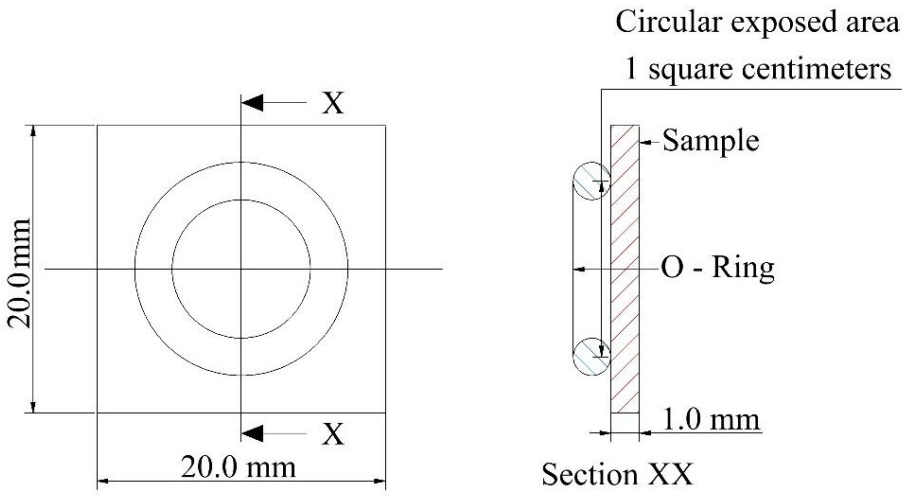

Figure 3.12. Dimensions of HMT sample assembled with O – Ring.

3.6.2.3. Test procedure for the hydrogen microprint technique

The entire HMT testing does not require any darkroom as used for autoradiography [104]. It is performed in normal illumination. The previously polished thin square sample is initially etched at one side to reveal the microstructure and further taken for emulsion coating [63]. The details of the polishing and etching were explained earlier. The required emulsion is prepared by mixing the Alfa Aesar, MFCD00003398 model, 5 grams of Silver bromide (AgBr) powder in 10 ml of 1.4 M sodium nitrite ($NaNO_2$) solution [76, 104]. Sodium nitrite is used instead of distilled water to avoid the corrosion of the etched sample. A monogranular AgBr emulsion layer is obtained on the etched face of the sample using a 5 cm diameter wire loop, made from a 1 mm thin metal wire [104]. The emulsion layer on the surface of the sample takes 15 minutes for desiccating. The HMT cell is assembled with a dried emulsion coating for the next stage of the experiment. The HMT cell assembly, explained in the previous section, is connected to the power source, as shown in Figure 3.13. This stage of the experiment in the HMT test setup includes an electrochemical hydrogen charging and the instant reaction of AgBr crystals of the emulsion coating by diffused hydrogen. The charging cell is connected to the Instek direct current power supply to deliver 5 mA constant current that produces the hydrogen for diffusion. The positive anode and negative cathode of the power supply are connected to the graphite counter electrode and the working sample. After making appropriate connections, the electrochemical cell is activated by pouring the electrolyte into the charging cell.

When the charging cell produces the hydrogen, it is immediately diffused from the charging side of the sample. The diffused hydrogen escapes from the emulsion-coated side of the sample

by reducing the silver ions in the emulsion to metallic silver. The hydrogen charging is terminated in the sample once the predetermined charging time elapses. The sample remains in the test setup for the same time used for charging. Hence, the sample undergoes one hour of cathodic hydrogen charging with the power supply and one hour of discharging after turning off the power supply. The hydrogen flux from the metal is reacted with emulsion for two hours in all samples, and the silver ions in the hydrogen diffusion path are reduced to metallic silver during this time [104]. The extended time allows the immediate discharging of all hydrogen atoms from the reversible traps. Later, the sample is dismantled from the cell assembly without disturbing the emulsion coating for proceeding to the next stage of the HMT experiment.

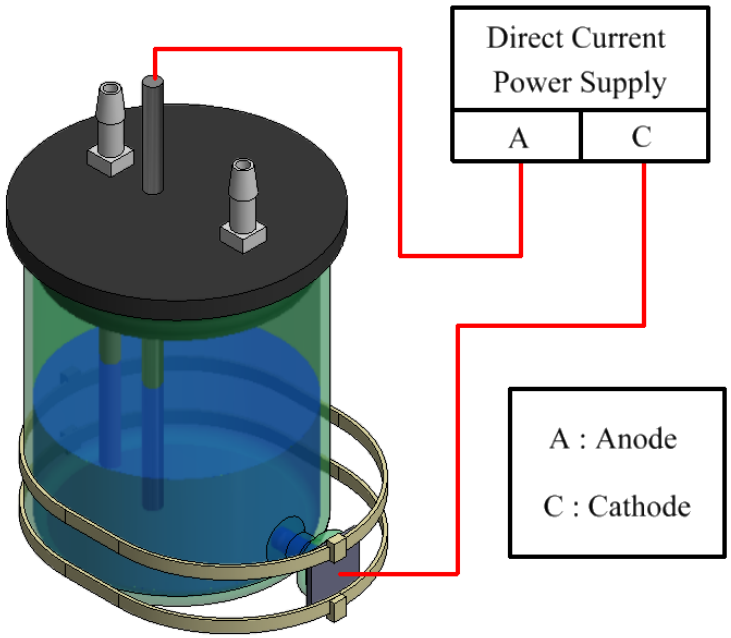

Figure 3.13. Schematic diagram of the hydrogen microprint test set up.

After the hydrogen diffusion and simultaneous reduction of silver ions, the emulsion coated side of the sample is dipped in a fixing solution made at room temperature. The fixing solution is prepared by mixing 0.6 M sodium thiosulfate ($Na_2S_2O_3$) in 1.4 M sodium nitrite ($NaNO_2$) solution. The sample is initially dipped in the fixing solution for 1 minute to wash away all the AgBr crystals that are not reduced by the diffused hydrogen. Later, the sample is cleaned by dipping in distilled water for 30 seconds and dehydrated using a blow dryer. Adequate care is taken for not disturbing the reduced metallic silver in the emulsion coated side during fixing, rinsing, and drying. Later, the sample is examined under an SEM to visualize the superimposed white spherical silver particles that indicate the hydrogen diffusion path.

CHAPTER 4

RESULTS AND DISCUSSION

4.1. Overview

Chapter four contains results of the study on the effect of grain size and misorientation on hydrogen diffusion and accumulation. Initially, prepared samples are evaluated by the characterization techniques like OM, SEM, EDS and EBSD. It allows in understanding microstructure, evaluating grain size, identifying elemental composition and calculating misorientation in the samples. Finally, results from hydrogen permeation experiments are related to the observations from hydrogen microprint technique experiments.

4.2. Estimation of the grain sizes from the annealed samples

The grain sizes of the annealed samples were estimated before hydrogen permeation and hydrogen microprint technique experiments on these samples. Grain sizes of samples were measured using the Heyn's technique. The need for understanding the effect of pre-cold rolling on grain growth during annealing was concluded from the literature review. Hence, pre-cold rolled samples were annealed initially to clarify whether the samples for the HP and HMT experiments should be prepared by annealing the as-received or cold-rolled steel.

4.2.1. Effect of pre-cold rolling before annealing

In this section, the impact of pre-cold rolling for grain growth during annealing is studied in X70-1 pipeline steel. Initially, a rectangular strip of 80 x 20 x13 mm was made from the top layer of the X70-1 plate using a vertical band saw. The strip was cold-rolled (CR) to make five rectangular samples of 20 x 10 mm size in as-received (AR), 10 % CR, 20 % CR, 30 % CR, and 40 % CR conditions. The five samples were annealed together in a muffle furnace. The annealing begins from room temperature to a reheating temperature of 1000º C, and samples were kept at that temperature for a soaking time of 50 hours. The samples were finally cooled to room temperature within the furnace. The reheating temperature and soaking time were chosen based on some initial thermomechanical treatments, and results from those experiments were not discussed in this thesis. The annealed samples were polished to the required surface finish, as explained earlier. EBSD characterization was used to determine the grain sizes of polished samples in this section. The measured grain sizes in annealed samples are plotted against the degree of pre-cold rolling in Figure 4.1. The largest grain size of 34.4 microns is measured for an annealed sample without any pre-cold rolling. The lowest average grain size

of 18.3 microns is measured for an annealed sample with a pre-cold rolling of 40 %. The grain size of the annealed sample decreased with the degree of pre-cold rolling before annealing. Hence, it is decided to do the annealing on the as-received steel without any pre-cold rolling to obtain larger grain sizes. However, the annealing cycles can be optimized based on the required range of grain sizes for the experiment.

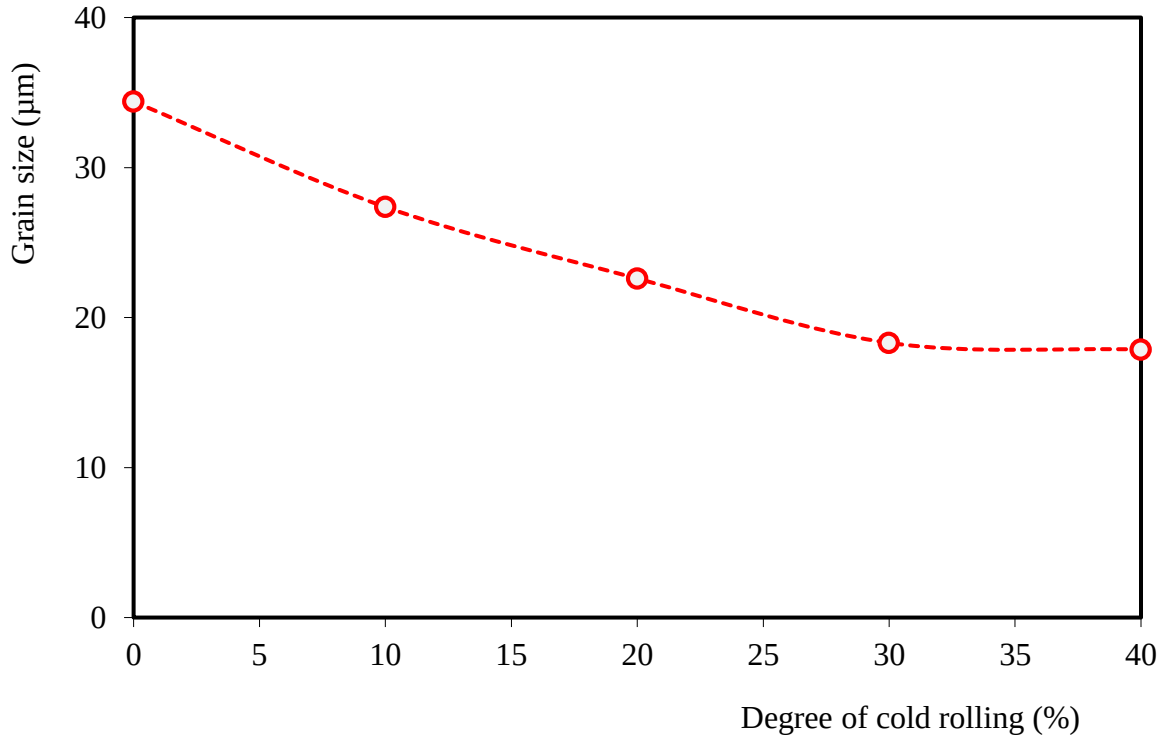

Figure 4.1. Degree of pre-cold rolling versus grain size in annealed X70-1 steel at 1000 ° C.

There is some difference in the definition of grains in the EBSD method than the conventional metallographic methods. In EBSD, the grains are well-defined based on orientation differences [106]. If the orientation of successive points is within a predefined value, then it is considered as a single grain. [107]. The EBSD maps consider grain size as the area obtained by adding the total occurrence of points in grain with the product of the square of the step size and a scanning grid factor [108]. All the EBSD scans presented in this section were obtained with a step size of 1.5 microns. Figure 4.2 presents the crystal orientation maps of the various annealed samples from the post-processed data of the EBSD characterizations. The orientation maps clearly illustrated the increase in grain size after annealing the pre-cold rolled X70-1 plate. The grains are showing random orientations based on the color code provided with the figure. However, the 40 % pre-cold sample after annealing has a more specific direction. The as-received X70-1 plate was annealed as the objective of the research needs a wide range of grain sizes.

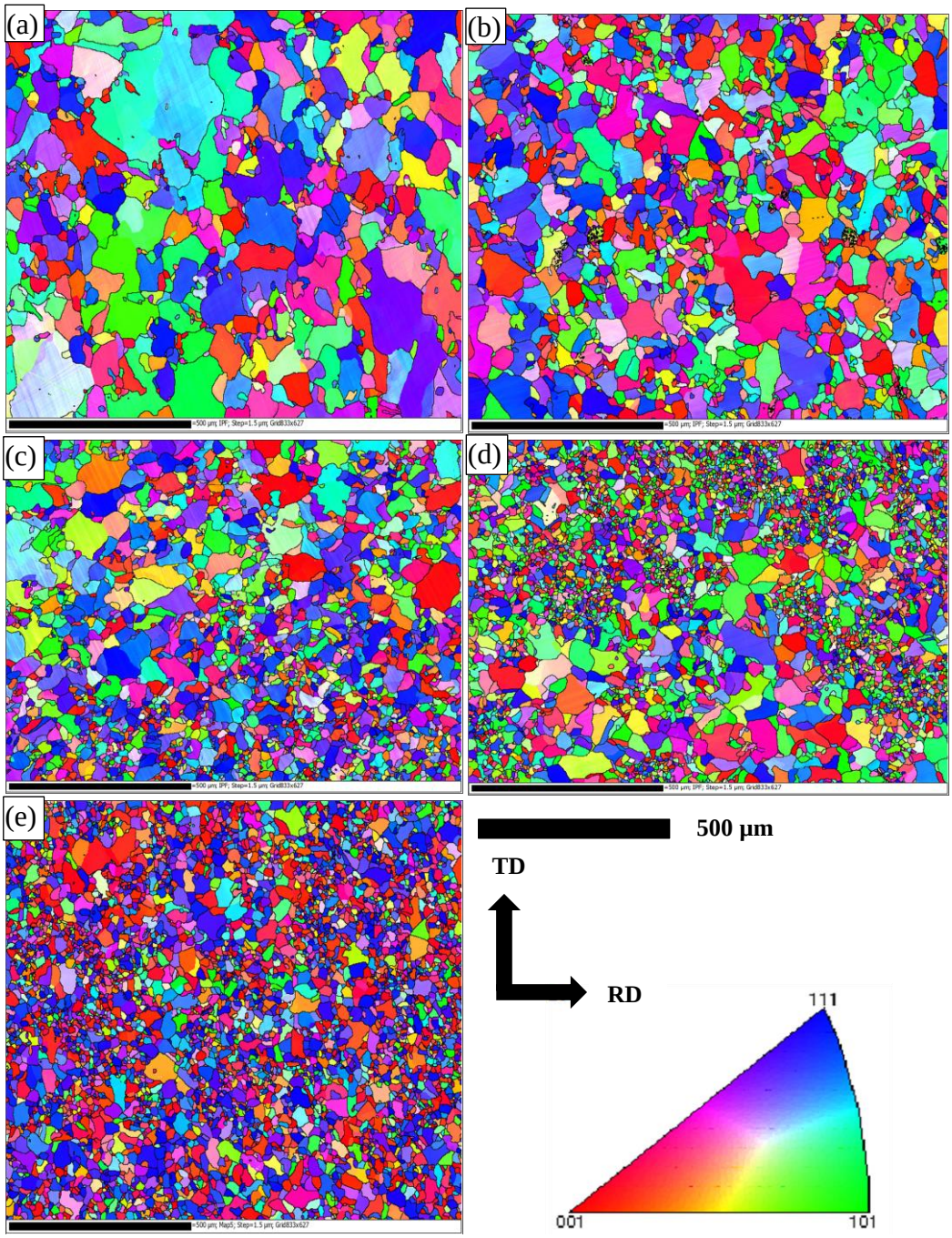

Figure 4.2. Crystal orientation maps in annealed X70-1 steel: (a) AR, (b) 10 % CR, (c) 20% CR, (d) 30% CR and (e) 40 % CR.

4.2.2. Effect of annealing in as-received samples

Figure 3.2 shows the annealing program used to prepare samples with a wide range of grain sizes by annealing the as-received X70-1 steel. Table 3.2 provides the details of the as-received two samples and eight annealed samples prepared from either layer. The samples were polished and etched based on the previously explained procedures. Later, the etched samples were

characterized by OM or SEM. Figure 4.3 shows the OM and SEM images of sample T1 and M1 from either layer of as-received X70-1 steel. The microstructural observation shows that both layers looks identical and composed of acicular ferrite (AF), and some polygonal ferrite (PF), quasi polygonal ferrite (QF) and Bainite (B). The microstructural phases are marked in the figure and agreeable with the literature [109, 110]. The average measured grain size of the top-layer was 2.30 ± 0.07 microns, and that of the mid-layer was 2.66 ± 0.10 microns. This marginal grain size increase in the mid-layer is due to an increased amount of bainite grains in mid-layer. There is elemental segregation of carbon around the center segregation zone [48]. Bohemen et al. reported that bainite transformation is prominent from an austenitic matrix of steel with increased carbon content [111]. Thus, the increase of bainite grains in the mid-layer than the top-layer can be related to the favorable elemental segregation for bainite transformation in the mid-layer. The increased amount of larger bainite (B) grains in mid-layer is easily distinguishable from SEM images. Remarkably, the SEM images identified many single inclusions in mid-layer, and the latter part of this chapter explains it with the help of EDS analysis.

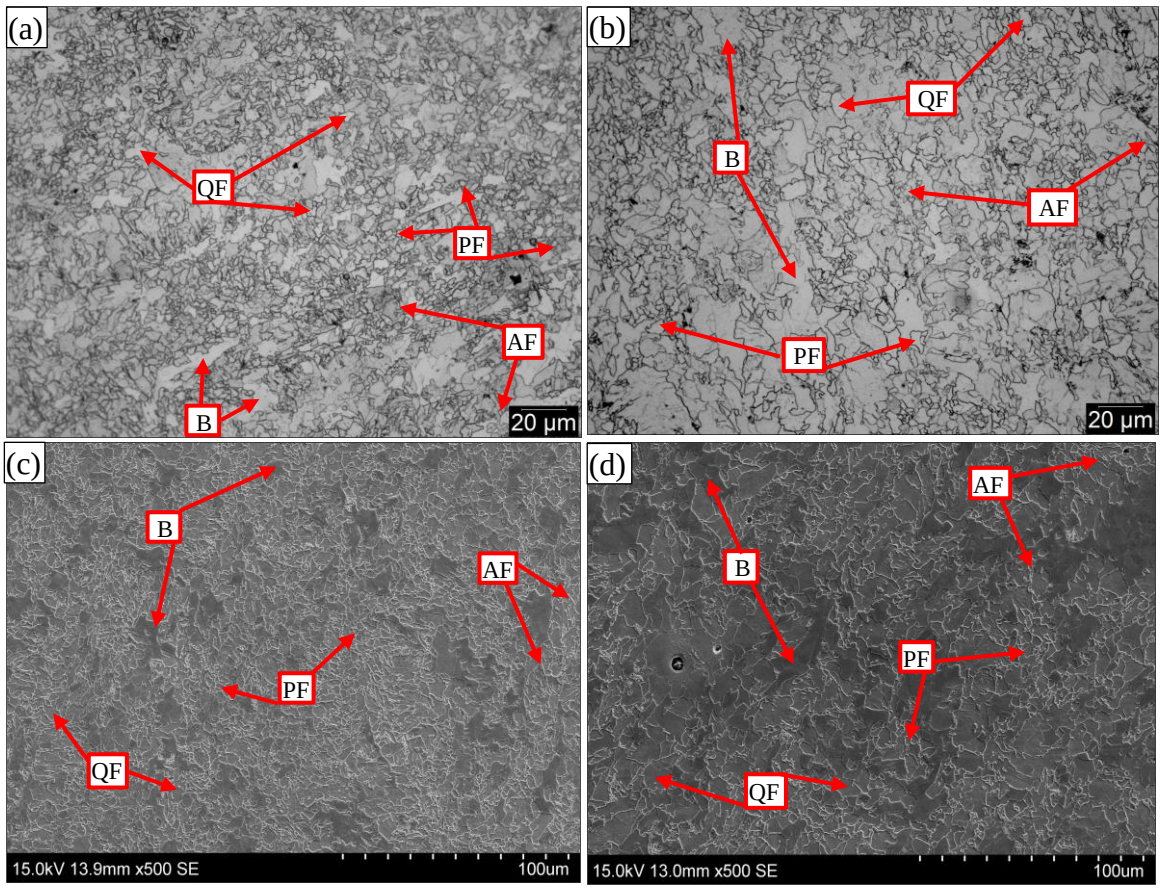

Figure 4.3. Microstructural images of the as-received X70-1 steel: (a) OM of top-layer, T1 (b) OM of mid-layer, M1 (c) SEM of top-layer, T1 and (d) SEM of mid-layer, M1

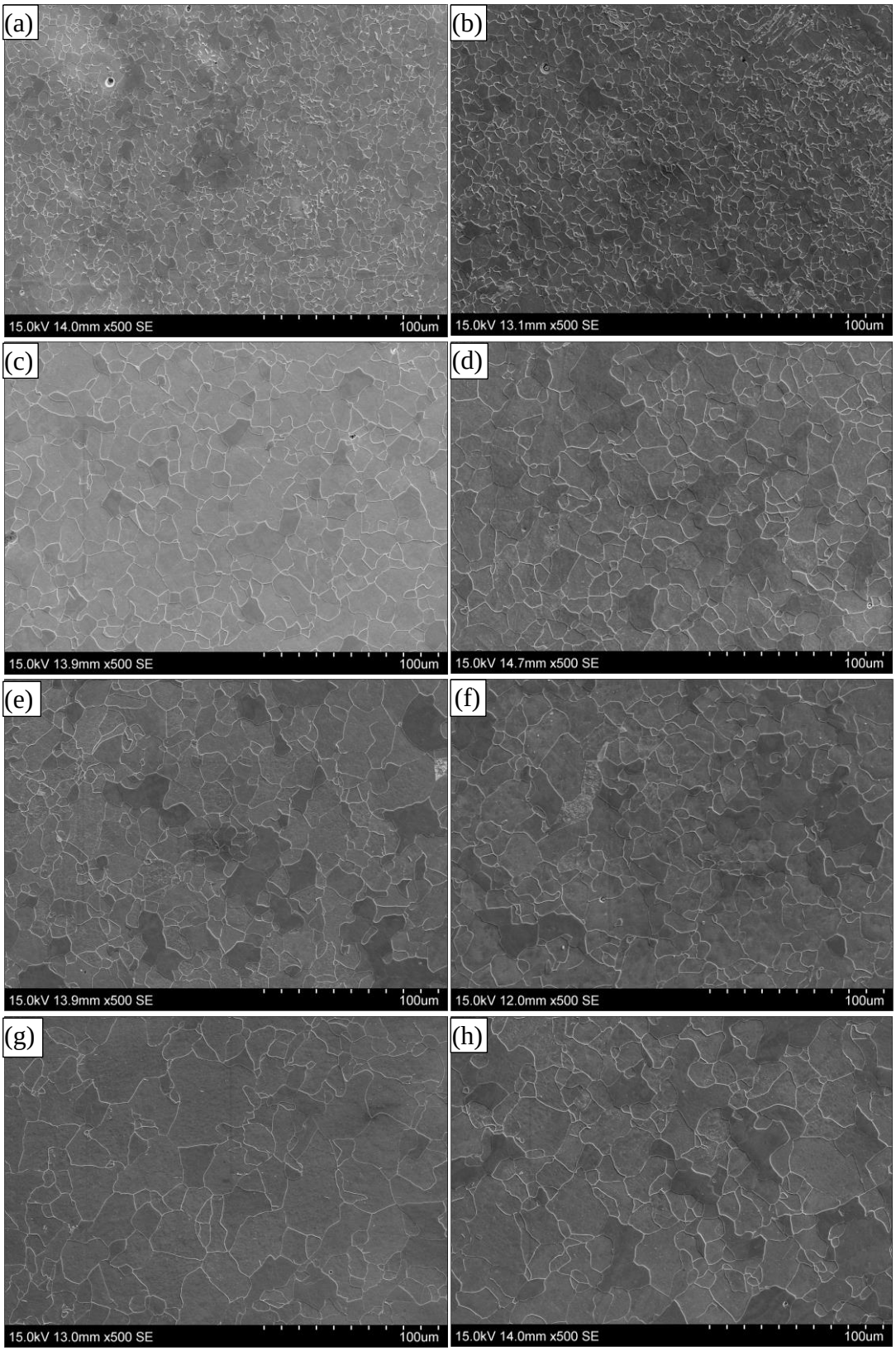

Figure 4.4. SEM images of the microstructure in annealed X70-1 steel: (a) T2, (b) M2, (c) T3, (d) M3, (e) T4, (f) M4, (g) T5 and (h) M5.

Figure 4.4 shows the SEM images of annealed samples from the top layer (T2 to T5) and the

mid-layer (M2 to M5). The visual observation of those micrograph concluded the increase in grain growth from T2 to T5 in the top layer and M2 to M5 in the middle layer. Thus, the designed annealing program allowed an increasing trend in the grain size from as-received condition (T1 or M1) to the final annealing cycle, A4 in either layer (T5 or M5). The micrograph corresponding to each of the individual annealing cycles shows that the analogous mid-layer has a higher number of larger bainite grains than the top layer. Also, the micrographs show that polygonal ferrite is dominant than the acicular ferrite when annealing cycles change from A1 to A4. There are separate and interconnected degenerate pearlite (DP) colonies in all samples. The influence of DP in hydrogen diffusion will be explained with observations from the HMT experiment in the last part of this chapter.

Table 4.1. Measured grain size in annealed X70-1 steel.

Cases	[1]Average grain size in the top-layer steel (μm)	[2]Average grain size in the mid-layer steel (μm)	[3]Average grain size for each case (μm)	Approximate average grain size for each case (μm)
As-received	2.30 ± 0.07	2.66 ± 0.10	2.48 ± 0.09	2.5
A1 at 875 º C	3.46 ± 0.04	3.54 ± 0.09	3.50 ± 0.05	3.5
A2 at 1000 º C	8.49 ± 0.19	8.55 ± 0.14	8.52 ± 0.11	8.5
A3 at 1050 º C	10.16 ± 0.47	10.13 ± 0.31	10.15 ± 0.26	10
A4 at 1150 º C	11.84 ± 0.90	11.99 ± 0.63	11.92 ± 0.51	12

Table 4.1 provides the measured average grain size of ten samples from either layer. The combined grain size from either layer is reported as an average grain size for each case. There is an elemental segregation of manganese and carbon around the center segregation zone [48, 112, 113]. Bohemen et al. reported that the bainite transformation is prominent from an austenitic matrix of steel with increased carbon content [111]. Remarkably, Feng et al. revealed that the carbon-manganese segregation alters the bainite transformation curve of the time-temperature-transformation diagram and the iron-manganese-carbon atomic segregation zone

[1] The measured average grain size in top-layer of the steel was based on four measurements.
[2] The measured average grain size in mid-layer of the steel was based on four measurements.
[3] The measured average grain size for each case was based on eight measurements with four measurements from each layer.

retard the atomic motion [114]. Those conditions allowed the required thermodynamics for the bainite transformation. The elemental segregation and favorable conditions for bainite transformation can increase the number of bainite grains in the mid-layer than the top-layer. Figure 4.5 plots the change in approximate average grain size with the reheating temperature of the different annealing cycles. The trend of grain growth with an increase in reheating temperature agreed with the literature [69]. The thermally treated samples and the as-received samples made samples with five different grain sizes each from the top layer and mid-layer. The smallest grain size is 2.5 microns, and the largest grain size is 12 microns. All the ten samples were used in the hydrogen permeation experiment, whereas selected samples based on the hydrogen permeation results were used in the hydrogen microprint experiment.

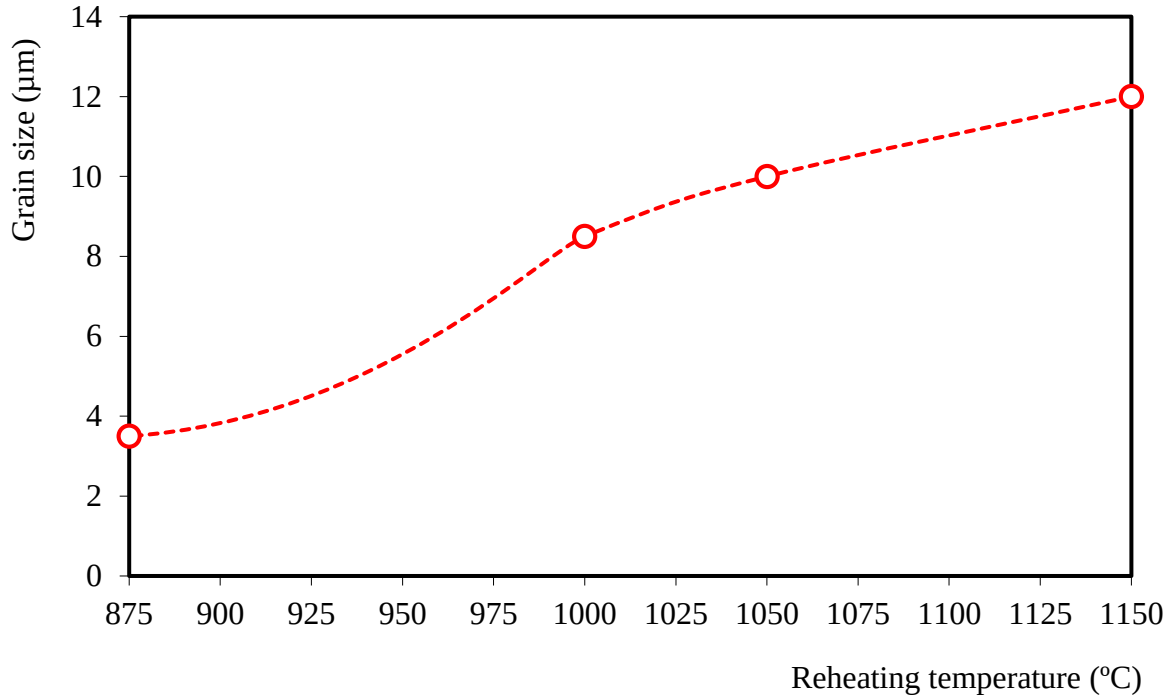

Figure 4.5. Effect of 5 minutes of reheating temperature on average grain size in X70-1 steel.

4.3. Evaluation of kernel average misorientation after different cold rolling reduction

There were five samples with different misorientations to study the effect of misorientation on hydrogen diffusion and accumulation in X70-2 steel. The variable plastic strain of the samples was estimated before proceeding with HP and HMT experiments. The regional plastic strain represented by the local grain misorientation is measured by kernel average misorientation (KAM) from the EBSD analysis. During EBSD characterization, the average misorientation around a measurement point for a predefined set of neighboring points is quantified using KAM. The calculation of KAM considers the adjacent pixels with a misorientation angle lower than a threshold angle of 5°. It allows the calculation of KAM without the grain boundaries.

Table 3.3 shows the details of the prepared samples for this study. Figure 4.6 shows the OM and SEM images of as-received X70-2 steel from the top-layer. The microstructure is composed of a mixture of polygonal ferrite (PF), quasi polygonal ferrite (QF), bainite (B) and some acicular ferrite (AF). The identified constituent phases are marked in the images and agreed with the previous studies using pipeline steels [109, 110]. Also, the average grain size of the sample was measured as 6.7 microns using the mean lineal intercept technique.

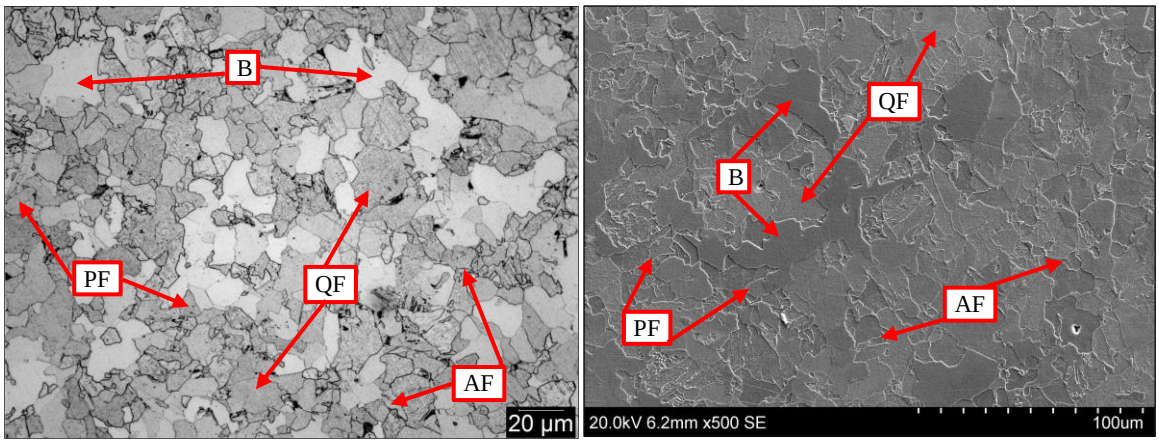

Figure 4.6. Microstructure of as-received X70-2 steel: (a) OM image and (b) SEM image.

Figure 4.7 and Figure 4.8 shows the grain boundary and KAM maps of samples from the EBSD analysis. The sample surface that contains the rolling direction (RD) and transverse direction (TD) were characterized. The grain boundary maps show that the cold-rolling deformed the grains and elongates it in the rolling direction. Also, the intensity of grain elongation increased with the increase in the degree of cold rolling from samples A to E. The analysis of sample A with the color scale shows that KAM was mostly less than 1º, and some isolated regions show a KAM between 1º and 2º. However, more than 50 % of the KAM in sample B appeared as a value close to 2º, and it is an indication of the induced plastic strain in the sample. The blue color representing a KAM close to 0º decreased from sample B to E. However, the green, yellow and red color corresponding to a KAM of 2º, 3.5º and 4.5º are increased from sample B to E. This observation of color transition indicated a higher occurrence of larger KAM angles for highly deformed samples. The EBSD indexing is challenging for the samples with a large amount of deformation. Hence, there are many elongated non-indexed areas in the rolling direction representing the highly deformed and elongated grains in sample E. The KAM maps show that the cold rolling induced variable misorientations in different regions of the samples. As the KAM is increased with an increased degree of cold rolling, the highly deformed samples are represented by the larger KAM angle. Figure 4.9 shows the absolute occurrence of the larger KAM angles from 3º to the threshold angle of 5º. The absolute occurrence of each KAM

angle is increased from samples A to E. Also, the absolute occurrence of the KAM angle in each sample is decreased from 3º to 5º. Remarkably, the as-received sample does not have any larger misorientations. The observations from the graph allowed to confirm that sample A and sample E are the least and most deformed samples.

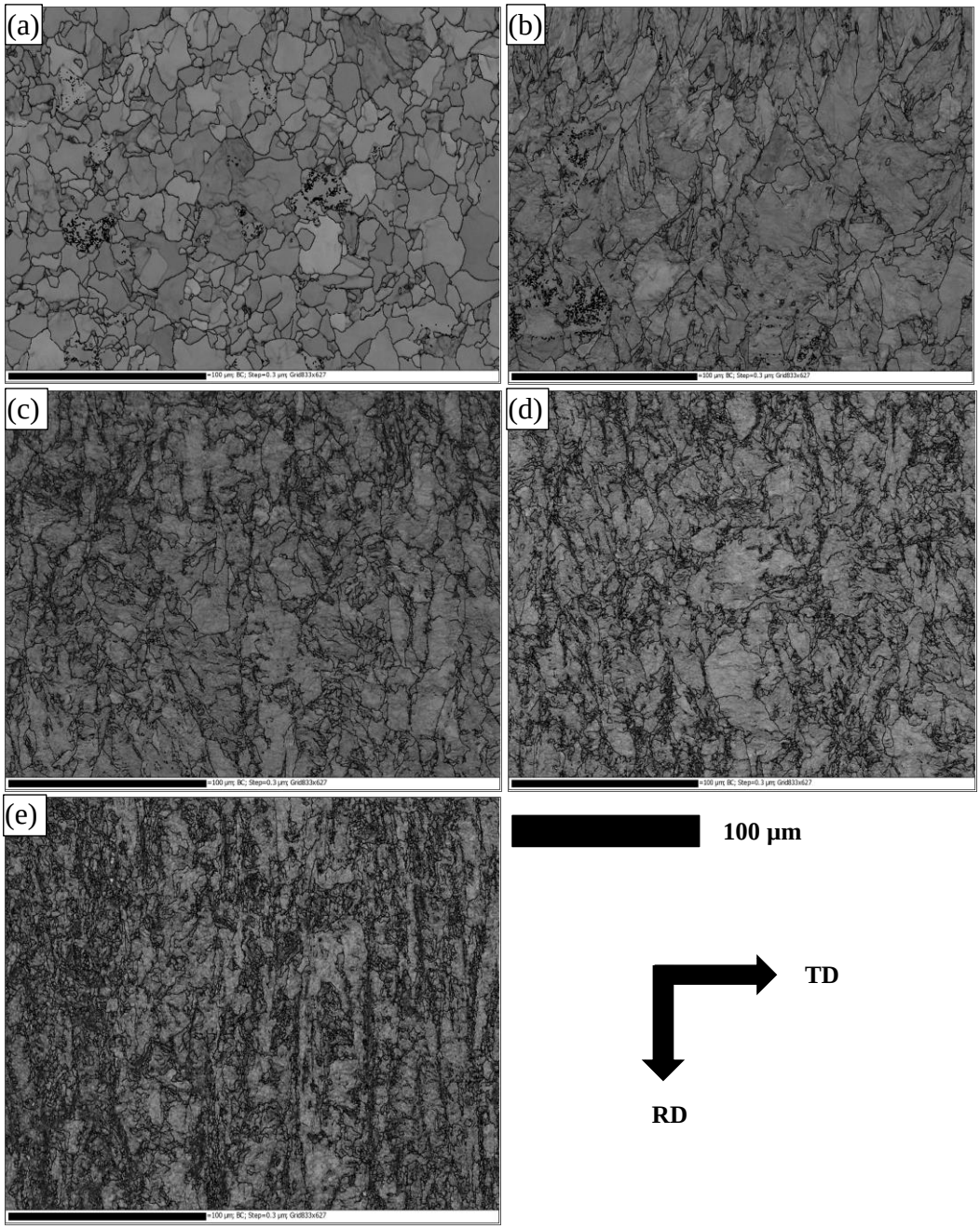

Figure 4.7. Grain boundary maps in X70-2 steel: (a) sample A, (b) sample B, (c) sample C, (d) sample D and (e) sample E.

Even though the degree of cold rolling was increased by 20 % for each sample, the induced misorientations are not proportional to the degree of cold rolling. It occurred by the multiple

passes in cold rolling, variations in the intensity of deformation in tested thickness and the non-indexing of the EBSD scan in the highly deformed samples. The non-proportionality in the measured misorientations enforced to estimate the mean KAM. It is represented as the mean of the product of KAM and absolute occurrence.

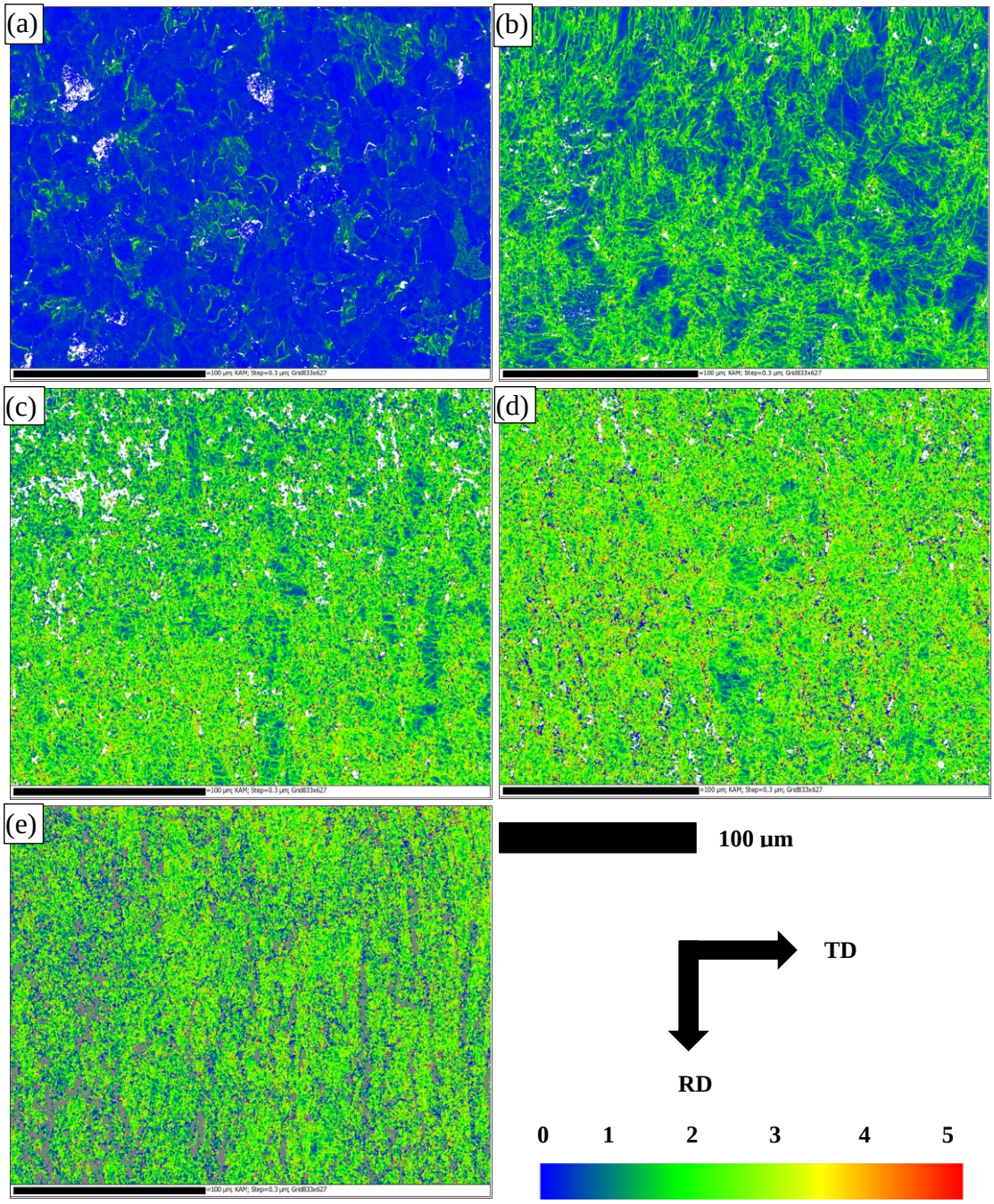

Figure 4.8. Kernel average misorientation maps in X70-2 steel: (a) sample A, (b) sample B, (c) sample C, (d) sample D and (e) sample E.

Table 4.2 shows the mean KAM and the corresponding increase in mean KAM from the

penultimate degree of cold rolling. Figure 4.10 demonstrated the non-proportionality of misorientations with the degree of cold rolling as the graph is deviating from a straight line. The graph also established that the corresponding increase in mean KAM with an increase in the degree of cold rolling is decreased.

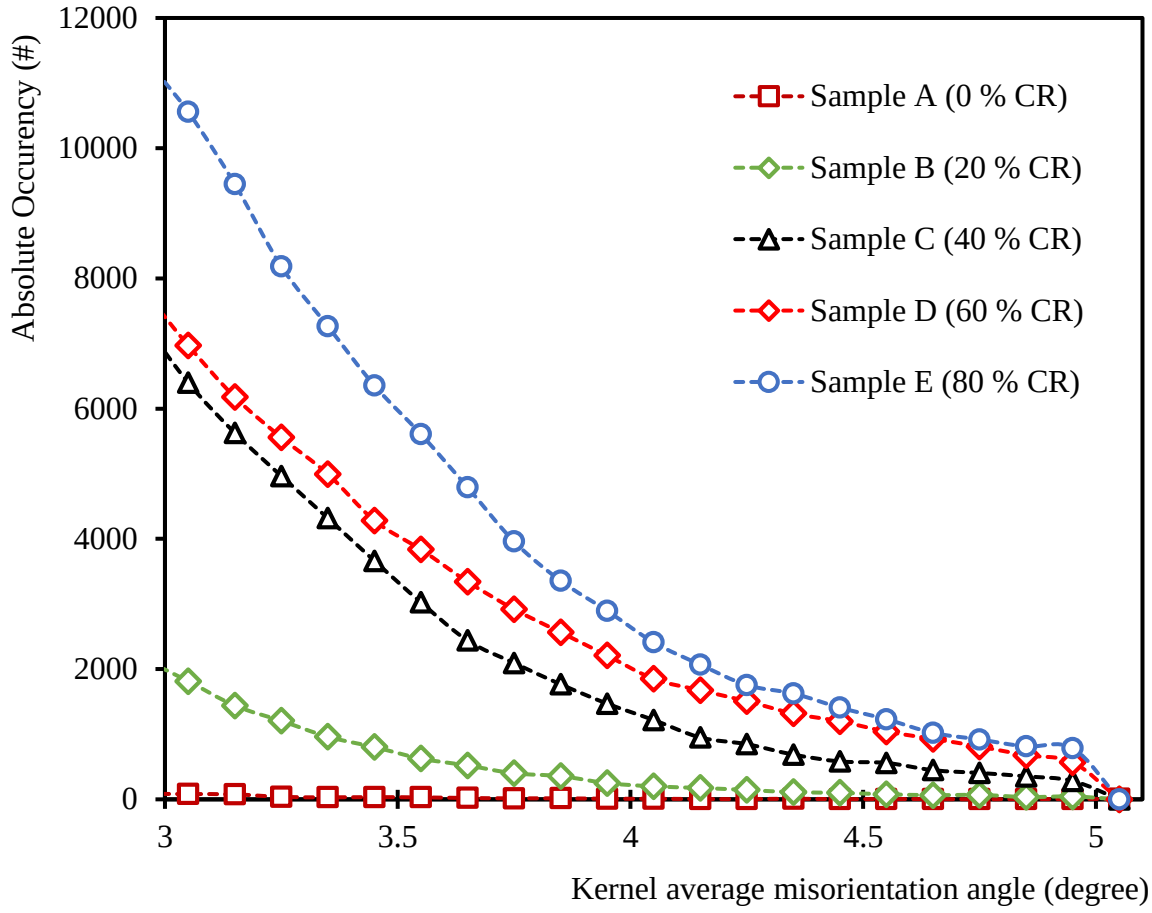

Figure 4.9. KAM angle versus absolute occurency at the RD-TD plane in X70-2 steel.

Table 4.2. Mean KAM for the cold-rolled X70-2 steel.

Sample name	Degree of cold rolling (%)	Mean KAM (degree)	Increase in mean KAM (degree)	Increase in mean KAM (%)
A	0	0.33	-	-
B	20	1.14	0.82	249
C	40	1.71	0.56	49
D	60	1.87	0.16	9
E	80	1.98	0.11	6

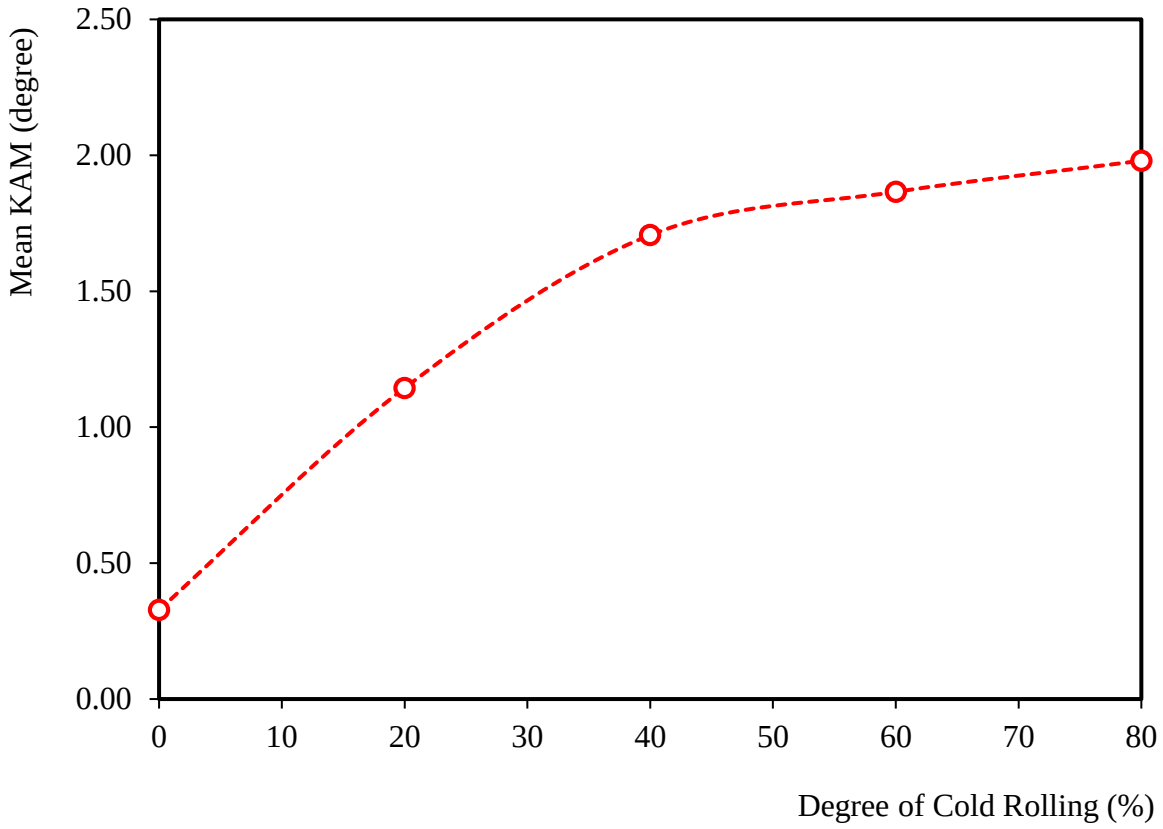

Figure 4.10. Effect of cold rolling on mean KAM in X70-2 steel.

4.4. Role of grain size in hydrogen trapping by permeation

The ten samples were repolished to the final dimension for the HP experiment and coated with a thin layer of palladium on either side after the grain size evaluation. All samples were tested by the dual-polarized HP experiment, and the oxidized current representing the permeated hydrogen was instantaneously recorded using the Gamry software. The permeability, effective diffusion coefficient, apparent solubility, and trapping sites were calculated based on the steady-state current and time lag from the permeation curve. All samples were tested by the HP experiment at a standard room temperature of 23 ° C and a standard atmospheric pressure of 1 atm. Table 4.3 and Table 4.4 provides the calculated permeation parameters of ten samples from the first and second polarization. Figure 4.11 shows the effect of grain growth on diffusion parameters after the dual-polarized HP experiment. The permeability is increased with grain growth for both polarizations in either layer. The increased permeability should be related to the decreased number of triple junctions and grain boundary surface area per unit volume for larger grains. The triple junction and grain boundaries should act as trapping sites for hydrogen and reduce hydrogen mobility through steel for small grain sizes. Hence, the trapping sites are decreased with grain growth for both layers of steel.

Table 4.3. Permeation parameters in annealed X70-1 steel from the first polarization.

Average grain size, Sample (µm)	Steady current, I_∞ ± 2.73 % (µA)	Time lag, T_L ± 12.29 % (s)	Permeability, $J_\infty L \times 10^{-11}$ ± 2.73 % (mol. $cm^{-1}.s^{-1}$)	Diffusion coefficient, $D_{eff} \times 10^{-8}$ ± 12.29 % ($cm^2.s^{-1}$)	Apparent solubility, $C_{app} \times 10^{-6}$ ± 12.59 % (mol. cm^{-3})	Trapping sites, $N_t \times 10^{18}$ ± 17.59 % (cm^{-3})
T1 (2.5)	70.43	3580	7.30	46.55	156.78	8621.94
T2 (3.5)	71.73	1304	7.43	127.81	58.16	1157.53
T3 (8.5)	88.30	290	9.15	574.71	15.92	67.99
T4 (10)	117.95	206	12.22	809.06	15.11	44.95
T5 (12)	144.63	150	14.99	1111.11	13.49	28.49
M1 (2.5)	70.38	2378	7.29	70.09	104.06	3794.21
M2 (3.5)	77.15	14328	7.99	11.63	687.30	151680.53
M3 (8.5)	85.70	21900	8.88	7.61	1167.07	393797.73
M4 (10)	100.80	8832	10.45	18.87	553.55	75260.00
M5 (12)	147.17	484	15.25	344.35	44.29	321.57

Table 4.4. Permeation parameters in annealed X70-1 steel from the second polarization.

Average grain size, Sample (µm)	Steady current, I_∞ ± 2.73 % (µA)	Time lag, T_L ± 12.29 % (s)	Permeability, $J_\infty L \times 10^{-11}$ ± 2.73 % (mol. $cm^{-1}.s^{-1}$)	Diffusion coefficient, $D_{eff} \times 10^{-8}$ ± 12.29 % ($cm^2.s^{-1}$)	Apparent solubility, $C_{app} \times 10^{-6}$ ± 12.59 % (mol. cm^{-3})	Trapping sites, $N_t \times 10^{18}$ ± 17.59 % (cm^{-3})
T1 (2.5)	39.46	4208	4.09	39.61	103.25	6672.10
T2 (3.5)	66.09	1292	6.85	129.00	53.09	1046.82
T3 (8.5)	74.05	160	7.67	1041.67	7.37	16.69
T4 (10)	82.80	94	8.58	1773.05	4.84	6.04
T5 (12)	130.93	60	13.57	2777.78	4.88	3.54
M1 (2.5)	65.76	406	6.81	410.51	16.60	100.58
M2 (3.5)	72.96	260	7.56	641.03	11.79	44.91
M3 (8.5)	78.65	114	8.15	1461.99	5.57	8.68
M4 (10)	79.72	100	8.26	1666.67	4.96	6.65
M5 (12)	140.28	50	14.54	3333.33	4.36	2.49

The tabulated values show that the measured steady-state current and permeability for second polarization is less than the first polarization for both layers. The lower permeability in the second polarization is due to the saturation of irreversible traps by hydrogen after the first polarization. This trap saturation reduced the steel porosity for the second polarization. So, the distance traveled by the hydrogen atoms through the steel in second polarization is increased to cause a reduction in the permeability. The permeability in the mid-layer is slightly higher than the top layer for most grains in either polarization. This observation should be related to the marginal increase in the mid-layer grains that reduced the trapping by triple junctions and grain boundaries.

The trend for the measured time lag is inversely reflected when the effective diffusion coefficient is plotted against the grain size, as shown in Figure 4.11. The reduced trapping by triple junctions and grain boundaries for larger grains increased the hydrogen mobility. Hence, the effective diffusion coefficient in either layer increased with grain growth for both polarizations. Contradictorily, there is an initial decay and subsequent growth in the effective diffusion coefficient of the mid-layer in first polarization. It may be due to the irreversible trapping sites of the samples from the center segregation zone. The initial decay and subsequent growth of measured irreversible trapping sites of the mid-layer verified the same. The effective diffusion coefficient in the second polarization is higher than the first polarization for either layer due to the saturation of irreversible trapping sites. Therefore, the average cross-sectional area for hydrogen diffusion in the second polarization increased to raise the effective diffusion coefficient closer to the bulk diffusion coefficient. The effective diffusion coefficient in the mid-layer is marginally higher than the top-layer for second polarization, and it is related to the marginal increase in the mid-layer grains that reduces the trapping by triple junctions and grain boundaries. The measured permeability and effective diffusion coefficient show a marginal increase in mid-layer for the second polarization. It allows in concluding that the mid-layer is slightly dominant over the top layer for hydrogen diffusion.

The plot of apparent solubility against grain size is also shown in Figure 4.11. The apparent solubility is decreased in larger grains as the trapping by triple junctions and grain boundaries is reduced with the increase in grain size. The explanation agrees with the literature that trapping at nodes and triple junctions reduced the movement of hydrogen and enhanced the hydrogen solubility [62]. Conflictingly, there is an initial growth and subsequent decay of apparent solubility in the mid-layer for first polarization. It occurs by the trapping of

irreversible sites. The irreversible trapping sites are saturated after first polarization, and the trapping of hydrogen by the active reversible traps during the second polarization is the reason for lower apparent solubility for the second polarization in either layer. The apparent solubility in the mid-layer is slightly lower than the top layer for second polarization. It can be related to the marginal increase in the mid-layer grains that reduced the trapping.

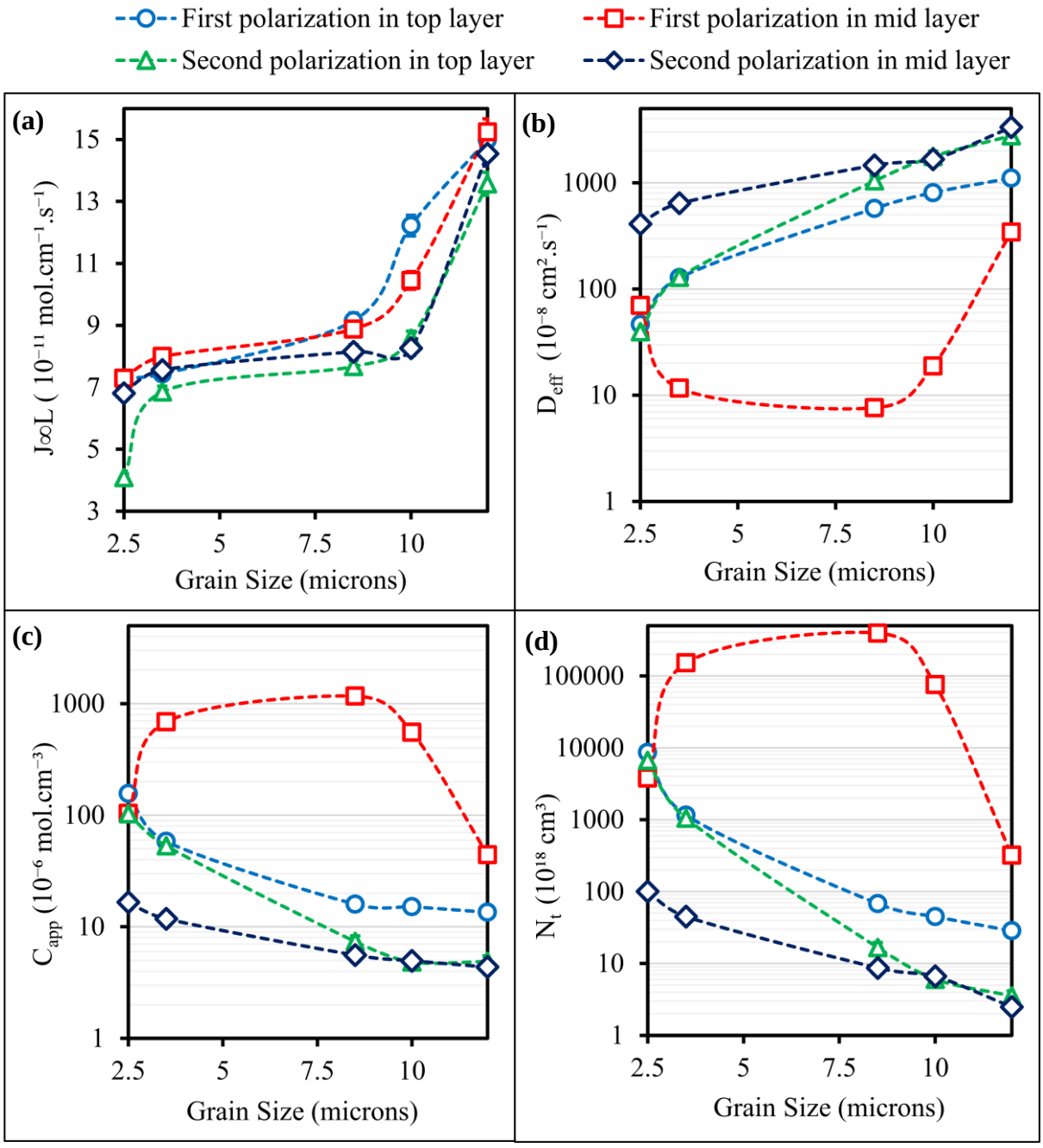

Figure 4.11. Effect of grain growth on diffusion in X70-1 steel: (a) permeability, (b) effective diffusion coefficient, (c) apparent solubility and (d) trapping sites.

Figure 4.11 also shows the effect of grain growth on the density of trapping sites. The measured trapping sites for the first and second polarization is the total and reversible traps in either layer

of the steel. The total traps include reversible and irreversible traps. The density of trapping sites decreased with grain growth in either layer. It should be related to the decreased number of triple junctions and grain boundaries for larger grains. The density of trapping sites in the second polarization is lower than that for the first polarization in either layer. It confirms that the total trapping sites contributed to the first polarization, while reversible trapping sites alone contribute to the second polarization. The density of reversible trapping sites for the top-layer is slightly more than that of the mid-layer. It should be related to the marginal increase in mid-layer grains that reduced the trapping by the lower number of triple junctions and grain boundaries. This proposition of considering the triple junctions and grain boundaries as reversible trapping sites can be validated from the HMT experiments.

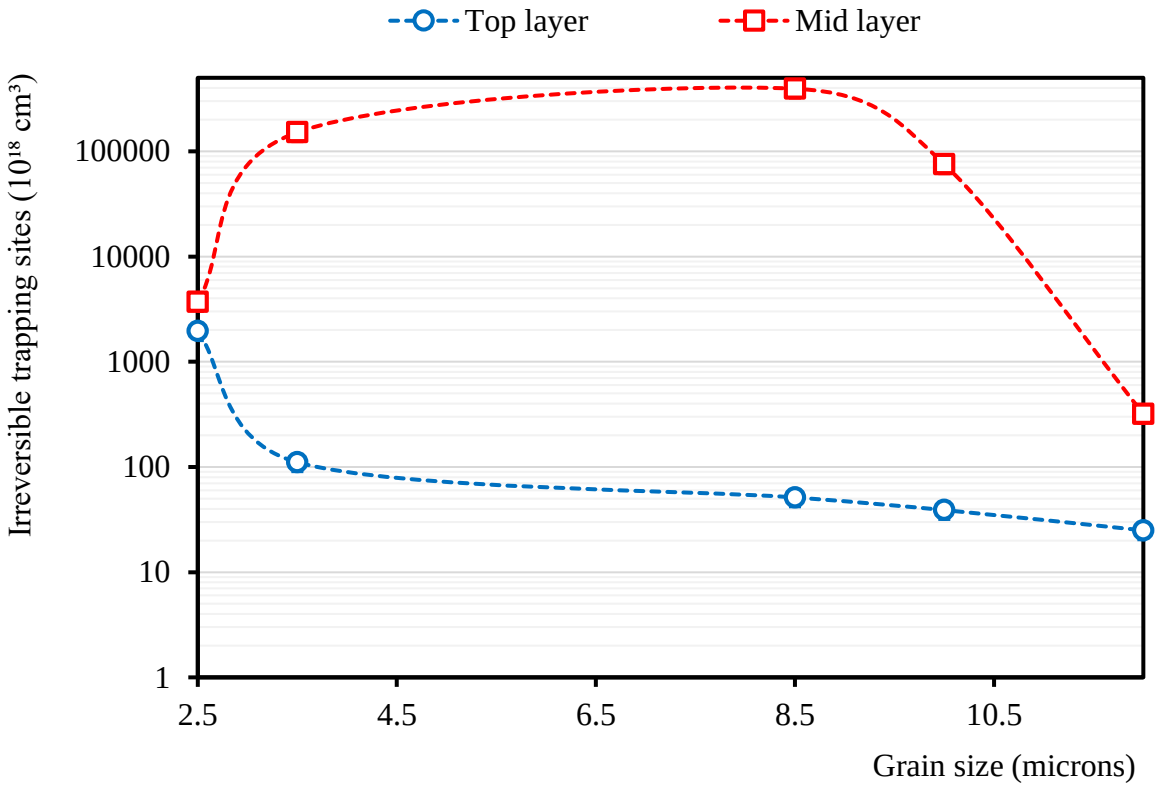

Figure 4.12. Effect of grain size on irreversible trapping in X70-1 steel.

Remarkably, the density of total trapping sites of the mid-layer shows initial growth and subsequent decay with grain growth. However, the density of reversible trapping sites of the mid-layer decreased for larger grains. These observations allowed in concluding the formation of irreversible trapping sites in the mid-layer. Precipitates are considered as an important source of irreversible traps [14]. Simm et al. reported precipitations of intermetallic compounds after annealing in steel [115]. Hence, annealing can also induce irreversible traps for the mid-layer samples. This proposition of additional traps in the mid-layer of an as-received and annealed

samples can be validated with the HMT experiments. Figure 4.12 shows the density of irreversible trapping sites in either layer of the steel. The density of irreversible trapping sites in the top-layer decreased with grain growth. Whereas, the mid-layer shows initial growth and subsequent decay for the density of irreversible trapping sites.

4.5. Influence of dislocations on hydrogen trapping in permeation tests

The five samples were removed from the mountings, and either side of the samples was repolished after characterizations. Also, a thin layer of palladium was coated on both sides. The dimensions of the sample, polishing procedure and specifications for the palladium coating were already explained. All the samples undertake the dual-polarized HP experiment. The HP experiments were performed at a standard room temperature of 23 ° C and a standard atmospheric pressure of 1 atm. The Gamry software was instantly recording the oxidized current that represents the permeated hydrogen through the sample. The values of steady-state current and time lag for the samples were captured from the permeation curve for each polarization. The permeability, effective diffusion coefficient, apparent solubility, and trapping sites were calculated based on the steady-state current and time lag.

Table 4.5 and Table 4.6 provides the calculated diffusion parameters and the density of different trapping sites after the first and second polarizations of the samples. Figure 4.13 shows the effect of mean KAM on the permeation parameters after the dual-polarized HP experiment. The permeability and effective diffusion coefficient decreased with the increase in mean KAM for both polarizations of the cold-rolled samples. It should be related to the increased hydrogen trapping by the induced dislocations after cold rolling. The permeability in the second polarization is lower than the first polarization, whereas the effective diffusion coefficient in the second polarization is higher than the first polarization. The steel sample becomes less porous after the saturation of irreversible traps after the first polarization. Hence, the hydrogen atoms travel a longer distance through the porous media before the oxidation in second polarization. Also, the average cross-sectional area in the porous medium available for hydrogen diffusion is increased. Then, the permeability measured as the rate of hydrogen flux through the sample is decreased, and the effective diffusion coefficient measured as the quantity of hydrogen that diffuses through the unit cross-sectional area of the sample is increased. Remarkably, the permeability of an as-received sample is less than 20 % and 40 % cold-rolled sample for either polarization. Popa et al. reported that new voids are formed after cold rolling [116]. The same authors reported that the number and size of the voids increased

with an increase in the degree of cold rolling. According to Ebnesajjad et al., permeation is considered as the movement of one species through the molecules of other species. However, the transport of materials through cracks, voids, or any other physical flaws should not accounts for permeation [117]. Hence, the formation of new voids after cold rolling and the penetration of hydrogen through these voids can increase the permeability of the as-received sample than the cold-rolled samples. The formation of new voids after cold rolling significantly increased the steady-state current by free permeation. However, it did not have any significant effect on the time lag, which mainly depends on the time elapsed for filling the dislocation traps formed during cold rolling. Thus, the initial increase in permeability can be related to the formation of new voids after cold rolling.

Table 4.5. Permeation parameters in cold-rolled X70-2 steel from the first polarization.

Mean KAM, Sample (degree)	Steady current, I_∞ ± 2.73 % (µA)	Time lag, T_L ± 12.29 % (s)	Permeability, $J_\infty L \times 10^{-11}$ ± 2.73 % (mol. $cm^{-1}.s^{-1}$)	Diffusion coefficient, $D_{eff} \times 10^{-8}$ ± 12.29 % ($cm^2.s^{-1}$)	Apparent solubility, $C_{app} \times 10^{-6}$ ± 12.59 % (mol. cm^{-3})	Trapping sites, $N_t \times 10^{18}$ ± 17.59 % (cm^3)
A (0.33)	76.92	673	7.97	250.18	32.20	331.00
B (1.14)	90.98	1390	9.43	119.90	78.63	1669.20
C (1.71)	82.91	2334	8.59	71.41	120.31	4304.97
D (1.87)	56.06	10624	5.81	15.69	370.28	60572.11
E (1.98)	30.08	14646	3.12	11.38	273.96	61803.80

Table 4.6. Permeation parameters in cold-rolled X70-2 steel from the second polarization.

Mean KAM, Sample (degree)	Steady current, I_∞ ± 2.73 % (µA)	Time lag, T_L ± 12.29 % (s)	Permeability, $J_\infty L \times 10^{-11}$ ± 2.73 % (mol. $cm^{-1}.s^{-1}$)	Diffusion coefficient, $D_{eff} \times 10^{-8}$ ± 12.29 % ($cm^2.s^{-1}$)	Apparent solubility, $C_{app} \times 10^{-6}$ ± 12.59 % (mol. cm^{-3})	Trapping sites, $N_t \times 10^{18}$ ± 17.59 % (cm^3)
A (0.33)	65.43	530	6.78	326.01	21.65	178.57
B (1.14)	77.42	1302	8.02	128.01	62.68	1245.57
C (1.71)	71.36	2128	7.39	78.32	94.41	3078.47
D (1.87)	45.14	2438	4.68	68.36	68.42	2557.88
E (1.98)	13.02	3962	1.35	42.07	32.08	1953.25

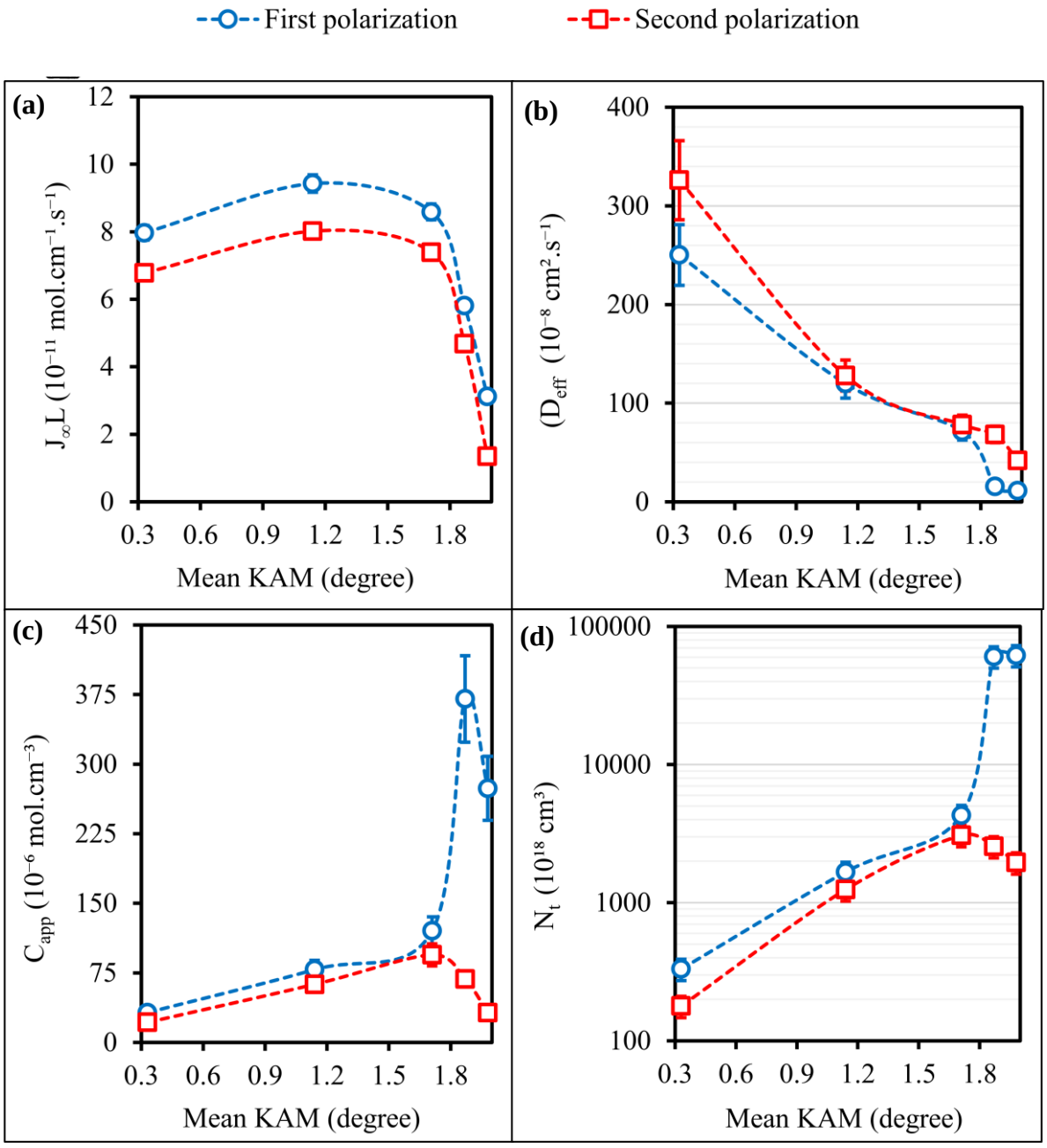

Figure 4.13. Effect of mean KAM on diffusion in X70-2 steel: (a) permeability, (b) effective diffusion coefficient, (c) apparent solubility and (d) trapping sites.

Figure 4.13 also shows the changes in the apparent solubility and density of trapping sites with an increase in the mean KAM. The apparent solubility shows an initial growth and subsequent decay with the increase in mean KAM for either polarization. This observation can be related to the type of traps formed after cold rolling. There was a sudden increase in the apparent solubility for a mean KAM from 1.7° to 1.9° in the first polarization, and the apparent solubility in the second polarization begins to decrease from a mean KAM of 1.7°. This observation can

be related to the shift of reversible traps into irreversible traps. Hence, the density of the reversible trapping sites shows growth and decay with the increase in mean KAM. The trend in the trapping sites can be related to the occurrence of a particular value of the KAM angle that can differentiate a reversible and irreversible trap. The apparent solubility in the first polarization was higher than the second polarization, and it occurs due to the increased hydrogen accumulation at the traps during the first polarization. The density of trapping sites for the first polarization was higher than in the second polarization. This observation is due to the saturation of irreversible traps after the first polarization.

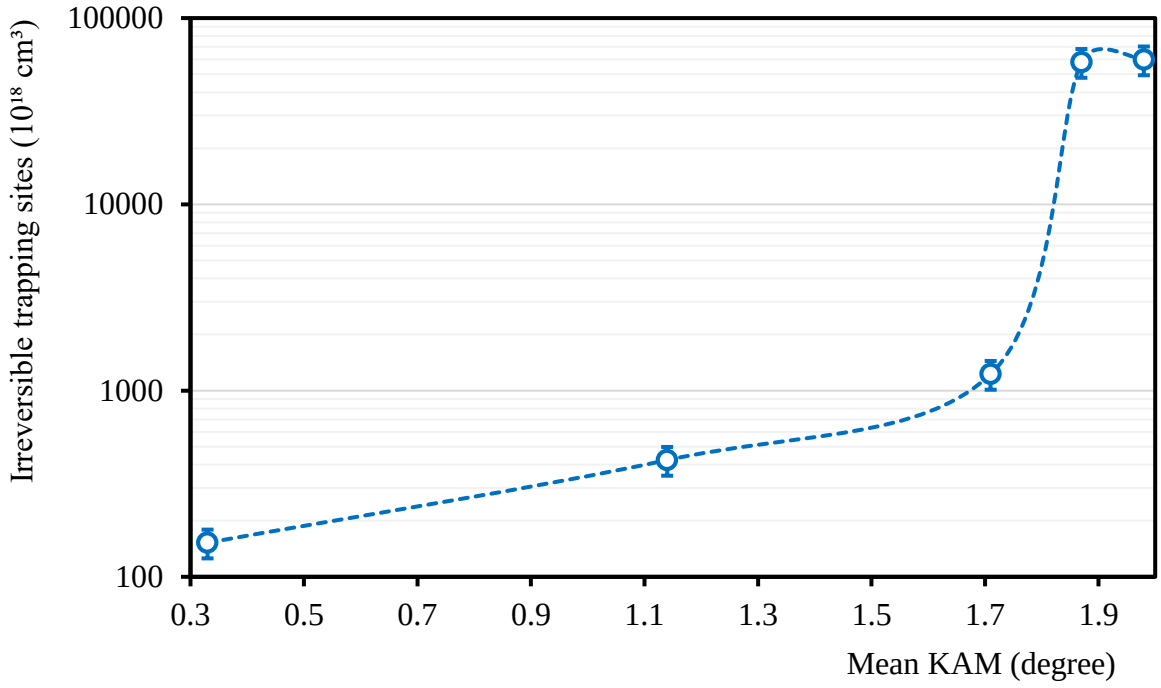

Figure 4.14. Effect of mean KAM on irreversible trapping in X70-2 steel.

The difference in the density of trapping sites from either polarization is presented as irreversible trapping sites in Figure 4.14. The density of irreversible trapping sites increased with the increase of mean KAM for the tested samples, and it was most visible for a mean KAM from 1.7º to 1.9º. The occurrence of higher KAM angles for the highly deformed sample should be related to the increase of density of irreversible traps. Hence, there was a decline in the density of reversible trapping sites for a mean KAM from 1.7º to 1.9º.

4.6. Imaging the hydrogen diffusion path by microprint method

The duplicate of as-received samples (M1 and A), annealed sample (T5 and M5) and cold rolled sample (C) were used in the HMT experiments. The different locations of the samples undergo simultaneous EDS analysis to validate the SEM observations at the end of HMT experiments. All the SEM images were taken inside a working distance, the distance between

the specimen and the final lens, of 8 - 10 mm. The accelerating voltage was calibrated close to 20.0 kV for the best visualization of the steel microstructure and the superimposed particles from the HMT experiment. The EDS analysis was also performed with the same conditions of the SEM characterization. The magnification was adjusted according to the desired visualization from the images. Characterizations were performed in multiple locations of the same sample, and selected results were reported.

4.6.1. Visualization of the diffusion path in an as-received steels

Sample M1, from the mid-layer of X70-1 steel and, sample A, from the top layer of X70-2 steel, are chosen for the HMT experiments in this section. After the HMT experiment, SEM and EDS characterization were performed at different locations of the same sample.

4.6.1.1. As-received X70-1 steel from the mid-layer

Figure 4.15 shows the SEM images from two different locations of sample M1 after the same HMT experiment. There is a partial diffusion of hydrogen through one region of the sample, as shown in the first micrograph. Another area of the same sample shows a complete diffusion in the second micrograph. The observation of white spherical particles overlaid on the microstructure illustrated the hydrogen escape. The higher number of white particles in the second micrograph compared to the first micrograph shows the partial and complete diffusion of hydrogen through the steel microstructure. The etching of the sample before HMT allowed the microstructural observation from the same SEM images. The first micrograph showed that the grain boundaries are contributing to the escape of the hydrogen atom from the sample.

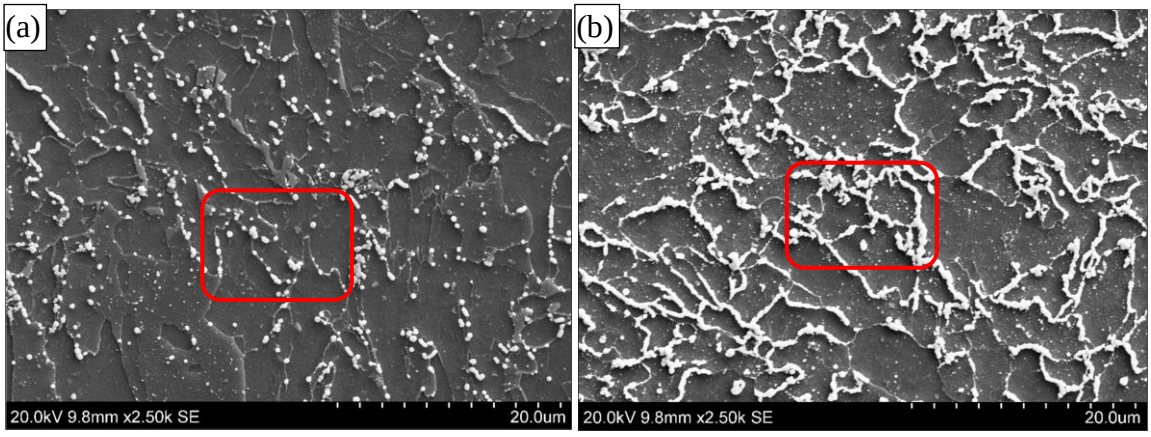

Figure 4.15. SEM images in sample M1: (a) partial diffusion and (b) complete diffusion.

The magnified SEM and EDS characterizations from the rectangular area of the micrographs in Figure 4.15 are presented as partial diffusion in Figure 4.16 and after a complete diffusion

in Figure 4.17. The particle size of several hundred nanometers to almost one micron represented the amount of diffused hydrogen. The black and intense green spots in the iron (Fe) and silver (Ag) maps from the EDS analysis confirmed the white particles as metallic silver. The complete diffusion micrograph visualized the white particles over the grain boundaries and white particle clusters at the triple junctions. The comparison of the EDS spectrum for the partial and complete diffusion showed an enhanced hydrogen discharge for complete diffusion. The non-uniform diffusion should occur by uneven emulsion coating and hydrogen bubble formation in the test setup. The preferential diffusion through the grain boundaries and triple junctions, after immediate hydrogen discharging, allowed in considering them as reversible trapping sites. Figure 4.18 shows preferential hydrogen diffusion through the triple junctions of sample M1. The SEM and EDS characterizations allow in concluding that there is a higher rate of diffusion through the triple junctions than through the grain boundary.

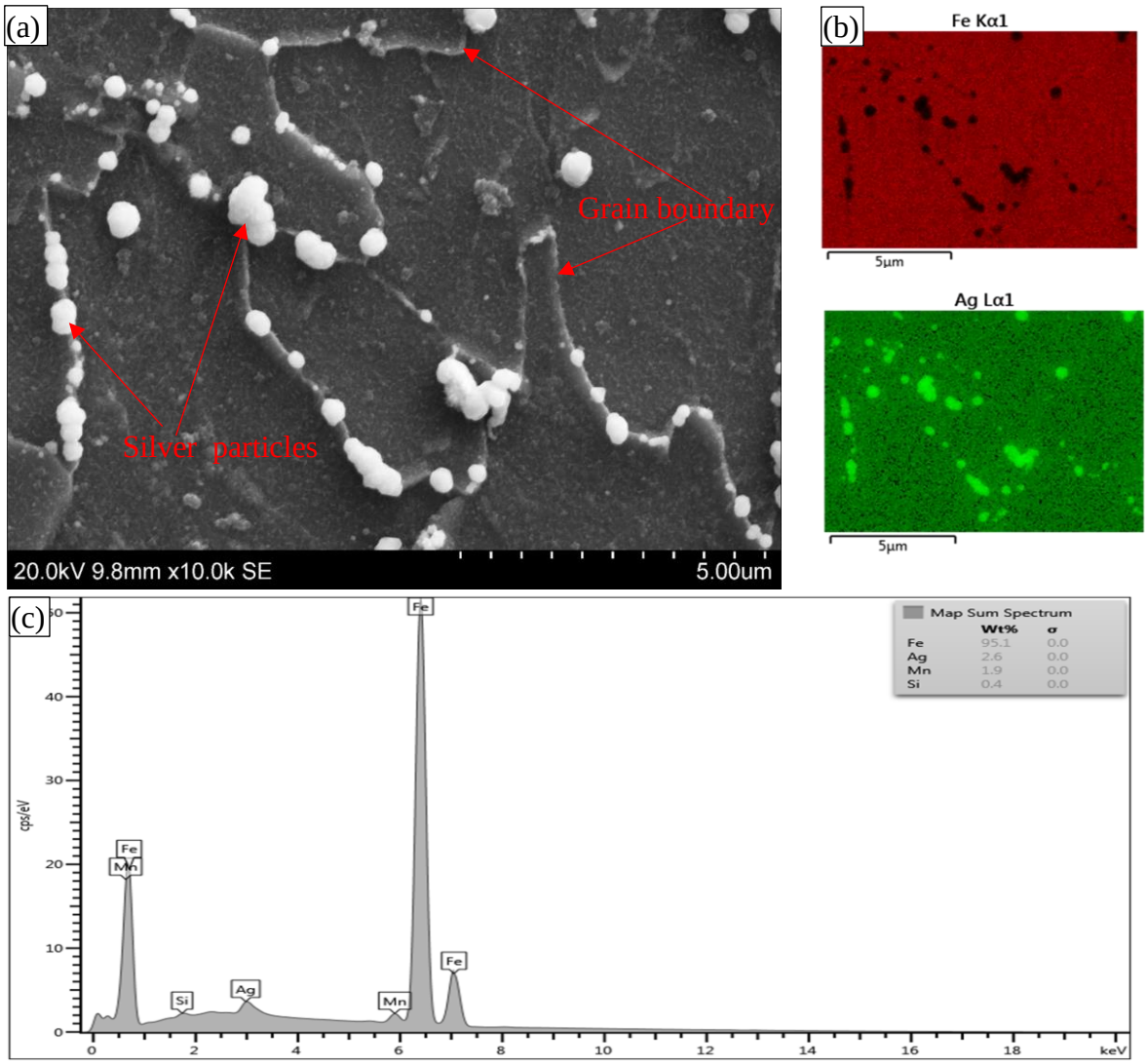

Figure 4.16. Partial diffusion in M1: (a) SEM image, (b) EDS map and (c) EDS spectrum.

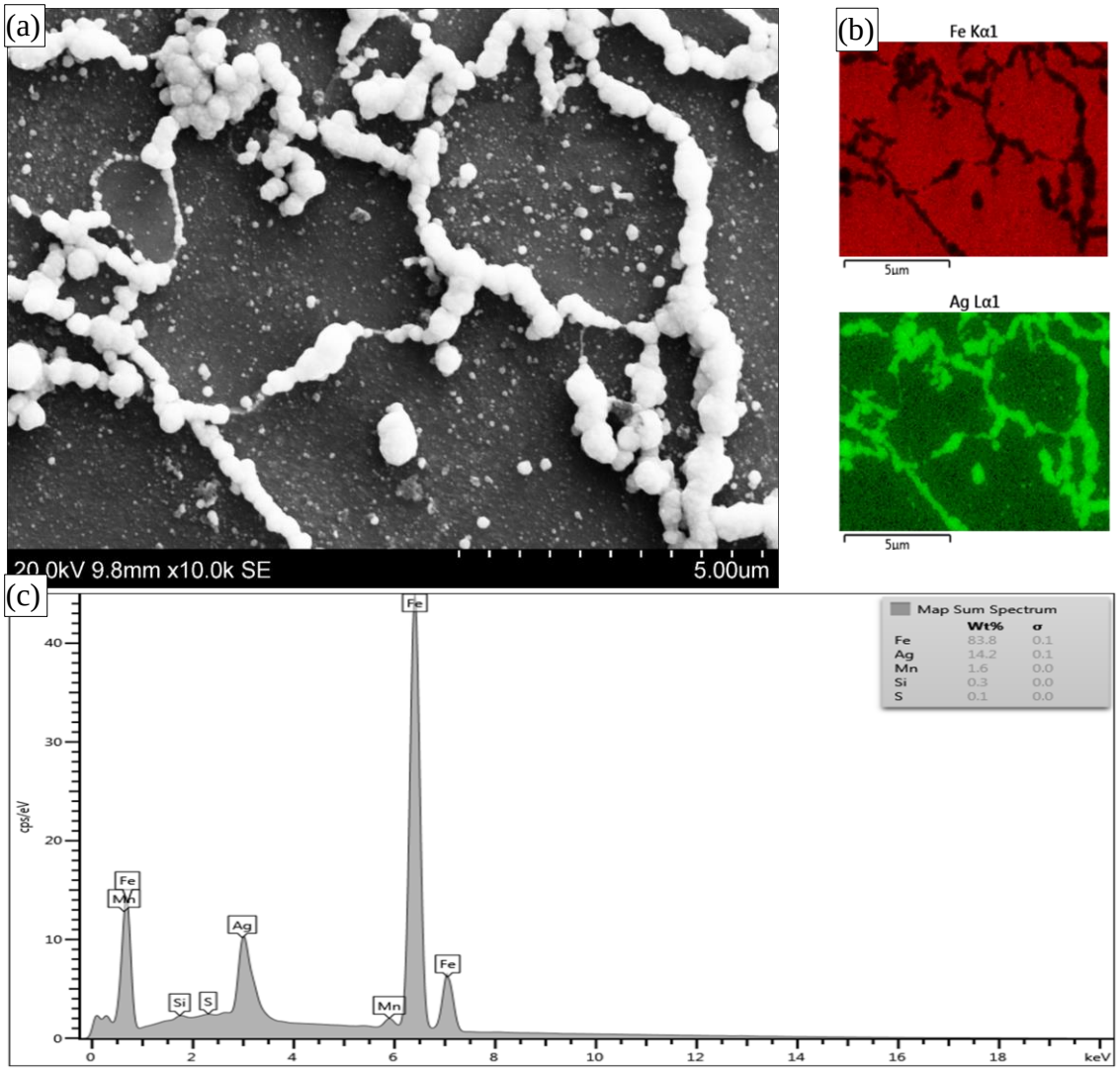

Figure 4.17. Complete diffusion in M1: (a) SEM image, (b) EDS map and (c) EDS spectrum.

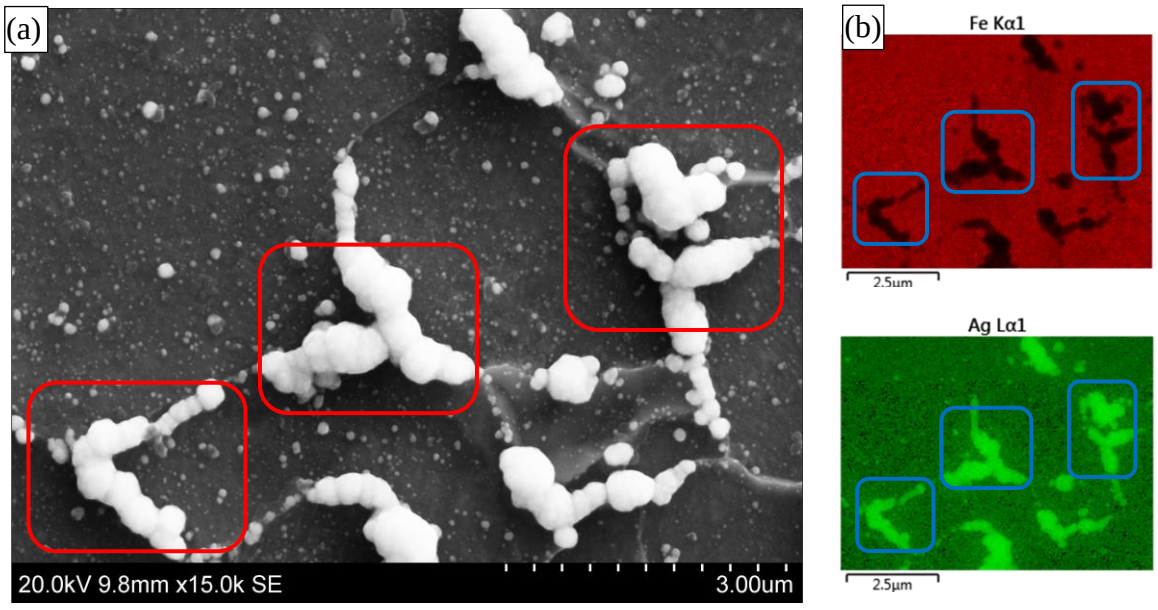

Figure 4.18. Diffusion at triple junctions in sample M1: (a) SEM image and (b) EDS map.

The non-metallic inclusions of different sizes, compositions and quantities are formed in liquid metal during refining and solidification. The nonmetallic inclusions in steel usually include oxides, sulfides, oxy-sulfides, nitrides, carbides, and carbonitrides. However, the latter three are considered as precipitates [118]. Figure 4.19 shows the SEM images of the hydrogen diffusion path around different inclusions in sample M1. The first micrograph is the visualization around a single inclusion. There are two inclusions adjacent to each other in the second micrograph. There is a partial diffusion through the matrix, as shown by the overlaid white particles in both micrographs. Remarkably, there is an evolution of a circular pattern, resembling overlaid white particles around the inclusions. The circular pattern is dominant for the double inclusions, and hence, it should be a characteristic of the inclusions. The same sample shows a circular pattern around inclusions in many locations, and the literature never reported such observation. The circular pattern encircling an inclusion may be related to the distorted and cracked matrix around the inclusion that can support the preferential diffusion. However, matrix cracking is not identified. The diameter of the circular pattern varied from 4 to 8 and 8 to 16 microns in the single and double inclusions.

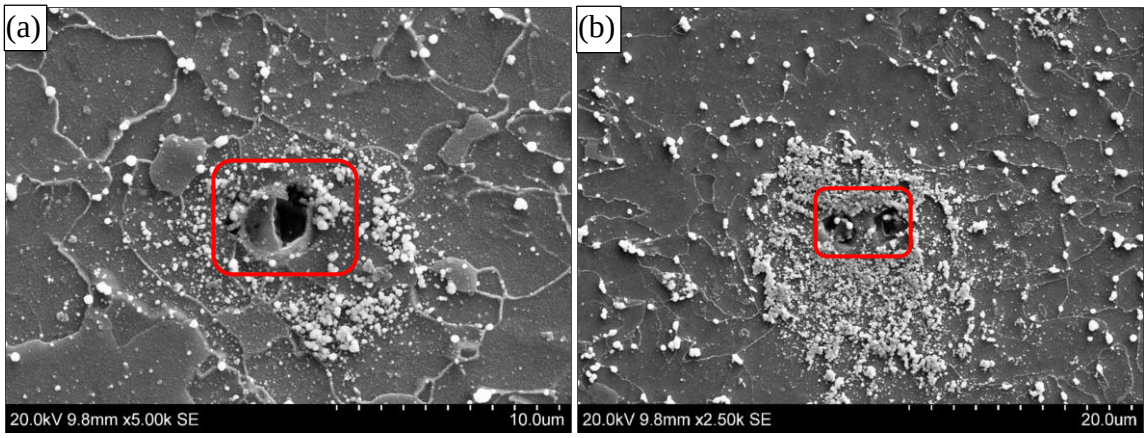

Figure 4.19. SEM images at two locations in sample M1: (a) single inclusion and (b) double inclusion.

The rectangular emphasized area from Figure 4.19 is presented with magnified SEM images and its EDS analysis. The single inclusion is in Figure 4.20, and the double inclusion is in Figure 4.21. The single inclusion, about 3.5 microns in diameter, is spherical in morphology and enclosed by the overlaid white particles. Those white particles are confirmed as being made of metallic silver by the increased intensity in the Ag map and the occurrence of strong Ag peak on the EDS spectrum. The inclusion is a combination of titanium, aluminum, manganese, and copper formed as some sulfides. The formation of such spherical inclusions with variable elemental composition during solidification of steel agrees with the literature [119].

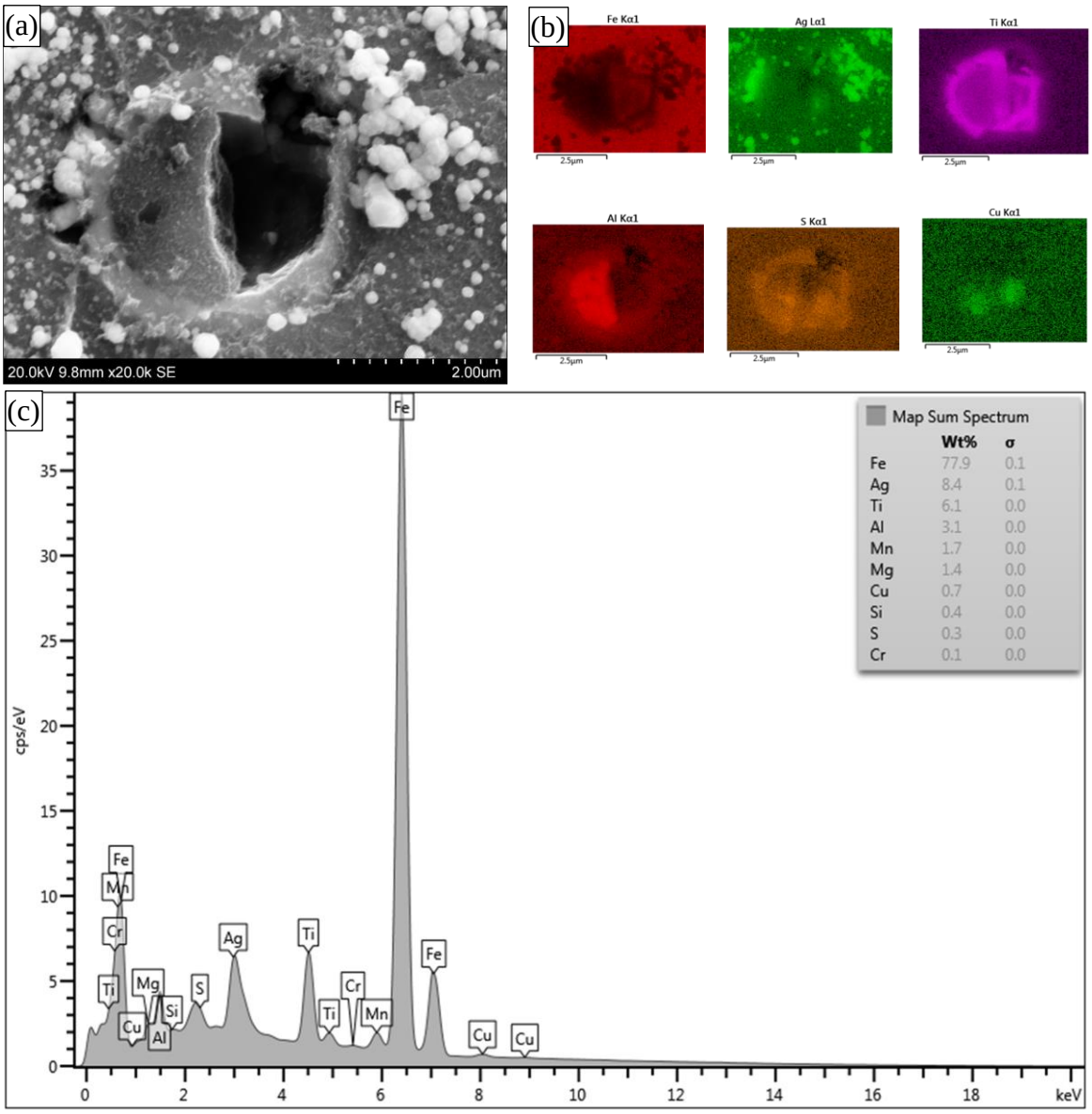

Figure 4.20. Hydrogen diffusion around a single inclusion in sample M1: (a) SEM image, (b) EDS map and (c) EDS spectrum.

Remarkably, the relative intensity of each element in the EDS maps shows that titanium encloses aluminum, copper, and sulfur in the inclusion. The double inclusion micrograph has two spherical inclusions adjacent to each other. Noticeably, the matrix between the inclusions does not have many white particles. However, there is a cluster of overlaid white spheroidal silver particles around these inclusions. The two inclusions consist of aluminum and titanium, and from the literature, aluminum usually forms oxides and titanium precipitates as carbides and nitrides [119]. However, there were no identifiable oxides, carbides, and nitrides formed during the EDS analysis. Also, the inclusions measured approximately 3 microns, and the matrix between them is measured as 1.5 microns.

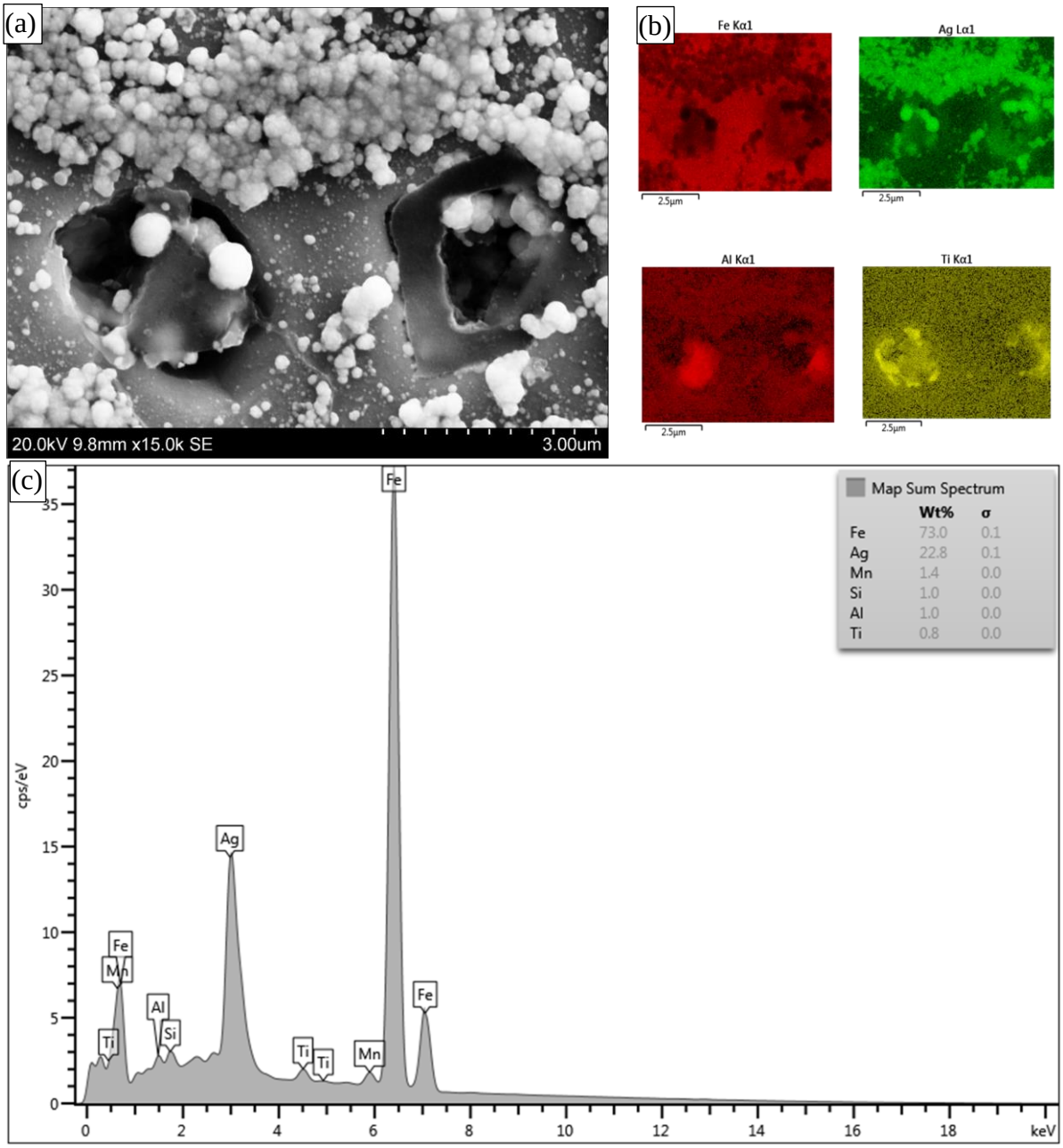

Figure 4.21. Hydrogen diffusion around a double inclusion in sample M1: (a) SEM image, (b) EDS map and (c) EDS analysis.

4.6.1.2. As-received X70-2 steel from the top-layer

The SEM images from different locations of sample A were taken after the same HMT experiment. The overlaid circular pattern with white particles is also observed in sample A. The observations similar to sample M1 is not presented to avoid the repetitions. However, Figure 4.22 shows another unreported observation after the SEM and EDS characterizations of sample A. The micrograph shows the hydrogen diffusion path around a single inclusion. Remarkably, the evolution of a circular pattern of white particles around the inclusions does

not happen here. However, the white superimposed spheroidal particles are observed at the interface between the matrix and inclusion. The white particles are also seen at the boundary between different elements in the inclusion. Also, the white particles are located at some grain boundaries.

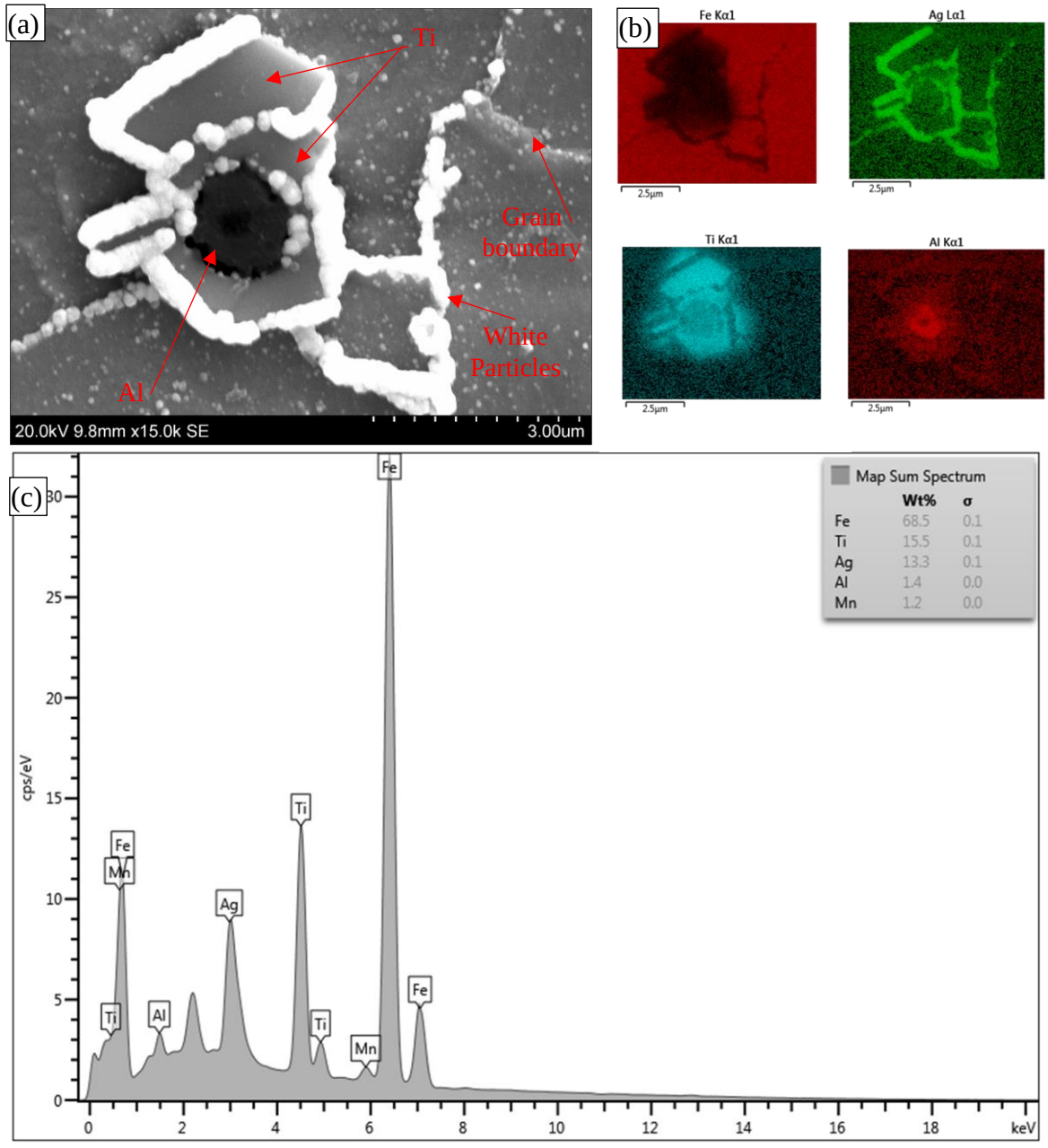

Figure 4.22. Hydrogen diffusion around the inclusion in sample A: (a) SEM image, (b) EDS map and (c) EDS spectrum.

The figure also marks the grain boundaries, white particles, and elemental compositions of the inclusion. The inclusion has an irregular shape with a dimension of 2.5 to 3.5 microns. It comprises of a layer of titanium enclosing a spheroidal aluminum area as identified in Ti and

Al maps from the EDS analysis. The occurrence of the Ti and Al peaks in the EDS spectrum and the concentration of elements in the normalized weight percentage of the sample indicated the same. The spheroidal aluminum part of the inclusion measured approximately 1.5 microns in size. The observations allow in concluding that there is a significant amount of hydrogen diffusion through the interfaces of the matrix and inclusion. Also, the intensity of this hydrogen flux is higher than that through the grain boundaries. However, higher hydrogen diffusion occurred at the interface separating different elements. Also, this diffusion is higher than that at the grain boundaries and lower than that at matrix-inclusion interfaces. Inclusions are considered reversible and irreversible traps based on their binding energy with the hydrogen. As there is no circular pattern around this particular inclusion, it should be considered as an irreversible trap. Hence, the circular pattern around inclusion should be used in support of the storage of hydrogen in the reversible traps during the first one hour of electrochemical hydrogen charging. The stored hydrogen in the reversible traps acted as a local source of hydrogen after one hour and diffused around the inclusion by producing a circular pattern of superimposed white metallic silver particles during the HMT experiment. Therefore, the presence and absence of a circular pattern of white metallic silver particles around inclusion should be considered as a method to determine the type of trap represented by them.

4.6.2. Visualization of the diffusion path in an annealed X70-1 steel

The preferential diffusion through triple junctions and grain boundaries in sample M1 was also observed in sample T5. Figure 4.23 visualizes the preferential hydrogen diffusion through two locations of sample T5 that contain degenerate pearlite (DP). The observations are after the same HMT experiment. The literature reported the occurrence of DP in X70 steel [120]. The block of ferrite and colony of lath-shaped cementite in the DP are identified and marked accordingly in the micrographs. The partial diffusion micrograph indicated that the cementite diffuses the hydrogen, and the complete diffusion micrograph supports the same with the observation of clustered white particles over the cementite. Also, the ferrite in the DP does not have any overlaid white particles. Figure 4.23 also presents the SEM images and EDS analysis of partial and complete diffusion through the magnified DP. The partial diffusion micrograph shows that the boundaries of the cementite lath appear to discharge more hydrogen as most of the white particles are visualized at the lath boundaries. The complete diffusion micrograph shows that the grain boundaries are a preferential hydrogen diffusion path than the bulk of the grain. However, the cementite also shows a cluster of white particles. This observation allows in concluding a high hydrogen diffusion through cementite than the grain boundary.

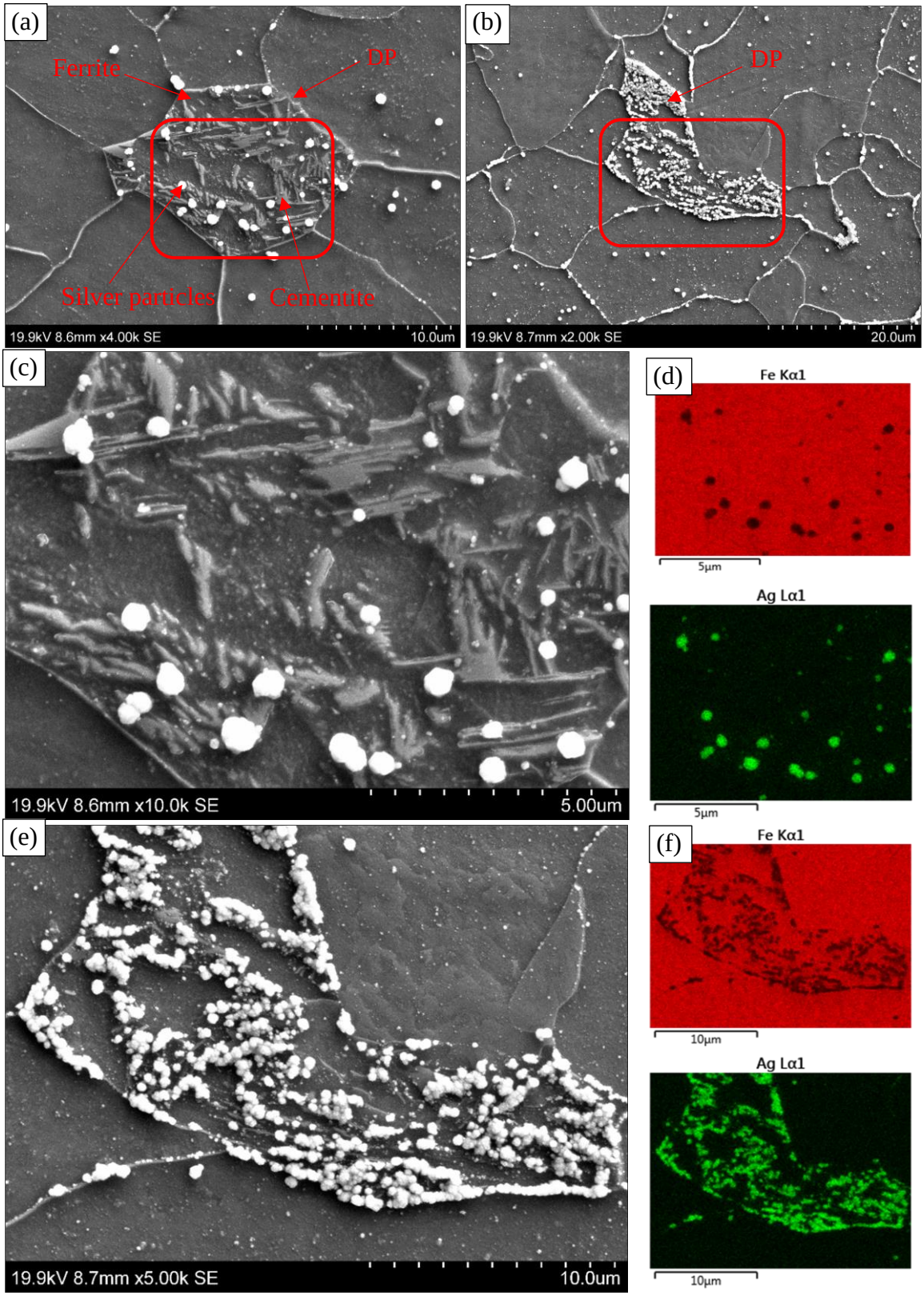

Figure 4.23. Preferential diffusion in sample T5: (a) SEM image of partial diffusion, (b) SEM image of complete diffusion, (c) SEM image of partial diffusion in DP, (d) EDS map of partial diffusion in DP, (e) SEM image of complete diffusion in DP and (f) EDS map of complete diffusion in DP.

The presence and absence of a circular pattern of white superimposed particles around the inclusion are reported with sample M1 and A. The observations from as-received samples are representing the reversible and irreversible traps. Figure 4.24 shows another reversible trap in a single inclusion and a double inclusion with a combination of an adjacent reversible and irreversible trap from different locations in sample T5. The single inclusion is spherical, whereas the double inclusion is a combination of spherical and cubic inclusion. The identified inclusion morphologies agreed with the literature [119]. The single inclusion had a circular pattern of white particles. However, the circular pattern is not uniform for the double inclusion. The white particles cover the periphery of the pattern, the top portion of the spherical inclusion and remain unoccupied around the cubic inclusion. The peculiar observations for the double inclusion indicated the formation of a reversible trap at spherical inclusion and an irreversible trap at cubic inclusion.

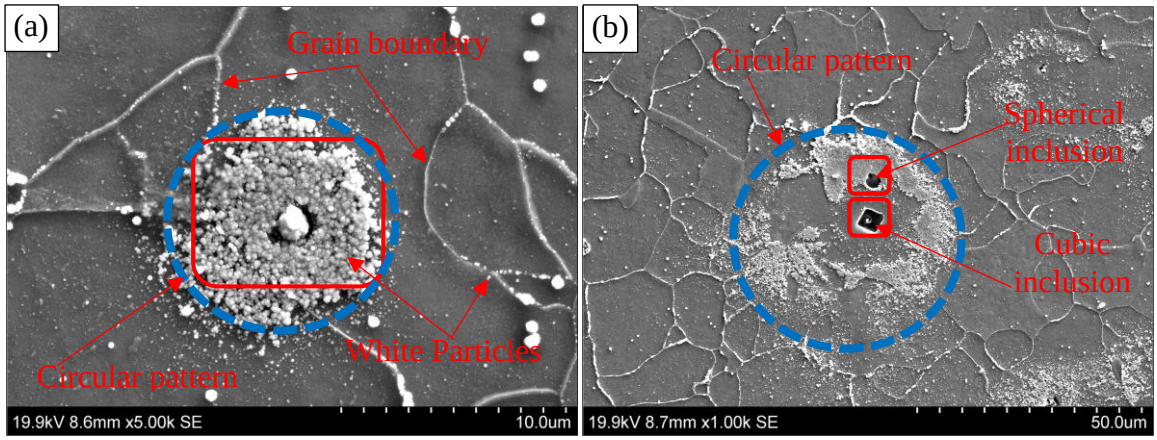

Figure 4.24. SEM images in sample T5: (a) single inclusion and (b) double inclusion.

Figure 4.25 represents the visualization results from the magnified area of the single inclusion of sample T5. The SEM image shows the superimposed circular pattern around the single inclusion and few white particles over the inclusion. As reported earlier, the elemental interfaces in the inclusion are considered as a preferential hydrogen diffusion path. Hence, the white particles overlay on the inclusion. The single inclusion has a spherical morphology, and it is approximately 2 microns in size. EDS results indicated the formation of manganese sulfide inclusion, and the literature reported the same inclusion as hydrogen trapping sites in pipeline steels [63]. Additionally, the circular pattern around the single inclusion indicated it as a reversible trapping site. Figure 4.26 shows the SEM and EDS observations of the two inclusions from the double inclusion of Figure 4.24. The two inclusions, identified as a cubic inclusion and a spherical inclusion, should be considered as an irreversible and reversible trap based on the overlaid white particles in the pattern formation.

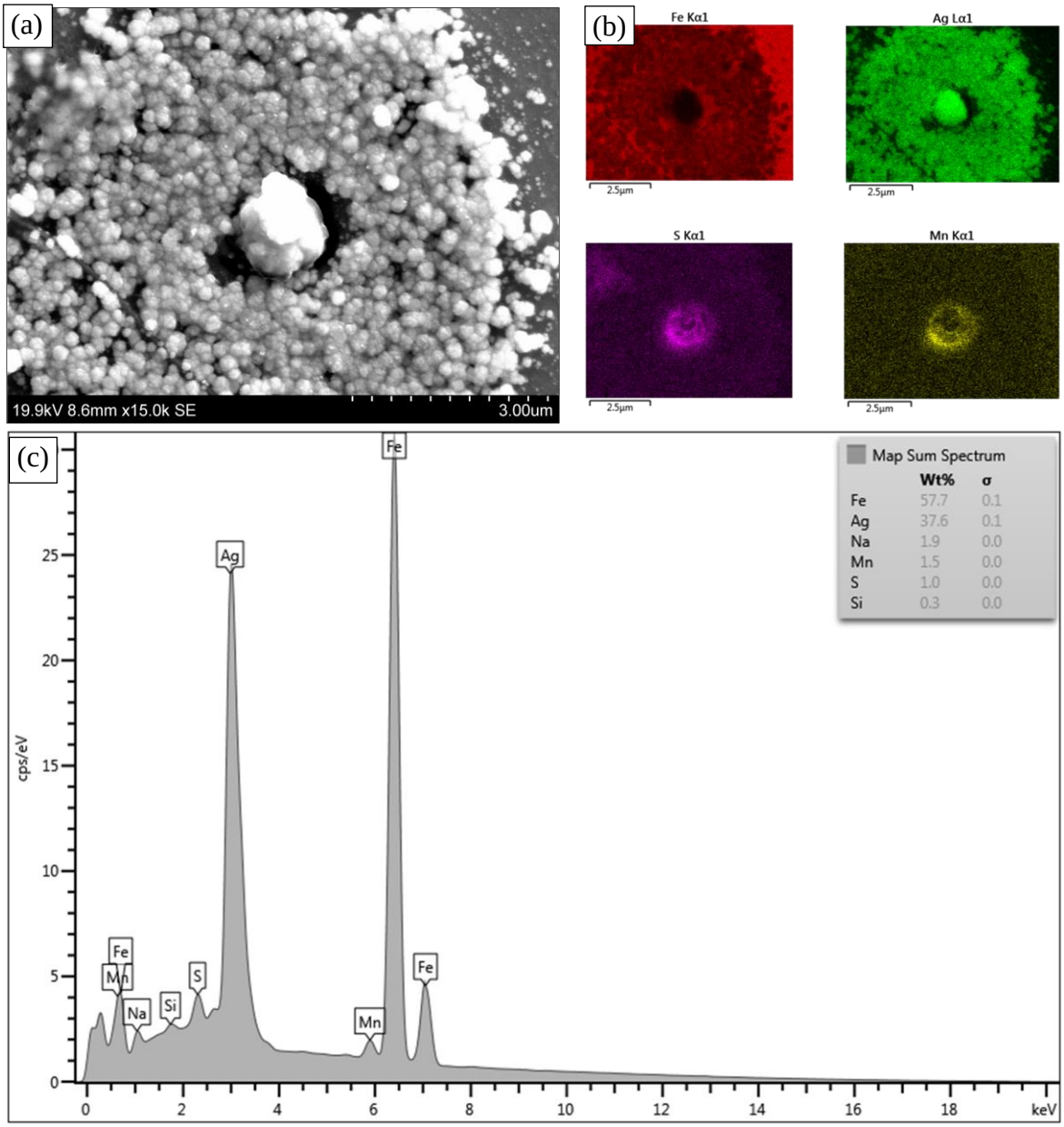

Figure 4.25. Hydrogen diffusion around a single inclusion in sample T5: (a) SEM image, (b) EDS map and (c) EDS analysis.

The magnified SEM image shows that the cubic inclusion does not have a circular pattern in the immediate surrounding matrix. However, the interfaces of inclusion and matrix with superimposed white particles indicated preferential hydrogen diffusion and agreed with observation presented by Luu et al. [63]. Also, the elemental interfaces support superior hydrogen diffusion as visualized by the overlaid white particles in the cubic inclusion. The EDS analysis shows the white particles as metallic silver and the inclusion as a combination of titanium, manganese, silicon, and sulfur. Researchers already reported the formation of titanium-based cubic inclusions [119], and hence, the EDS observation looks meaningful.

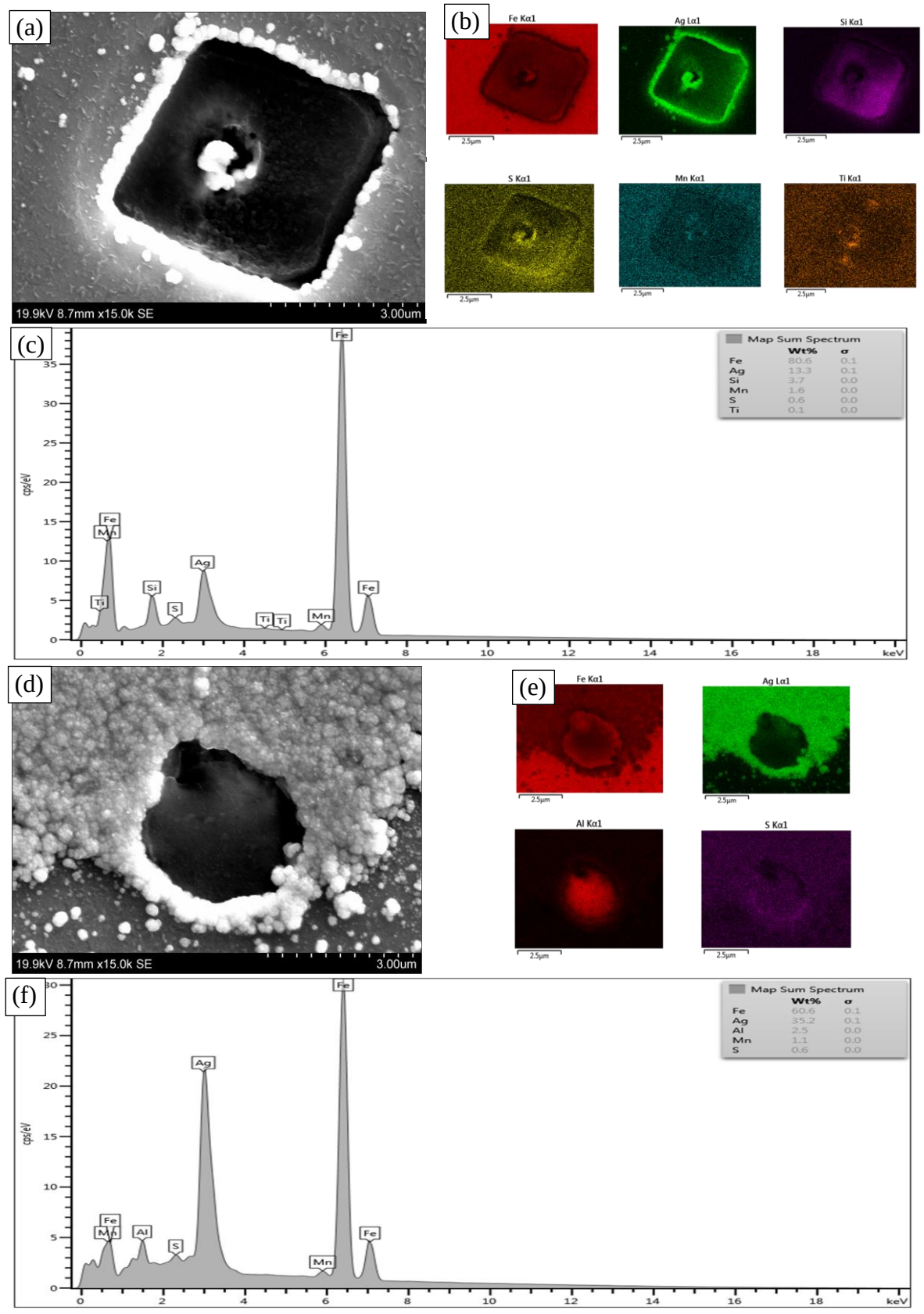

Figure 4.26. Double inclusion in sample T5: (a) SEM image of cubic inclusion, (b) EDS map of cubic inclusion, (c) EDS spectrum of cubic inclusion, (d) SEM image of a spherical inclusion, (e) EDS map of a spherical inclusion and (f) EDS spectrum of a spherical inclusion.

The white overlaid particles form a semicircular pattern on the top portion of the spherical inclusion, and it occurred by the diffusion of reversibly stored hydrogen after the electrochemical hydrogen charging. The white particles are again observed at the interfaces of the spherical inclusion and the matrix. Therefore, the matrix-inclusion interface indicated preferential hydrogen diffusion and agreed with the literature [63]. The EDS results confirmed aluminum and sulfur as the significant contributors to the inclusion. The absence and presence of an overlaid circular pattern of white particles around the inclusions allow in considering the cubic inclusion as an irreversible trap and the spherical inclusion as a reversible trap.

4.6.3. Visualization of diffusion path in as-received and annealed mid-layer X70-1 steel

Figure 4.27 shows the EDS analysis of mid-layer samples after different HMT experiments. The as-received steel, sample M1, contains titanium-based inclusion, whereas the annealed steel, sample M5, contains manganese-based inclusion. The circular pattern of silver particles around inclusions represented the hydrogen escaping sites. The immediate discharging of reversible hydrogen after cathodic charging in the HMT experiment allows in considering that the circular pattern occurs by the diffusion of trapped hydrogen from the inclusions. The circular pattern can also be related to the cracked matrix around the inclusion. However, matrix cracking around inclusion is not identified. In any case, the as-received and annealed samples in the mid-layer contain inclusions that affect the permeation results. As per the proposed method of trap classification, the two inclusions with a circular pattern of silver particles around them should be considered as reversible trapping sites.

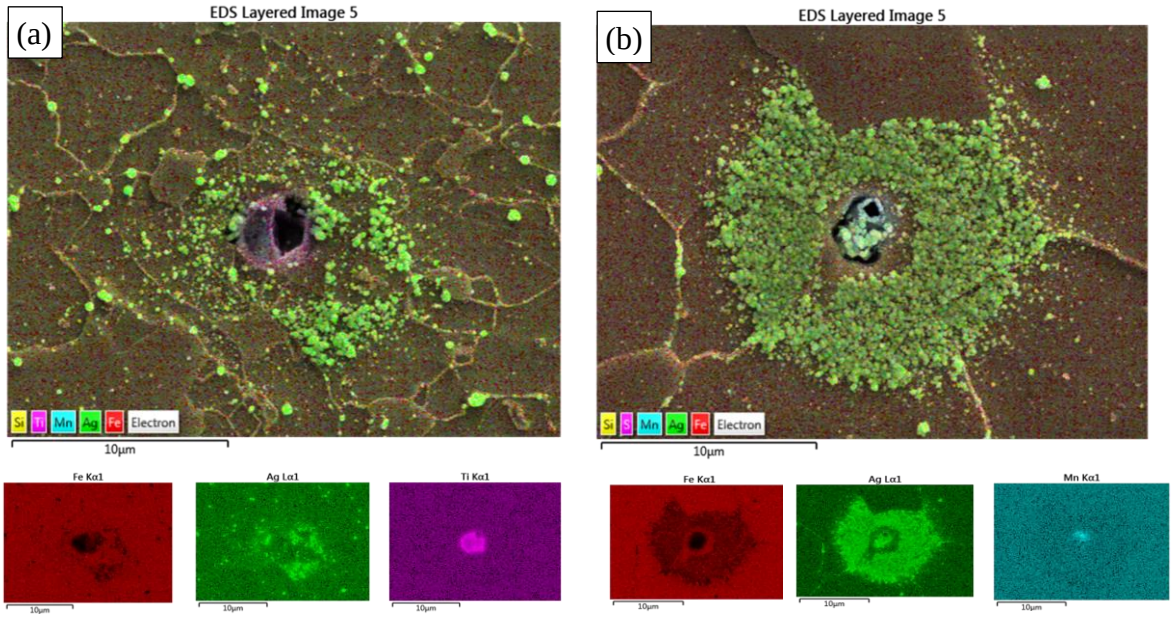

Figure 4.27. EDS analysis after the HMT experiment: (a) sample M1 and (b) sample M5.

4.6.4. Visualization of diffusion path in cold-rolled X70-2 steel

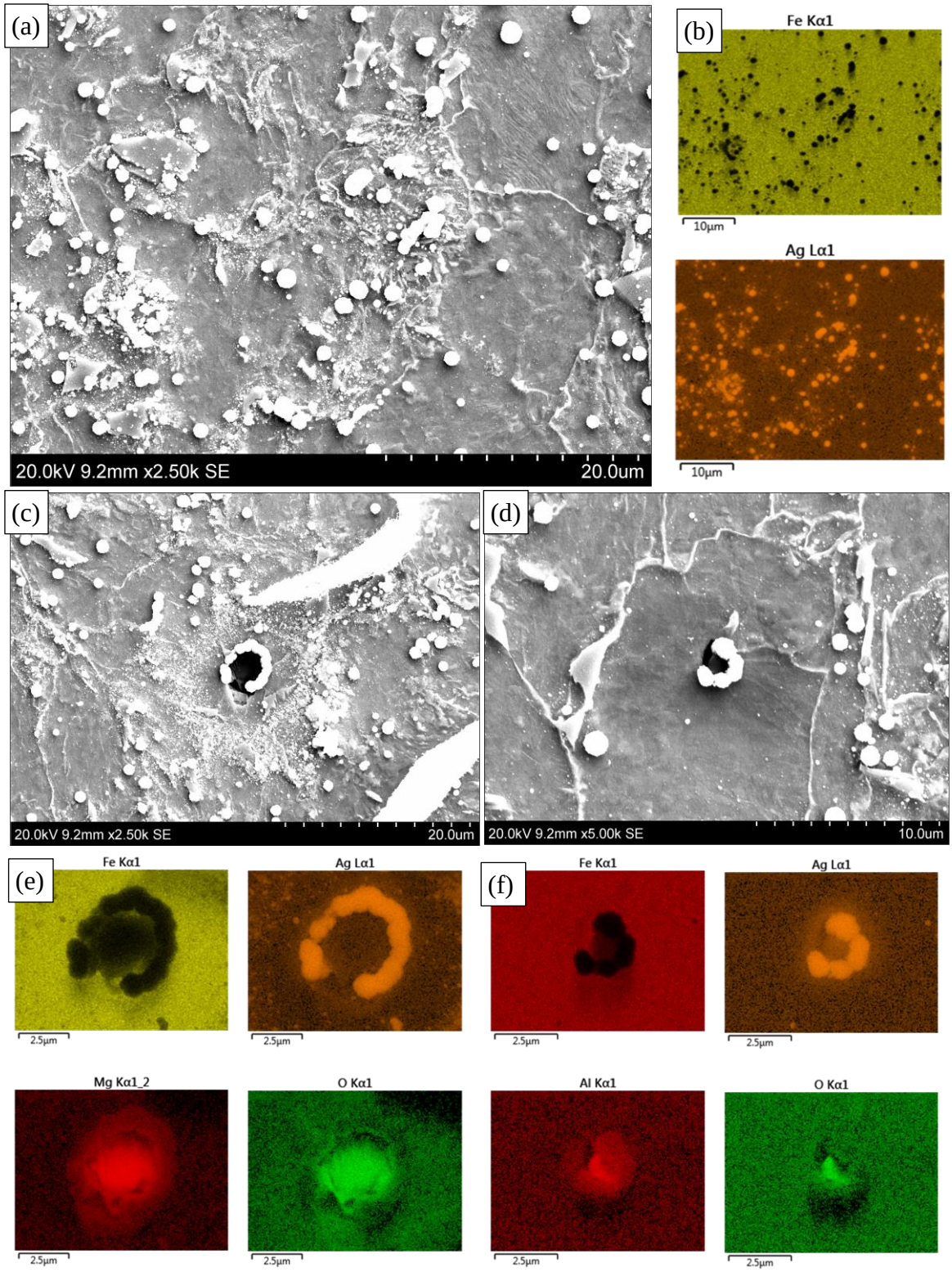

Figure 4.28. Sample C from HMT: (a) SEM image of deformed grain, (b) EDS map of deformed grain, (c) SEM image of reversible inclusion, (d) SEM image of irreversible inclusion, (e) EDS map of reversible inclusion and (f) EDS map of irreversible inclusion.

The HMT experiment used the duplicate of sample C in a 40 % cold rolled condition. The first permeation of sample C shows a time lag of less than one hour in the dual-polarized HP experiment. Hence, sample C was used instead of a highly deformed sample in the HMT experiment. Figure 4.28 shows the SEM images and EDS maps of sample C at three different regions after the same HMT experiment. The three images are sensibly chosen to visualize the hydrogen diffusion at deformed grains, reversible inclusion and irreversible inclusion. The white overlaid spherical particles on the microstructure in all the SEM images are identified as metallic silver by EDS analysis. In the first SEM image, there are few non-deformed grains between the deformed grains. The white particles are mostly covered on deformed grains, and it indicated that the induced dislocations act as a reversible trapping site and immediately discharge the trapped hydrogen after the electrochemical charging. The non-deformed grains are left uncovered with white particles and appeared similar to the as-received steel. The second SEM image shows a spherical inclusion with an encircled pattern of white particles. Hence, it can be considered as a reversible inclusion. However, the white pattern is absent for the other spherical inclusion in the third SEM image. Hence, it belongs to the irreversible traps. The preferential hydrogen diffusion through the matrix-inclusion interface is observed in both inclusions. The analysis of the SEM images shows that preferential hydrogen increased in the order of deformed grains and matrix-inclusion interfaces with matrix inclusion interfaces being the most diffusable path in the deformed steel. The analysis of EDS maps shows that both spherical inclusions are formed from aluminum and oxygen. The reversible spherical inclusion measured 4 microns, whereas the irreversible spherical inclusion measured 2 microns in size.

CHAPTER 5

CONCLUSIONS AND FUTURE WORK

5.1. Overview

The first half of the chapter contains the conclusions from the study of hydrogen diffusion and accumulation in X70 pipeline steel. The final half of the chapter includes the recommendation for future works based on the expertise gained after this research.

5.2. Conclusions

The deliverables from each thesis objectives are presented separately. The conclusions from the first objective include the microstructural evaluation in two batches of steels and the summary of the prepared samples after the thermo-mechanical treatments. The results from the HP experiments are included in the second objective, whereas the results from the HMT experiments are included in the third objective.

5.2.1. Realization of the first objective

1. The microstructure of the top-layer and the mid-layer of as-received X70-1 steel appeared identical and is composed of acicular ferrite and some polygonal ferrite, quasi polygonal ferrite and bainite. The annealing, of as-received X70-1 steel, allowed in making five different grain sizes in the range of 2.5 to 12 microns for both layers, to study the effect of grain size on hydrogen diffusion and accumulation.
2. The grain size of the X70-2 steel was measured as 6.7 microns in as-received condition, and the microstructure comprises polygonal ferrite, quasi polygonal ferrite, bainite and some acicular ferrite. The cold-rolling, of as-received X70-2 steel, allowed in making five samples with different misorientation up to 2^{o}, to study the effect of misorientation on hydrogen diffusion and accumulation.

5.2.2. Realization of the second objective

The deliverables from the second objective contain the HP results from two batches of steel, and they are supported by the HMT observations from the third objective. The study with different grain sizes and misorientations used X70-1 and X70-2 steels.

5.2.2.1. Study of variable grain sizes in X70-1 steel by the HP experiment

1. The visualization of preferential diffusion through grain boundaries, triple junctions, and

cementite by immediate hydrogen discharging, after the cathodic charging in an HMT experiment, allowed in considering them as reversible trapping sites. Therefore, the decreased number of the reversible triple junction and grain boundary traps for larger grains increased the hydrogen mobility. It further increased the permeability with an increase in grain size, for the tested grains, in both layers of the steel.

2. The slightly higher permeability, higher effective diffusion coefficient, and lower apparent solubility of the mid-layer than top-layer, in the second polarization, for most of the tested range of grain size should be related to a bit larger grains in the mid-layer.
3. The effective diffusion coefficient increased and the apparent solubility decreased with an increase in grain size, for the tested grains, in both layers of the steel. It was related to the increased hydrogen mobility by the decrease of the triple junction and grain boundary traps in larger grains.
4. The initial decrease and subsequent increase in the effective diffusion coefficient for the first polarization in the mid-layer was due to the inclusion traps in the mid-layer. The initial increase and subsequent decrease in the apparent solubility of hydrogen for the first polarization in the mid-layer was also associated with inclusion traps.
5. The lower hydrogen permeability, lower apparent solubility and higher effective diffusion coefficient of the second polarization, in the tested grain sizes, was due to the saturation of irreversible traps after the first polarization.
6. The density of total, reversible, and irreversible trapping sites decreased with an increase in the grain size, for the tested grains, in top-layer. However, the density of reversible trapping sites of the mid-layer decreased for the same conditions. The irreversible and total trapping sites of the mid-layer shows an initial growth and subsequent decay due to the presence of inclusion traps in the mid-layer.

5.2.2.2. Study of different density of dislocations in X70-2 steel by the HP experiment

1. The visualization of preferential diffusion through deformed grains by immediate hydrogen discharging, after the cathodic charging in an HMT experiment, allowed in considering them as reversible trapping sites. The hydrogen permeability and effective diffusion coefficient decreased with an increase in mean kernel average misorientation up to 2º for the cold-rolled steel due to the formation of additional trapping sites. However, the permeability was higher in the as-received steel than the cold-rolled steel.
2. The second polarization had a lower permeability, lower apparent solubility, and a higher effective diffusion coefficient than the first polarization. This observation was related to

the saturation of irreversible traps after the first polarization.

3. The apparent solubility of the cold-rolled steel shows an initial growth and subsequent decay in the first and second polarizations. This observation can be explained by the shift of traps from reversible to irreversible for a mean kernel average misorientation between 1.7º and 1.9º.
4. The density of the total and irreversible trapping sites increased with the increase in mean kernel average misorientation. However, the dominant increase in those trapping sites was observed for a mean kernel average misorientation between 1.7º and 1.9º.

5.2.3. Realization of the third objective

1. The mid-layer of as-received and the top-layer of the annealed steel shows partial diffusion of hydrogen through one region of the sample and complete diffusion through another region in the same HMT experiment. It allowed in comparing the preferential hydrogen diffusion through different microstructural features from the same images.
2. The mid-layer of as-received X70-1 steel contains single inclusion and double inclusion of spherical morphology formed from a combination of titanium, aluminum, manganese, copper, and sulfur. The inclusions measured 1.5 to 3.5 microns, and the HMT experiment shows a preferential hydrogen diffusion around an inclusion by the visualized circular pattern of white silver particles of 4 to 16 microns in diameter. The circular pattern was related to the diffusion of stored hydrogen in the reversible traps that act as a localized source of hydrogen after electrochemical charging.
3. The top-layer of as-received X70-2 steel contains an irregular inclusion formed as a combination of titanium and aluminum. The inclusion measured 2.5 to 3.5 microns, and the absence of preferential hydrogen diffusion as a circular pattern around the irreversible inclusion allowed in considering it as an irreversible trap. However, there was a preferential hydrogen diffusion through the inclusion interfaces and matrix-inclusion interfaces as indicated by the overlaid white silver particles.
4. The presence and absence of a circular pattern of superimposed white metallic silver particles around inclusion or precipitate by immediate and complete hydrogen discharging in the HMT experiment is a method to distinguish the type of hydrogen traps. The reversible inclusion or precipitate shows a circular pattern around them, and irreversible hydrogen traps do not have any encircled pattern.
5. The HMT experiments allowed in concluding that the preferential hydrogen diffusion increased in the order of non-deformed grains, grain boundaries, inclusion interfaces, triple

junctions, cementites and matrix-inclusion interfaces with the matrix-inclusion interfaces being the most significant path. However, the comparison between the cementites and matrix-inclusion interfaces lacked convincing observations in the same images. Hence, they were compared between different images.

5.3. Recommendations for future work

This research was used to understand the effect of grain size and misorientation on hydrogen diffusion and accumulation in X70 pipeline steels. However, this research also allows in identifying several potential areas for future research. Also, there were several opportunities for improvement in the experimental setup.

5.3.1. Recognized potential areas for future research

1. The hydrogen diffusion parameters and visualization path for different crystallographic textures need to be explored by the HP and HMT experiments.
2. The preferential hydrogen diffusion with different grain orientations and grain boundary character distribution needs to be investigated by the HMT experiment.
3. The hydrogen diffusion parameters for the grain sizes outside the investigated range need to be evaluated by the HP experiment.
4. The hydrogen diffusion preferences for different microstructural phases need to be visualized by the HMT experiment.
5. The HMT lacks ISO standards like HP, and hence, there exists an opportunity for the improvement of the HMT methodology to obtain results with good quality.

5.3.2. Suggested improvements for experimental setup

The electrochemical experiments were highly sensitive and hard to replicate. Hence, there should be continuous efforts to minimize inaccuracies. The HP test setup, within the research group, was modified for this research work. The HMT experiment uses part of the HP test setup with modifications. The opportunities for modification in future experiments were listed.

5.3.2.1. Changes for charging cell glass beaker

The supplied cathodic current was altered by the hydrogen bubble at the charging cell. The changes in the charging current affect the rate of hydrogen production. The entire hydrogen did not diffuse through the sample, and several hydrogen atoms combine to form hydrogen molecules. The hydrogen molecules merge to create a hydrogen bubble, and it escapes through

the top surface of the electrolyte. Figure 3.9 from chapter three shows the growth and collapse of the hydrogen bubble. The extended flange of the glass beaker allows the formation of the hydrogen bubble. The bubble grows to overcome the restrictions from the extended flange before the free escape. The formation and collapse of the bubble take 3 to 5 minutes in different experiments. The supplied cathodic current decreases by 0.5 to 0.75 milliamperes with bubble resistance and recovers after the bubble collapse. The minimum flange length and maximum draft angle allow the immediate free escape of hydrogen molecules.

5.3.2.2. Replace the power source with a potentiostat

The DC power source did not have a feedback system to keep up with the changes in the electrochemical cell to provide a constant current supply of 5 mA. Hence, the user had to manually control the power supply knob to keep the same current irrespective of the fluctuations in the electrochemical cell. The manual adjustment causes inaccuracies to the supplied current. Therefore, it is recommended to substitute the power source with a potentiostat that had an inbuilt feedback system. Potentiostat, in general, supplies a much cleaner signal than a power source. Also, none of the hardware can give a zero amplitude and zero frequency DC signal. The low noise and ripple of the potentiostat compared to the power supply indicates that potentiostat was providing a cleaner DC signal. Hence, when the instrument detects ripple, the potentiostat corrects the ripple very quickly than a capable power supply. Also, the potentiostats have better accuracy and resolution than any power sources. Therefore, it is vital to use a potentiostat instead of a DC power source, when the requirement is small current.

REFERENCES

[1] British Columbians for prosperity, "Letter of Comment Submission to the Joint Review Panel of the National Energy Board regarding the proposed Trans Mountain Pipeline Expansion Project," British Columbians for Prosperity, Vancouver, 2015.

[2] Natural Resources Canada, "Frequently Asked Questions (FAQs) Concerning Federally-Regulated Petroleum Pipelines in Canad," [Online]. Available: https://www.nrcan.gc.ca/energy/energy-sources-distribution/pipelines/frequently-asked-questions-faqs-concerning-federally-regulated-petroleum-pipelines-canada/5893. [Accessed 12 June 2019].

[3] T. Nace, L. Plante and J. Browning, "Global Energy Monitor," April 2019. [Online]. Available: https://globalenergymonitor.org/pipeline-bubble/. [Accessed 15 June 2019].

[4] Canadas Oil and Natural Gas Producers, "Canadian Association of Petroleum Producers," February 2018. [Online]. Available: https://www.capp.ca/publications-and-statistics/publications/315421. [Accessed 15 June 2019].

[5] TC Energy, "Oil and Liquids Operations," [Online]. Available: https://www.tcenergy.com/operations/oil-and-liquids/. [Accessed 12 June 2019].

[6] Canadian Energy Pipeline Association, "Pipeline Industry Performance Report," Canadian Energy Pipeline Association, Calagary, 2015.

[7] National Energy Board, Canada, "Stress Corrosion Cracking on Canadian Oil and Gas Pipelines," National Energy Board, Canada, Calgary, 1996.

[8] National Energy Board, Canada, "A comparitive analysis of pipeline safety performance," National Energy Board, Canada, Calgary, 2004.

[9] P. Hopkins, "Learning from pipeline failures," WTIA/APIA welded pipe symposium, Perth, 2008.

[10] Canadian Energy Pipeline Association, "Performance Data," Canadian Energy Pipeline Association, Calgary, 2017.

[11] American Petroleum Institute - Association of Oil Pipelines, "Annual Liquids Report," API-AOPL , Washington, 2019.

[12] C. Duret-Thual, "The effect of H2S on the corrosion of steels," in *Understanding Biocorrosion*, Cambridge, Woodhead Publishing, 2014, pp. 385-407.

[13] J.-Y. Lee and S. Lee, "Hydrogen trapping phenomena in metals with B.C.C. and F.C.C. crystals structures by the desorption thermal analysis technique," *Surface and Coatings Technology,* vol. 28, pp. 301-314, 1986.

[14] G. Pressouyre and I. Bernstein, "A quantitative analysis of hydrogen trapping," *Metallurgical and Materials Transactions: A,* vol. 9, no. 11, pp. 1571-1580, 1978.

[15] E. Villalba and A. Atrens, "SCC of commercial steels exposed to high hydrogen fugacity," *Engineering Failure Analysis,* vol. 15, pp. 617-641, 2008.

[16] Office of Energy Efficiency and Renewable Energy, "Hydrogen Pipelines," [Online]. Available: https://www.energy.gov/eere/fuelcells/hydrogen-pipelines. [Accessed 25 June 2019].

[17] Canadas Oil and Natural Gas Producers, "Canadian Association of Petroleum Producers," March 2019. [Online]. Available: https://www.capp.ca/publications-and-statistics/publications/333595. [Accessed 12 June 2019].

[18] International Energy Agency, "World Energy Outlook," 2018. [Online]. Available: https://www.iea.org/weo2018/fuels/. [Accessed 13 June 2019].

[19] Canadas Oil and Natural Gas Producers, "Canadian Association of Petroleum Producers," April 2018. [Online]. Available: https://www.capp.ca/publications-and-statistics/publications/317291. [Accessed 15 June 2019].

[20] International Energy Agency, "World Energy Outlook," 2018. [Online]. Available: https://www.iea.org/weo/. [Accessed 15 June 2019].

[21] International Energy Agency, "World Energy Outlook," International Energy Agency, Paris, 2018.

[22] Institute for Energy Economics and Financial Analysis, "Fact Sheet: IEA's "Sustainable Development scenario best reflects our global energy future," IEEFA, Ohio, 2018.

[23] BP plc, "BP Statistical Review of world energy," BP plc, London, 2019.

[24] K. Petak, J. Manik and A. Griffith, "North America Midstream Infrastructure through 2035," ICF, Virgina, 2018.

[25] S. Hall, "19 - Metallurgy," in *Branan's Rules of Thumb for Chemical Engineers*, Oxford, Butterworth-Heinemann, 2012, pp. 305-320.

[26] B. N. Popov, J.-W. Lee and M. B. Djukic, "Chapter 7 - Hydrogen Permeation and Hydrogen-Induced Cracking," in *Handbook of Environmental Degradation of*

Materials, Norwich, William Andrew Publishing, 2018, pp. 133-162.

[27] J. Kittel, V. Smanio, M. Fregonese, L. Garnier and X. Lefebvre, "Hydrogen induced cracking (HIC) testing of low alloy steel in sour environment:Impact of time of exposure on the extent of damage," *Corrosion Science*, vol. 52, pp. 1386-1392, 2010.

[28] A. El-Sherik, Trends in Oil and Gas Corrosion Research and Technologies, Cambridge: Woodhead Publishing, 2017.

[29] H. Duo, Z. Dezhi, S. Taihe, Z. Zhi and D. Wenliang, "The effects of sulfide stress cracking on the mechanical properties and intergranular cracking of P110 casing steel in sour environments," *Petroleum Science*, vol. 10, no. 3, pp. 385-394, 2013.

[30] X.-B. Shi, W. Yan, W. Wang, L.-Y. Zhao, Y.-Y. Shan and K. Yang, "HIC and SSC Behavior of High-Strength Pipeline Steels," *Acta Metallurgica Sinica*, vol. 28, no. 7, pp. 799-808, 2015.

[31] Y. Sun, Q. Wang, S. Gu, Z. He, Q. Wang and F. Zhang, "Sulfide Stress Cracking Behavior of a Martensitic Steel Controlled by Tempering Temperature," *Materials*, vol. 11, no. 3, p. 412, 2018.

[32] W. K. Kim, K. Y. Kim, T. W. Yun and B. Y. Yang, "The Effect Of Metallurgical Factors On SSC Of High Strength Pipeline Steel," in *NACE International Corrosion 2008*, Louisiana, 2008.

[33] I. Chattoraj, "The effect of hydrogen induced cracking on the integrity of steel components," *Sadhana*, vol. 20, no. 1, pp. 199-211, 1995.

[34] D. R. H. Jones, Failure Analysis Case Studies II, Bergama: Pergamon, 2001.

[35] K. O. Findley, M. K. O'Brien and H. Nako, "Critical Assessment 17 Mechanisms of hydrogen induced cracking in pipeline steels," *Materials Science and Technology*, vol. 31, no. 14, pp. 1673-1680, 2015.

[36] H. Cialone and J. Holbrook, Hydrogen Embrittlement: Prevention and control, vol. 146, Philadelphia: ASTM, 1988, pp. 213-225.

[37] A. Bueno, E. Moreira and J. Gomes, "Evaluation of stress corrosion cracking and hydrogen embrittlement in an API grade steel," *Engineering Failure Analysis*, vol. 36, pp. 423-431, 2014.

[38] J. Capelle, J. Gilgert, I. Dmytrakh and G. Pluvinage, "Sensitivity of pipelines with steel API X52 to hydrogen embrittlement," *International Journal of Hydrogen Energy*, vol.

33, no. 24, pp. 7630-7641, 2008.

[39] A. B. Forero, J. A. C. Ponciano and I. S. Bott, "Susceptibility of pipeline girth welds to hydrogen embrittlement and sulfide stress cracking," *Materials and Corrosion*, vol. 65, no. 5, pp. 531-541, 2014.

[40] B. Allison Araújo, G. Dias Travassos, A. Almeida, E. O. Vilar, J. Carrasco and C. De Araújo, "Experimental characterization of hydrogen embrittlement in API 5L X60 and API 5L X80 steels," *Key Engineering Materials*, vol. 478, pp. 34-39, 2011.

[41] M. Soudani, M. H. Meliani, K. El-Miloudi, Z. Azari, A. Sorour, N. Merah and G. Pluvinage, "Reduction of hydrogen embrittlement of API 5l X65 steel pipe using a green inhibitor," *International Journal of Hydrogen Energy*, vol. 43, no. 24, pp. 11150-11159, 2018.

[42] U. B. Baek, H. M. Lee, S. W. Baek and S. H. Nahm, "Hydrogen Embrittlement for X-70 Pipeline Steel in High Pressure Hydrogen Gas," in *Pressure Vessels and Piping Conference*, Massachusetts, 2015.

[43] Z. Hafsi, M. Mishra and S. Elaoud, "Hydrogen embrittlement of steel pipelines during transients," *Procedia Structural Integrity*, vol. 13, pp. 210-217, 2018.

[44] L. Zhang, H. Shen, Y. Xing, W. Cao, Y. Fang and M. Lu, "Investigation of Hydrogen Embrittlement of High Strength Pipeline Steels under Cathodic Protection," in *NACE International.*, Louisiana, 2017.

[45] M. Cabrini, E. Sinigaglia, C. Spinelli, M. Tarenzi, C. Testa and F. M. Bolzoni, "Hydrogen Embrittlement Evaluation of Micro Alloyed Steels by Means of J-Integral Curve," *Materials*, vol. 12, no. 11, 2019.

[46] F. Huang, J. Liu, Z. Deng, J. Cheng, Z. Lu and X. Li, "Effect of microstructure and inclusions on hydrogen induced cracking susceptibility and hydrogen trapping efficiency of X120 pipeline steel," *Materials Science and Engineering: A*, vol. 527, no. 26, pp. 6997-7001, 2010.

[47] A. P. Institute, "Specification for Line Pipe," API, Washington, 2013.

[48] M. Mohtadi-Bonab, J. Szpunar and S.S. Razavi-Tousi, "A comparative study of hydrogen induced cracking behavior in API 5L X60 and X70 pipeline steels," *Engineering Failure Analysis*, vol. 33, pp. 163-175, 2013.

[49] Y. Fang, M. Lu, Y. Xing, H. Shen and L. Zhang, "Investigation of Hydrogen

Embrittlement of High Strength Pipeline Steels under Typical Service Environment," in *Advances in Structural Engineering and Mechanics*, Seoul, 2017.

[50] G. T. Park, S. U. Koh and H. G. Jung, "Effect of microstructure on the hydrogen trapping efficiency and hydrogen induced cracking of linepipe steel," *Corrosion Science* , vol. 50, no. 7, pp. 1865-1871, 2008.

[51] M. D. Danford, "Hydrogen Trapping and the Interaction of Hydrogen with Metals," in *NASA Technical paper 2744*, Alabama, 1987.

[52] G. Pressouyre, "A classification of hydrogen traps in steel," *Metallurgical Transactions A,* vol. 10, pp. 1571-1573, 1979.

[53] J. Hirth and D. G.J., " On the rate of equilibration of diffusional traps in solids," *Acta Materialia,* vol. 30, pp. 2061-2064, 1982.

[54] G. Pressouyre and I. Bernstein, "An Example of the Effect of Hydrogen Trapping on Hydrogen Embrittlement," *Metallurgical Transactions A,* vol. 12A, pp. 835-844, 1981.

[55] H. M. Ha, J.-H. Ai and J. R. Scully, "Effects of Prior cold Work on Hydrogen Trapping and Diffusion in API X-70 Line Pipe Steel during electrochemical charging," *Corrosion,* vol. 70, no. 2, pp. 166-184, 2014.

[56] M. A. Mohtadi-Bonab, M. Eskandari and J. A. Szpunar, "Texture, local misorientation, grain boundary and recrystallization fraction in pipeline steels related to hydrogen induced cracking," *Materials Science and Engineering: A,* vol. 620, pp. 97-106, 2015.

[57] V. P. Ramunni, T. D. P. Coelho and P. E. V. d. Miranda, "Interaction of hydrogen with the microstructure of low-carbon steel," *Materials Science and Engineering: A,* Vols. 435-436, pp. 504-514, 2006.

[58] E. V. d. Eeckhout, A. Laureys, Y. V. Ingelgem and K. Verbeken, "Hydrogen permeation through deformed and heat-treated Armco pure iron," *Material Science and Technology*, vol. 33, no. 13, pp. 1515-1523, 2017.

[59] A. H. Krom and A. Bakker, "Hydrogen Trapping Models in Steel," *Metallurgical and Materials Transactions B,* vol. 31, no. 6, pp. 1475-1482, 2000.

[60] D. Li, R. P. Gangloff and J. R. Scully, "Hydrogen trap states in ultrahigh-strength AERMET 100 steel," *Metallurgical and Materials Transactions A,* vol. 35, no. 3, pp. 849-864, 2004.

[61] M. Ichimura, Y. Sasajima and M. Imabayashi, "Grain boundary effect on diffusion of

hydrogen in pure aluminium," *Materials Transactions,* vol. 32, no. 12, pp. 1109-1114, 1991.

[62] N. Yazdipour, A. Haq, K. Muzaka and E. Pereloma, "2D modelling of the effect of grain size on hydrogen diffusion in X70 steel," *Computational Materials Science,* vol. 56, pp. 49-57, 2012.

[63] W. Luu and J. Wu, "Effects of sulfide inclusion on hydrogen transport in steels," *Materials Letters,* vol. 24, no. 1-3, pp. 175-179, 1995.

[64] K. Takasawa, Y. Wada, R. Ishigaki and R. Kayano, "Effects of Grain Size on Hydrogen Environment Embrittlement of High Strength Low Alloy Steel in 45 MPa Gaseous Hydrogen," *Materials Transactions,* vol. 151, no. 2, pp. 347-353, 2010.

[65] N. Zan, H. Ding, X. Guo, Z. Tang and W. Bleck, "Effects of grain size on hydrogen embrittlement in a Fe-22Mn-0.6G TWIP steel," *International Journal of Hydrogen Energy* , vol. 40, no. 33, pp. 10687-10696 , 2015.

[66] M. Masoumi, L. P. Santos, I. N. Bastos, S. S. Tavares, M. J. d. Silva and H. F. d. Abreu, "Texture and grain boundary study in high strength Fe-18Ni-Co steel related to hydrogen embrittlement," *Materials and Design,* vol. 91, pp. 90-97, 2016.

[67] M. Mohtadi-Bonab, J. Szpunar and S. Razavi-Tousi, "Hydrogen induced cracking susceptibility in different layers of a hot rolled X70 pipeline steel," *International Journal of Hydrogen Energy,* vol. 38, no. 31, pp. 13831-13841, 2013.

[68] R. B. Calhoun and D. C. Dunand, "Metal matrix composites," in *Comprehensive Composite Materials,* Oxford, Pergamon, 2000, pp. 27-59.

[69] A. H. Seikh, M. S. Soliman, A. AlMajid, K. Alhajeri and W. Alshalfan, "Austenite Grain Growth Kinetics in API X65 and X70 Line-Pipe," *Advances in Materials Science and Engineering Steels during Isothermal Heating,* pp. 1-8, 2014.

[70] R. L. Jr and R. G. Derrick, "Hydrogen transport in austenitic stainless steel," *Corrosion Science,* vol. 15, no. 6-12, pp. 565-577, 1975.

[71] T.-P. Perng and C. Altstetter, "Effects of deformation on hydrogen permeation in austenitic stainless steels," *Acta Metallurgica Sinica.,* vol. 34, no. 9, pp. 1771-1781, 1986.

[72] S. S. Chen, T. I. Wu and J. Wu, "Effects of deformation on hydrogen degradation in a duplex stainless steel," *Journal of Material Science,* vol. 39, pp. 67-71, 2004.

[73] M. Gerlanda, P. Lefranca, V. Doquet and C. Sarrazin-Baudouxa, *Materials Science and Engineering A,* vol. 507, pp. 132-143, 2009.

[74] K. Horikawa and K. Yoshida, "Visualization of Hydrogen Distribution in Tensile-Deformed Al-5%Mg Alloy Investigated by means of Hydrogen Microprint Technique with EBSP Analysis," *Materials Transactions,* vol. 45, no. 2, pp. 315-318, 2004.

[75] K. Horikawa, K. Tanigaki and H. Kobayashi, "Hydrogen Visualization in the deformed microstructure of Al-Zn-Mg base alloys," *TMS (The Minerals, Metals S Materials Society),* pp. 341-345, 2015.

[76] T. Pérez and J. Ovejero García, "Direct observation of hydrogen evolution in the electron microscope scale," *Scripta Metallurgica,* vol. 16, no. 2, pp. 161-164, 1982.

[77] A. Turnbull, "Factors affecting the reliability of hydrogen permeation measurement," *Material Science Forum,* Vols. 192-194, pp. 63-78, 1995.

[78] Y. Li, L. Cai, G. Liu and L. Ma, "Effect of cold-rolled thickness reduction degree on characteristics of hydrogen diffusion in silicon steel," *International Journal of Corrosion,* vol. 2014, p. 5 pages, 2014.

[79] D. S. d. Santos, S. Miraglia and D. Fruchart, "Effects of cathodic charging on hydrogen permeation in a Pd80Rh20 alloy," *Journal of Alloys and Compounds,* vol. 383, no. 1-2, pp. 213-218, 2004.

[80] O. Kazum and M. B. Kannan, "Effect of cathodic hydrogen-charging current density on the hydrogen diffusivity in nanostructured bainitic steels," *Materials Science and Technology,* vol. 33, no. 13, pp. 1548-1522, 2017.

[81] ISO 17081 - Method of measurement of hydrogen permeation and determination of hydrogen uptake and transport in metals by an electrochemical technique, Switzerland: International Standards Organization, 2014.

[82] P. Manolatos, M. Jerome and J. Galland, "Necessity of a palladium coating to ensure hydrogen oxidation during electrochemical permeation measurements on iron," *Electrochimica Acta,* vol. 40, no. 7, pp. 867-874, 1995.

[83] G. Zhang, S. Dorris, U. Balachandran and M. Liu, "Effect of Pd Coating on Hydrogen Permeation of Ni-Barium Cerate Mixed Conductor," *Electrochemical and Solid-State Letters,* vol. 5, no. 3, pp. J5 -J7, 2002.

[84] W. Prochwicz, W. Macherzynski, B. Paszkiewicz and Z. M. Stepien, "Hydrogen

permeation properties of Pd-coated Pd33Ni52Si15 amorphous alloy membrane," *Materials Science-Poland,* vol. 33, no. 1, pp. 56-58, 2015.

[85] Z. Wang, M. Liu, M. Lu, L. Zhang, J. Sun, Z. Zhang and X. Tang, "The Effect of Temperature on the Hydrogen Permeation of Pipeline Steel in Wet Hydrogen Sulfide Environments," *International Journal of Electrochemical Science,* vol. 13, pp. 915-924, 2018.

[86] S. I. Jeon, E. Magnone, J. H. Park and Y. Lee, "The effect of temperature and pressure on the hydrogen permeation through Pd-coated Ti26Ni21V53 alloy membrane under different atmospheres," *Materials Letters,* vol. 65, no. 15-16, pp. 2495-2497, 2011.

[87] T. Si, Y. Liu, Q. Zhang, D. Liu and Y. Li, "Effect of Microstructure on Hydrogen Permeation in EA4T and 30CrNiMoV12 Railway Axle Steels," *Metals,* vol. 9, no. 2, pp. 1-11, 2019.

[88] ASTM E112 − 12 - Standard test methods for determining the average grain size, Washington: ASTM International, 2012.

[89] P. Manolatos and M. Jerome, "A thin palladium coating on iron for hydrogen permeation studies," *Electrochimica Acta,* vol. 41, no. 3, pp. 359-365, 1996.

[90] M. A. V. Devanathan and Z. Stachurski, "The adsorption and diffusion of electrolytic hydrogen in palladium," *Proceedings of the Royal society of London. Mathematical, physical and engineering sciences,* vol. 270, no. 1340, pp. 90 - 102, 1962.

[91] L. Cailletet and Compte Rendu, "The permeability of iron for gases at high temperature," in *Weekly Reports of the Sessions of the Academy of Sciences*, vol. 58, Paris, Academy of Sciences, 1864, p. 327.

[92] H. M. Bodenstein, "Diffusion von Kathodischem Wasserstoff durch Eisen und Platin," *Elektrochemie und angewandte physikalische Chemie banner,* vol. 28, no. 23-24, pp. 517-526, 1922.

[93] M. A. V. Devanathan and Z. Stachurski, "The Mechanism of Hydrogen Evolution on Iron in Acid Solutions by Determination of Permeation Rates," *Journal of The Electrochemical Society,* vol. 111, no. 5, pp. 619-623, 1964.

[94] M. A. V. Devanathan, Z. Stachurski and W. J. Beck, "A Technique for the Evaluation of Hydrogen Embrittlement Characteristics of Electroplating Baths," *Journal of The Electrochemical Society,* vol. 110, no. 8, pp. 886-890, 1963.

[95] K. Ichitani, S. Kuramoto and M. Kanno, "Quantitative evaluation of detection efficiency of the hydrogen microprint technique applied to steel," *Corrosion Science,* vol. 45, no. 6, pp. 1227-1241, 2003.

[96] J. O. Bockris, J. McBreena and L. Nanisb, "The Hydrogen Evolution Kinetics and Hydrogen Entry into α-Iron," *Journal of the Electrochemical Society,* vol. 112, no. 10, pp. 1025-1031, 1965.

[97] H. A. Daynes, "The process of diffusion through a rubber membrane," *Proceedings of the Royal society of London. Mathematical, physical and engineering sciences,* vol. 97, no. 685, pp. 286-307, 1920.

[98] Y. Cheng, "Analysis of electrochemical hydrogen permeation through X-65 pipeline steel and its implications on pipeline stress corrosion cracking," *International Journal of Hydrogen Energy,* vol. 32, no. 9, pp. 1269-1276, 2007.

[99] H. Xue and Y.F. Cheng, "Characterization of inclusions of X80 pipeline steel and its correlation with hydrogen-induced cracking," *Corrosion Science,* vol. 53, no. 4, pp. 1201-1208, 2011.

[100] M. Mohtadi-Bonab, J. Szpunar, L. Collins and R. Stankievech, "Evaluation of hydrogen induced cracking behavior of API X70 pipeline steel at different heat treatments," *International Journal of Hydrogen Energy,* vol. 39, no. 11, pp. 6076-6088, 2014.

[101] J. Yu, T. Zhang and J. Qian, Electrical Motor Products, Cambridge: Woodhead , 2011.

[102] A. A. Rabah, A. Fekete and S. Kabelac, "Experimental Investigation on a Rotary Regenerator Operating at Low Temperatures," *Journal of Thermal Science and Engineering Applications,* vol. 1, no. 4, pp. 1-9, 2010.

[103] J. R. Taylor, An introduction to error analysis, California: Sausalito, 1996.

[104] J. O. García, "Hydrogen microprint technique in the study of hydrogen in steels," *Journal of Materials Science,* vol. 20, no. 7, p. 2623–2629, 1985.

[105] Y. Kisaka, N. Senior and A. P. Gerlich, "A Study on Sulfide Stress Cracking Susceptibility of GMA Girth Welds in X80 Grade Pipes," *Metallurgical and Materials Transactions,* vol. 50, no. 1, pp. 249-256, 2019.

[106] G. F. V. Voort, Metallography: Principles and Practice, New York: McGraw-Hill, 1984.

[107] F. Humphreys, "Quantitative metallography by electron backscattered diffraction," *Journal of Microscopy,* vol. 195, no. 3, pp. 170-185, 2003.

[108] F. J. Humphreys, "Review Grain and subgrain characterization by electron backscatter diffraction," *Journal of Materials Science,* vol. 36, no. 16, pp. 3833-3854, 2001.

[109] R. J. F. Tavitas, R. S. Garcés and V. H. L. Cortéz, "Hybrid Laser – Arc Welding Applied in Longitudinal Joints for Hydrocarbon Conduction Pipes," in *MRS Proceedings*, 2015.

[110] H. Alipooramirabad, R. Ghomashchi, A. Paradowska and M. Reid, "Residual stress-microstructure- mechanical property interrelationships in multipass HSLA steel welds," *Journal of Materials Processing Technology,* vol. 231, pp. 456-467, 2016.

[111] S. v. Bohemen and J. Sietsma, "The kinetics of bainite and martensite formation in steels during cooling," *Materials Science and Engineering: A,* vol. 527, no. 24–25, pp. 6672-6676, 2010.

[112] J. Omale, E. Ohaeri, A. Tiamiyu, M. Eskandari, K. Mostafijur and J. Szpunar, "Microstructure, texture evolution and mechanical properties of X70 pipeline steel after different thermomechanical treatments," *Materials Science and Engineering: A,,* vol. 703, pp. 477-485, 2017.

[113] H. Tehemiro, T. Takeda, S. Matsuda, K. Yamamoto and H. Okomura, "Effect of accelerated cooling after controlled rolling on the hydrogen-induced cracking resistance of pipeline steels," *Transactions of the Iron and Steel Institute of Japan,* vol. 25, no. 9, pp. 982-988, 1985.

[114] R. Feng, S. Li, X. Zhu and Q. Ao, "Microstructural characterization and formation mechanism of abnormal segregation band of hot rolled ferrite/pearlite steel," *Journal of Alloys and Compounds,* Vols. 646,, pp. 787-793, 2015.

[115] T. H. Simm, L. Sun, D. R. Galvin, P. Hill, M. Rawson, S. Birosca, E. P. Gilbert, H. Bhadeshia and K. Perkins, "The Effect of a Two-Stage Heat-Treatment on the Microstructural and Mechanical Properties of a Maraging Steel," *Materials,* vol. 10, no. 12, p. 1346, 2017.

[116] F. Popa, I. Chicinas, D. Frunza, I. Nicodim and D. Banabic, "Influence of high deformation on the microstructure of low-carbon steel," *International Journal of Minerals Metallurgy and Materials,* vol. 21, no. 3, pp. 273-278, 2014.

[117] S. Ebnesajjad, Fluoroplastics, Norwich: William Andrew, 2015.

[118] L. Holappa and O. Wijk, "Inclusion Engineering," in *Treatise on Process Metallurgy*, Amsterdam, Elsevier, 2014, pp. 347-372.

[119] J. Guo, S.-s. Cheng, H. Guo and Y. Mei, "Determination of non-metallic inclusions in a continuous casting slab of ultra-low carbon interstitial free steel by applying of metallographic method, electrolytic method and RTO technique," Nature Research, London, 2019.

[120] Q. Sha and D. Li, "Microstructure and Properties of Low Manganese API X70 Pipeline Steel for Sour Service Application," in *Proceedings of the 8th Pacific Rim International Congress on Advanced Materials and Processing*, Cham, 2013.